Studies of Photophysical Processes of Semiconductor Nanomaterials and Molecular Fluorophores in Supramolecular Assemblies

By

KIRAN BHARADWAJ

CHEM11201604033

National Institute of Science Education and Research,

Bhubaneswar, Odisha

A thesis submitted to the

Board of Studies in Chemical Sciences

In partial fulfillment of requirements

for the Degree of

DOCTOR OF PHILOSOPHY

of

HOMI BHABHA NATIONAL INSTITUTE

November, 2020

राष्ट्रीय विज्ञान शिक्षा एवं अनुसंधान संस्थान, भुवनेश्वर
(परमाणु उर्जा विभाग, भारत सरकार का एक स्वायत्त संस्थान)
NATIONAL INSTITUTE OF SCIENCE EDUCATION AND RESEARCH, BHUBANESWAR
(An autonomous Institution under Department of Atomic Energy, Govt. of India)

CERTIFICATE BY THE GUIDE

This is to certify that **Ms. Kiran Bharadwaj** bearing HBNI Enrolment No.: **CHEM11201604033** has incorporated all the suggestions, corrections and comments received from the thesis examiners & Guide, in the final thesis. Furthermore, the suggestions, corrections and comments received from the members of the viva-voce board during the viva-voce examination held on **27.04.2021** have also been incorporated in the final Ph.D. thesis which is submitted to the Academic Office, NISER.

Dr. Subhadip Ghosh

Signature & Name of the Ph.D. Guide

Date: 27.04.2021

STATEMENT BY AUTHOR

This dissertation has been submitted in partial fulfillment of requirements for an advanced degree at Homi Bhabha National Institute (HBNI) and is deposited in the Library to be made available to borrowers under rules of the HBNI.

Brief quotations from this dissertation are allowable without special permission, provided that accurate acknowledgement of source is made. Requests for permission for extended quotation from or reproduction of this manuscript in whole or in part may be granted by the Competent Authority of HBNI when in his or her judgment the proposed use of the material is in the interests of scholarship. In all other instances, however, permission must be obtained from the author.

Kiran Bharadwaj

DECLARATION

I, hereby declare that the investigation presented in the thesis has been carried out by me. The work is original and has not been submitted earlier as a whole or in part for a degree/diploma at this or any other Institution / University.

Kiran Bharadwaj

List of Publications

[1] "Spectroscopic and Calorimetric Studies of Molecular Recognitions in a Dendrimer Surfactant Complex." S. Koley, M. R. Panda, **K. Bharadwaj,** S. Ghosh, *Langmuir*, **2018**, *34*, 817−825.

#[2] "Model-Free Estimation of Energy-Transfer Timescales in a Closely Emitting CdSe/ZnS Quantum Dot and Rhodamine 6G FRET Couple", **K. Bharadwaj**, S. Koley, S. Jana, S. Ghosh, *Chem. Asian J.*, **2018**, *13*, 3296 – 3303.

#[3] "Role of Emissive and Non-Emissive Complex Formations in Photoinduced Electron Transfer Reaction of CdTe Quantum Dots", **K. Bharadwaj**, H. Choudhary, S. Hazra, S. Ghosh, *Chem. Asian J.*, **2019**, *14*, 4207-4216.

#[4] "Study of Interfacial Charge Transfer from an Electron Rich Organic Molecule to CdTe Quantum Dot by using Stern-Volmer and Stochastic Kinetic Models", **K. Bharadwaj**, H. Choudhary, S. Hazra, S. Ghosh, *ChemPhysChem*, **2020**, *21*, 415-422.

the publications included in the present thesis

Kiran Bharadwaj

Conferences

[1] Delivered a short talk on "Model-Free Estimation of Energy Transfer Timescale in a Closely Emitting CdSe/ZnS Quantum Dot and Rhodamine 6G FRET Couple" at the National Conference on "Advances in Materials Chemistry and Applications" (**AMCA-2019**) at Utkal University. **(Short Talk)**

[2] Presented a poster titled "Model-Free Estimation of Energy Transfer Timescale in a Closely Emitting CdSe/ZnS Quantum Dot and Rhodamine 6G FRET Couple" in the international conference "Trombay Symposium on Radiation and Photochemistry (**TSRP-2020**) organized by Bhabha Atomic Research Centre (BARC), Mumbai. **(Poster Presentation)**

Kiran Bharadwaj

Dedicated to …….

My Family

ACKNOWLEDGEMENTS

I may humbly be permitted to show my appreciation to everyone who was an incredible help throughout this journey.

I would like to offer my gratitude and respect to my mentor **Dr. Subhadip Ghosh**, for his unwavering guidance, insightful suggestions, constructive criticism, and kindness. His modern thinking, scientific reasoning, and methodology have made this work conceivable and will continue encouraging me in the future. He allowed me to think freely and motivated me to solve my research problems. I feel fortunate to have worked with him.

I would like to express my sincere thanks to my Doctoral committee members, chairman **Dr. Sanjib Kar**, **Dr. Sudip Barman**, **Dr. Himansu Sekhar Biswal**, **Prof. Tapobrata Som** for their support and recommendations throughout my Ph.D. I would also like to extend my thanks to all the teachers who taught me during course-works. I am grateful to NISER, D.A.E., and HBNI for providing me with financial support, the best research facilities, and infrastructure.

I would also like to recognize the invaluable assistance provided by my senior, **Dr. Somnath Koley** during the learning of new instruments and methods. I also appreciate the constant support and co-operation of my fellow lab members, **Ms. Krishna Mishra** and **Ms. Ayendrila Das**.

Also, I am deeply indebted to my parents (**Mrs. Anita Sharma** and **Mr. Harish Kumar Sharma**) and my beloved sister, **Ms. Deepti Bhardwaj** for their unconditional love, support, and blessings. The successful completion of my dissertation would not have been possible without the love and nurturing of my family. I am also extremely grateful to my friends, **Ms. Sanchita Shah**, **Mr. Siddharth Singh**, **Ms. Anjana Kamal**, and **Ms. Shalini Pandey** for their constant moral support.

CONTENTS

LIST OF SCHEMES

LIST OF FIGURES

LIST OF TABLES

CHAPTER 6

Photoinduced Electron Transfer: Collisions or Complexation?A Limiting Case Study

6.1 Introduction

As discussed in the previous chapter, cadmium telluride (CdTe) and its alloys are in limelight for their extensive use in photovoltaics (PVs) and photo-detectors in the last few decades.[183,186–194,221–244] In the previous as well as present chapter, we studied bimolecular PET reactions in toluene for the simple nature of the kinetics especially when studied in the solution phase. In the solution phase, PET generally takes place following one-to-one collisions between donor and acceptor molecule, which is much easy to interpret without having knowledge of multi-particle interactions, sample morphology, and sample heterogeneity. In solid-state study, one must have this knowledge.[199–204] Besides, in the solution phase study a direct contact of fluorescent molecules with air oxygen is unlikely. Oxygen quenches the emission of fluorescent molecules which causes the solid-state PET study more complicated.[21] Bimolecular PET study in solution is widespread for organic dye molecules but remained relatively less explored for QDs. Although the latter has more applications in PVs and light-emitting devices.[78,132,182] In the previous chapter we had explored the complexation between CdTe QD and the quencher molecules and emissive as well as nonemissive complexation between the two. The Tachiya model was implemented which beautifully explained the entire quenching process. This chapter is an extension of previous chapter where we have explored the applicability of the same Tachiya model for different QD and quencher combinations. Unlike in the previous chapter where complexation was predominant, here in the present chapter, we have observed that at low to moderate quencher concentrations

interaction of NMA with QD is predominantly collisional with some contribution from QD-NMA complex formation.[245] However, high quencher concentration leads to more number of QD-NMA complex formations, causing a sudden upward curvature in steady-state SV plots. In all the cases a ground state complex formation is detected through ITC studies. Our mechanistic analysis provides an in-depth understanding of a bimolecular PET process where QD acts as an electron acceptor. The outcome of our study will help researchers in the rational design of next-generation devices.

6.2 Synthesis, Purification, TEM Measurements, and Spectral Properties

Three different batches of dodecylamine (DDA) capped CdTe QD particles were synthesized and purified following the same procedure described in Chapter 5.

TEM images for this batch (different batch than the batch in the previous chapter) revealed a high monodispersity of the samples with sizes ~3.2 nm (QD1), ~4.2 nm (QD2), and ~5.2 nm (QD3). QD particle size increases gradually as we move from QD1 to QD3 (Figure 6.1A-B). The absorption and emission spectra of CdTe QD are shifted to the red side by increasing the particle size due to a quantum confinement effect (Figure 6.1C).

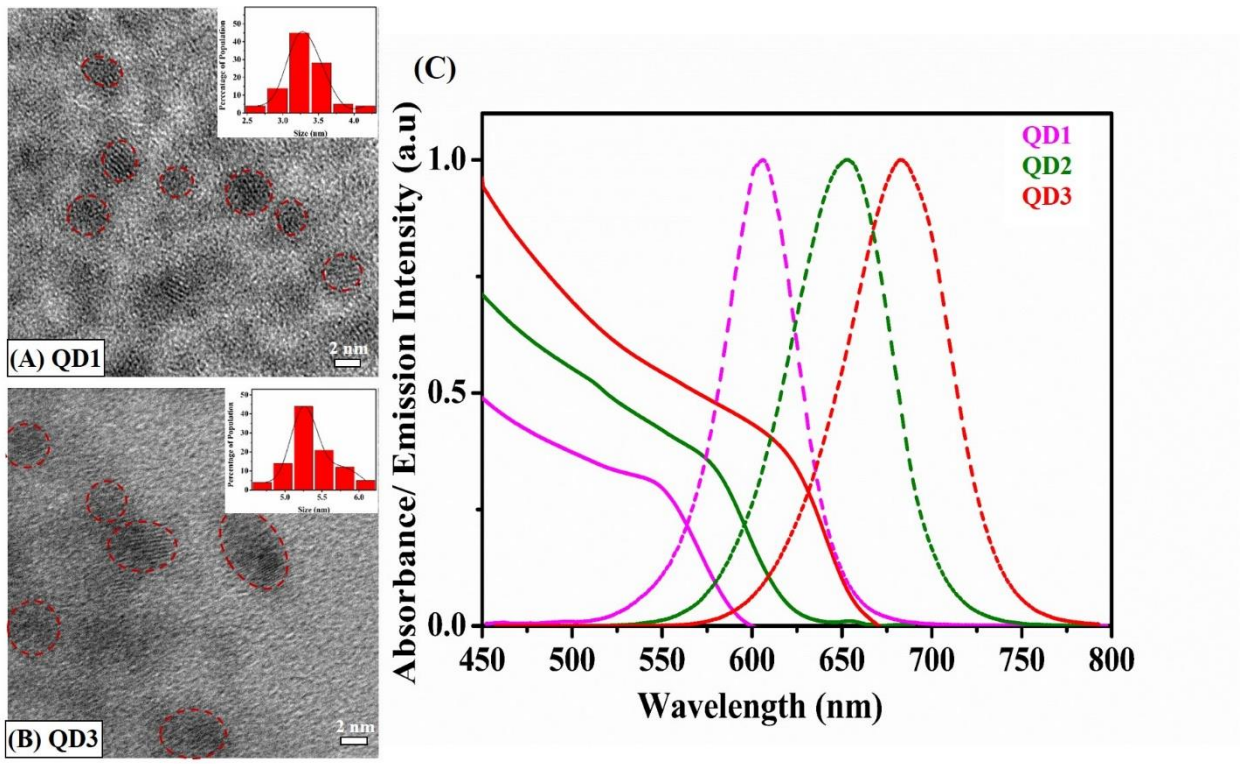

Figure 6.1. (A-B) High-Resolution TEM images along with the particle size distributions (inset) of QD1 and QD3. The average particle sizes for QD1 and QD3 were ~3.2 nm and ~5.2 nm (C) Spectral signatures of QD1 (Magenta), QD2 (Green), and QD3 (Red). Solid curves represent the absorption spectra while the dashed curves represent the emission spectra.[245]

6.3 Fluorescence Quenching: Steady-State and Time-Resolved

Emission intensity and the excited state lifetime of all three QDs (QD1, QD2, and QD3) notably quenched in the presence of NMA (Figure 6.2, Table 6.1).

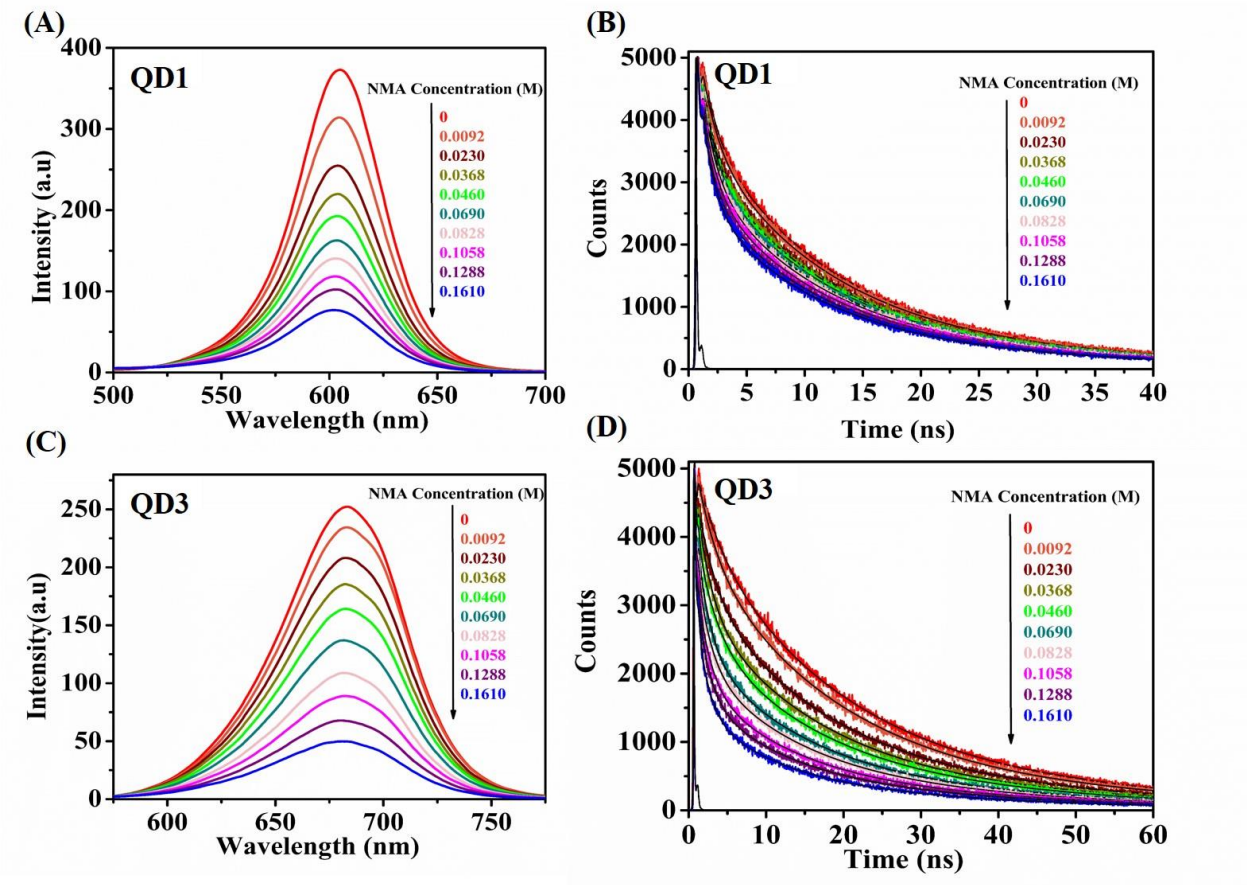

Figure 6.2. Steady-state fluorescence quenching (A and C) and lifetime quenching (B and D) of QD1 (A and B) and QD3 (C and D) upon addition of NMA. The excitation wavelength was kept to be λ_{ex}~405 nm for all the measurements while the lifetimes were recorded at the corresponding emission maxima. [245]

Table 6.1. Average lifetimes of quantum dots at different quencher concentrations. [245]

CdTe Quantum Dot	Quencher (NMA) Concentration (M)	τ_{avg} (ns)
	0	7.57
	0.0092	6.74
	0.023	6.69
QD1	0.0368	6.18
	0.046	6.05
	0.069	5.62
	0.0828	5.97
	0.1058	4.82
	0.1288	4.22
	0.161	4.08
	0	9.37
	0.0092	8.94
	0.023	8.58

QD2	0.0368	8.12
	0.046	7.78
	0.069	7.42
	0.0828	6.97
	0.1058	6.45
	0.1288	6.22
	0.161	5.94
	0	19.04
	0.0092	17.12
	0.023	15.43
QD3	0.0368	13.52
	0.046	12.58
	0.069	11.64
	0.0828	11.34
	0.1058	10.40
	0.1288	9.39
	0.161	8.51

6.4 Photoinduced Electron Transfer: Redox Profiles

The quenching is due to a hole transfer from the valance band (VB) of QD* to the HOMO of the NMA molecule. Energy levels of the donor obtained from Brus's approximations show a nice matching with the acceptor's energy level (SCHEME 6.1). Similar quenching phenomena are reported in the literature but most of them studied hole or electron transfer from QD* to π-conjugated polymers.[170,197–200] For instance, Ghosh and colleagues studied the hole transfer in the CdTe QD-MEHPPV hybrid system, where they observed excited-state lifetime of CdTe QD quenched significantly in the presence of MEH-PPV π-conjugated polymer nanoparticles. Quenching was asserted due to a hole transfer from CdTe QD* to MEH-PPV.

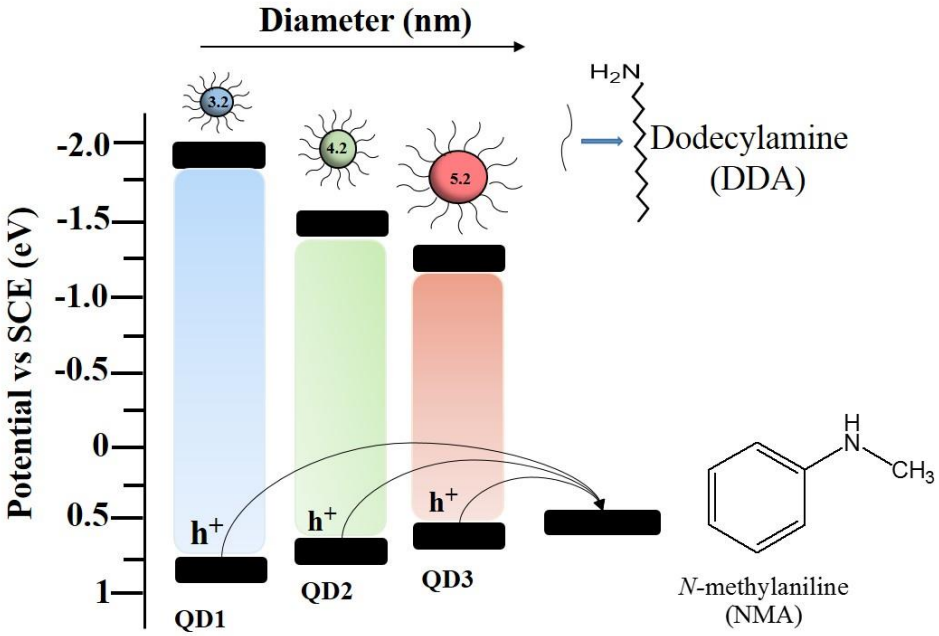

SCHEME 6.1. Energy levels of CdTe QDs and an NMA molecule. Arrows show the hole transfers from QDs* to NMA. The calculation of energy levels is provided in Chapter 2.[245]

6.5 Isothermal Titration Calorimetry Study

The CdTe QDs used in our study are dodecylamine (DDA) capped. The DDA capping layer can easily trap the quencher molecules at a high quencher concentration. In such a case no collision is required for PET reaction and solvent diffusion will have a little role on overall PET kinetics [128,132,182,218–220] In our study formation of QD-NMA static complex was confirmed by isothermal calorimetry (ITC) study (Figure 6.3), which showed a moderate interaction (K~150 M^{-1}) between QD and NMA, nicely correlated with steady-state SV curves.[246] In the ITC study, QD3 (in toluene) in the cell was titrated by a ~10 times higher concentration titrant NMA (in toluene). We used a high concentration of NMA since complex formation is more feasible at high quencher concentrations. A total of 38 μl of high concentration NMA solution was injected into the cell (containing QD solution) using 38 successive injections (i.e., 1 μl per injection). Heat absorbed/evolved was recorded against each injection. The heat of dilutions of QD3 and NMA was determined in two separate experiments where QD3 and NMA were injected in toluene. Heats of dilutions were subtracted from the total heat change that gave us the heat change due to the complex formation. Heat change due to complex formation was plotted against the NMA-to-QD mole ratio, which was fitted using a single-site binding model to obtain the value of equilibrium binding constant (K~150 M^{-1}).

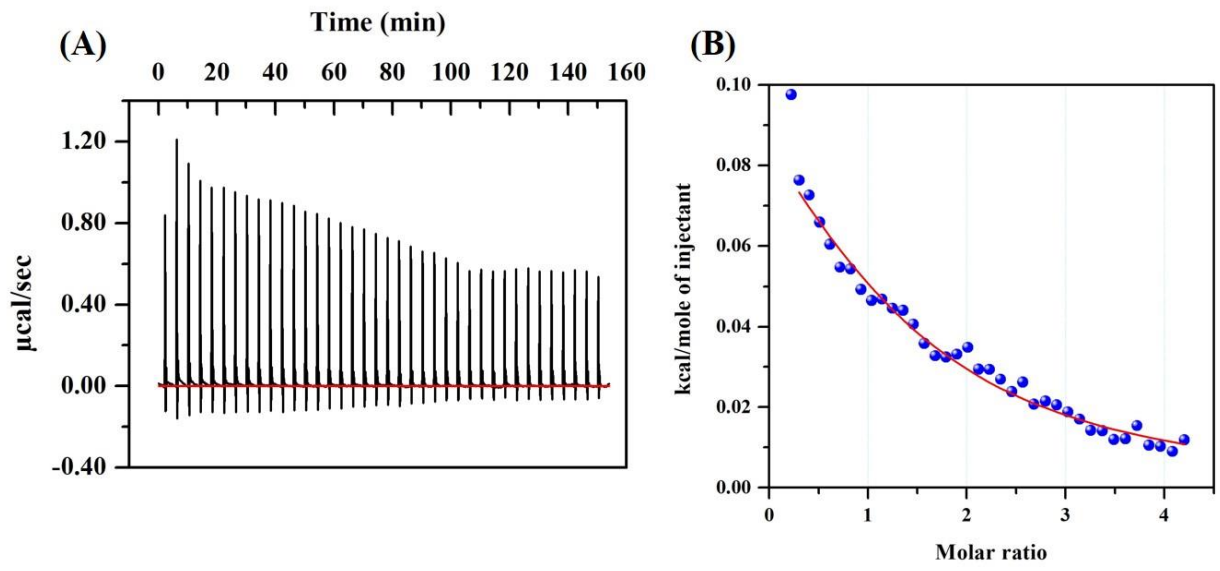

Figure 6.3. (A) Raw data of heat change due to sequential injections of NMA solution from the injector syringe to QD3 solution in the sample cell at 20 ^{0}C. (B) Integrated heat change due to the complex formation as a function of the NMA-to-QD3 molar ratio. Heat change data was fitted with a one-site binding model (red solid line) to obtain the value of the binding constant. [245]

The moderate value of the binding constant (K~150 M^{-1}) suggested that at low quencher concentration, the PET mechanism is predominantly collisional with some contribution from the complex formation. We fitted our PET data with two models: (1) Tachiya's stochastic kinetic model and (2) Stern-Volmer analysis with some modifications. Tachiya's stochastic model has been used on several occasions where QD emission is quenched by PET and FRET processes.[39,207,211–214,] By assuming the presence of trap sites at the QD surface this model has nicely explained the non-exponential nature of QD's fluorescence lifetime profile. Undoubtedly the incorporation of this assumption during PET analysis of the QD-NMA system provided us an accurate estimation of PET kinetics. However, the stochastic model was applicable only when PET kinetics was solely controlled by QD-NMA complex formation which is possible at high quencher

concentrations. Therefore the use of stochastic kinetic analysis was restricted to a high NMA concentration regime only. On the other hand, SV analysis is imperative at low to moderate or even at high quencher concentrations, especially when PET is taking place through either collisional or static or a mixture of both the processes. Our analyses using the SV model and stochastic kinetic model enabled a conclusive understanding of the PET mechanism of the QD-NMA system. In the next section of this chapter, the stochastic kinetic analysis, demonstrating the PET kinetics only at a high quencher concentration regime, followed by SV analysis at low to high quencher concentrations is provided. The PET data were fitted by two models namely: (1) Tachiya's stochastic kinetic model and (2) Stern-Volmer analysis with some modifications. Tachiya's stochastic model has been used on several occasions where QD emission is quenched by PET and FRET processes.[39,207,211–214] By assuming the presence of trap sites at the QD surface this model has nicely explained the non-exponential nature of QD's fluorescence lifetime profile.

6.6 PET Analysis at High NMA Concentration using Stochastic Kinetic Model

At high quencher concentration, QD easily finds NMA molecules in its immediate environment for complex formation. Before applying the stochastic kinetic model to our system, we took two assumptions: (1) at high quencher concentration regime PET kinetics is predominantly controlled by the complex formation, and (2) since donor-acceptor are separated by a thick DDA layer within the complex, the quenched fluorescence lifetimes of these complexes can't escape the detection by 70 ps IRF of our TCSPC setup. To calculate the mean number of bound NMA molecules per QD at high quencher concentrations (>0.10 M) and thereby PET rate coefficients, we assumed NMA molecules are attached to QD following Poisson distribution.[39,207,213,214] As discussed in the previous chapter (Chapter 5), the excited state decay of QD* in the presence of the average m

number of attached quencher molecules (and m_t number of trap sites) per QD can be expressed by equation 5.6.[39,211,213,214] In the absence of quencher, excited state population decay kinetics of QD* is not a unimolecular process, as manifested by the nonexponential nature of the excited state decay profiles (Figure 6.2 B-D). Exciton trap sites at the QD surface act as efficient quenchers that are responsible for not observing an exponential decay of the excited state QD population in the absence of NMA.[39] Equation 5.7 of the previous chapter, nicely explains the excited state decay kinetics of QD* alone by assuming average m_t trap sites per QD distributed at the surface of QD following a Poisson distribution.[39]

Similarly, a survival probability function [$S_q(t,m)$, equation 5.8] as derived in chapter 5, by normalizing equation 5.6 by equation 5.7, was used to fit our experimental I(t,m)/I(t) curves (i.e., lifetime profile of QD* quenched by NMA/unquenched lifetime profile of QD*).[132,182,212] These experimental ratio curves of lifetimes at different NMA concentrations were fitted with equation 5.8, which gave us two crucial parameters: (1) PET rate coefficient per NMA molecule (k_q) and (2) the mean number of NMA molecules attached to a QD (m) (Table 6.2). Equation 5.8 enables a satisfactory fitting only to the high quencher concentration data (>0.1 M) (Figure 6.4). This was maybe due to the reason that at high quencher concentration QD-NMA complex formation becomes more feasible. Collisional quenching leads the PET reaction at a low quencher concentration (<0.08 M), which cannot be explained by Equation 5.8. Instead, a Stern-Volmer (SV) fitting equation was employed, which is discussed in the latter part of this chapter The number of NMA molecules per QD at a high quencher concentration regime (>0.1 M) increases from ~0.33 to ~0.47 with increasing the quencher concentration from ~0.106 M to ~0.161 M for smallest sized QD (~3.2 nm; QD1). The same increases from ~0.59 to ~0.76 when QD size is increased to ~5.2 nm (QD3). The bigger QD (QD3) provides a more binding area to NMA than that in a smaller QD

(QD1), which results in a more number of NMA bound to QD3. The smallest sized QD (QD1) recorded the fastest PET rate (~0.7 ns^{-1} per NMA), while the biggest sized QD (QD3) exhibited the slowest PET rate (~0.41 ns^{-1} per NMA), as obtained from the fittings with our stochastic kinetic model (Figure 6.4, Table 6.2). In all the cases PET rates were nicely correlated by the chemical driving forces (ΔG_0) associated with the PET reactions (Table 6.2 and SCHEME 6.1).

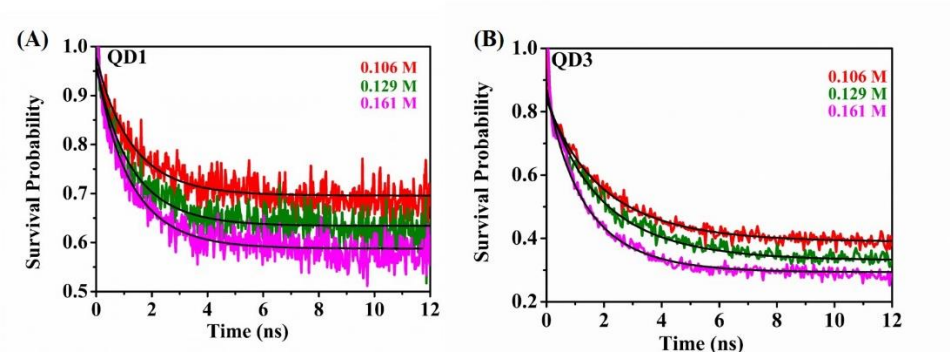

Figure 6.4. The experimental survival probability curves [I(m,t)/I(t)] with their best fits (black solid lines) using Equation 5.8 for QD1 (A) and QD3 (B) for high NMA concentrations (i.e., 0.106, 0.129 and 0.161 M). [245]

Table 6.2. Values of best-fitted parameters as obtained from the fittings of survival probability curves with equation 5.8 (stochastic kinetic model). [245]

Quantum Dot	**NMA Concentration (M)**	**The average number of quencher molecule per QD (m)**	**k_q (ns^{-1})**	**ΔG_0 (eV)**
QD1	0.1058	0.33	0.7	-3.1
	0.1288	0.4		
	0.1610	0.47		
QD2	0.1058	0.25	0.56	-2.4
	0.1288	0.29		
	0.1610	0.34		
QD3	0.1058	0.59	0.43	-2.06
	0.1288	0.74		
	0.1610	0.76		

PET rate coefficients reported in the above section were calculated through fitting to lifetime quenching data with the help of a stochastic kinetic model. We also attempted to fit steady-state

quenching data using the same set of parameters obtained from the lifetime quenching data fittings. As we know steady-state intensity is the time integral of the lifetime profile across the entire time window,[48] therefore starting from the time-resolved fitting equation (equation 5.8) one can easily derive a steady-state fitting equation as follows.[39,211,213,214]

$$\frac{I}{I_0} = e^{-m} + \frac{\left\{\sum_{n>0}^{\infty}\sum_{n'=0}^{\infty}\left(m^n e^{-m}/n!\right)\left(m_t^{n'} e^{-m_t}/n'!\right)/[1+nk_q/k_0+n'k_{qt}/k_0]\right\}}{\sum_{n'=0}^{\infty}\left(m_t^{n'} e^{-m_t}/n'!\right)/[1+n'k_{qt}/k_0]} \quad (6.1)$$

Due to the inherently complex nature of the above equation, it is not possible to fit our steady-state data with this equation without further simplification. However, equation 6.1 can be simplified when k_q/k_0 is much larger than unity [i.e., PET rate (k_q) is much higher than the natural excited state decay rate (k_0)]. Then, equation 6.1 is further reduced to a form with the right-hand side remains only "e^{-m}". One may use the "m" values at different quencher concentrations obtained from the time-resolved fittings (Figure 6.4, Table 6.2) to fit the steady-state "I/I_0 vs [NMA]" curve. Where I and I_0 are the steady-state emission intensities of QD* in the presence and absence of NMA. However, in our case, k_q/k_0 is not >>1, so a reduced form of equation 6.1 can't be used.

6.7 PET Analysis using Stern Volmer Plots across all NMA Concentration Ranges

As mentioned earlier, using the stochastic kinetic model was limited only to the high NMA concentrations, we simultaneously used Stern Volmer (SV) plots which account for collisional and static quenching across all concentration regimes (Figure 6.5).[21] For all the three QDs, steady-state SV plots (I_0/I vs [NMA]) were found to be distinctly different from their respective lifetime SV plots (τ_0/τ vs [NMA]). Steady-state SV plot (I_0/I vs [NMA]) showed a linear nature until quencher

concentration reaches ~0.08 M, which was followed by a sudden change in slope to an upward curvature at high quencher concentrations (>0.1 M). However, the lifetime SV plots (τ_0/τ vs [NMA]) were found to be linear with a lower slope compared to that in the steady-state SV curve (for all three QDs) across the entire concentration range. This is a clear indication of QD-NMA complex formation, which becomes more prominent at higher quencher concentrations (>0.1 M).

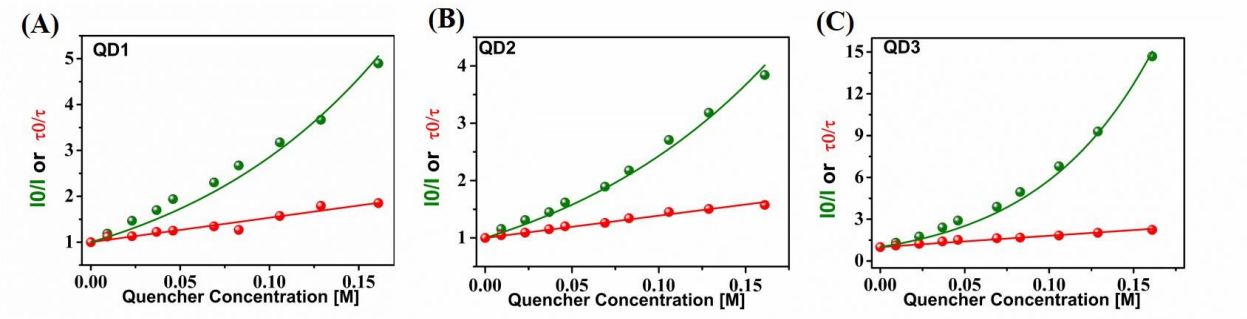

Figure 6.5. Steady-state Stern-Volmer plots (green balls) and time-resolved Stern-Volmer plots (red balls) for QD1 (A), QD2 (B), and QD3 (C). Green and red solid lines represent the fittings of the steady-state and lifetime data using Stern-Volmer fitting equations. [245]

At low quencher concentration (up to ~0.08 M) quenching mechanism was mostly controlled by bimolecular collisions; nevertheless, a small contribution from QD-NMA complex formation cannot be ruled out, since the slope of the steady-state SV plot remained higher compared to the slope of lifetime SV plot even at low quencher concentrations (Figure 6.5). We found that the SV fitting equations can conclusively fit both, time-resolved and steady-state SV plots across all the concentration regimes. At high quencher concentrations (>0.1 M) effect of QD-NMA complex formation in the quenching process became more prominent than bimolecular collisions, indicated by observing a sudden upward curvature in steady-state SV plot at high quencher concentrations

(Figure 6.5). Sudden upward curvature in the steady-state SV plot at high NMA concentrations and significant heat change in the ITC experiment indicate a strong interaction between QD and NMA molecules, leading to the complex formation (Figure 6.5 & 6.3). From lifetime SV fittings ($\tau_0/\tau=1+k\tau_0[NMA]$) we obtained PET rates [$k\sim0.7\times10^9$ $M^{-1}S^{-1}$ (QD1-NMA), $\sim0.4\times10^9$ $M^{-1}S^{-1}$ (QD2-NMA) and 0.4×10^9 $M^{-1}S^{-1}$ (QD3-NMA)] due to the collisional quenching only. The values of collisional quenching constants were fixed in the steady-state SV fitting equation [$I_0/I=(1+k\tau_0[NMA])\exp(K[NMA])$] to obtain equilibrium constants [$K\sim6.2$ M^{-1} (QD1-NMA), ~5.7 M^{-1} (QD2-NMA) and ~11.6 M^{-1} (QD3-NMA)] of QD-NMA complexes (Table 6.3). PET rates due to collisional quenching (k) were found to be always much lower than the upper limit ($k_d\sim1.2\times10^{10}$) of any bimolecular diffusion-controlled process in toluene. We chose toluene as the reaction medium for its low viscosity, which in turn provided us a much higher diffusion-controlled rate compared to the intrinsic PET rates. If the intrinsic PET rate is faster than the diffusion rate of the radium, SV fitting will report the mass transportation rate of the medium instead of the PET rate. However, in our case, the diffusion rate in toluene was much faster than the measured PET rates.

Table 6.3. Values of Stern-Volmer fitting parameters. [245]

Quantum Dots	**k_q ($M^{-1}S^{-1}$)**	**K_S(M^{-1})**
QD1	0.7×10^9	6.2
QD2	0.4×10^9	5.7
QD3	0.4×10^9	11.6

Through steady-state SV plots, one can easily identify the involvement of non-emissive complex formation in the PET process. Apart from non-emissive complexes, ultrafast PET can also cause the dark complex formation provided quenched lifetime falls shorter to the IRF of the time-resolved setup. In such a scenario, only a steady-state SV plot can detect the non-emissive/ultrafast complex formations. However, in our case chances of ultrafast complex formation were unlikely since the donor and acceptor are separated by a thick DDA layer within the complex. Dark complexes are not detected by a time-resolved setup (TCSPC), which excludes their contributions from time-resolved SV and stochastic analyses. The observed PET rate coefficients obtained using the stochastic kinetic model (at high quencher concentrations) are the intra-complex PET rate constants of the QD-NMA emissive complexes. In this work, we studied the PET kinetics due to bimolecular collisions and complex formations.

6.8 Conclusion

Besides, kinetics due to the surface trap sites of QD interfere with the precise detection of PET components, and a suitable model along with the complete Stern Volmer analysis is sometimes required for a conclusive fitting and a complete PET picture. Unlike in the previous fluorophore quencher combination (used in the previous chapter), in the present case of CdTe QD and NMA quencher, at low-to-moderate quencher concentrations (<0.08 M), collisional quenching predominantly controls the PET kinetics of the QD-NMA system. However, at high quencher concentrations (>0.1 M), QD-NMA complex formations dominate the quenching process. Two regimes (collisional and static) of the kinetics are well understood by Stern-Volmer analysis. In a separate analysis especially at high quencher concentrations, we employed a stochastic kinetic model, which enabled a conclusive fitting at a high quencher concentration regime only, where the

complex formation is prevalent. Using the stochastic kinetic model is important for the QD-NMA system since it explains the non-exponential decay behavior of the excited state population of QD. However, the stochastic model is not very efficient to explain the collisional quenching. This is in contrast to SV analysis, which nicely explains the PET kinetics across all concentration regimes, but without considering the trap sites at the QD surface. Therefore it is imperative to use both the analyses for obtaining a conclusive understanding of PET kinetics in the QD-NMA system. The outcome of our study will help researchers with the efficient use of CdTe QDs in various device applications.[148]

6.9 Conclusive Summary of Chapter 5 and 6 at a glance: A comparative study

A very quick glance at chapters 5 and 6, summarises the various aspects of PET involving a quantum dot particle and a quencher molecule. One can adopt different analysis methods and models to get a complete picture of the PET process of interest.

Here the two cases of PET involving the same QD but a different quencher molecule needed different approaches to studying the PET process. In the case of CdTe QD and 2,4-DNT, the DNT molecule acted as an acceptor of electron and showed complexation with QD even at low concentrations. On contrary, in the case of CdTe QD and NMA, the NMA molecule acted as a donor of electrons and showed complexation only at high concentrations. Both the cases needed a different approach to studying the entire PET process. The following table summarises the two cases.

Table 7. The Two Charge Transfer Processes at a Glance

	CASE I	**CASE II**
Quantum Dot	DDA capped CdTe	DDA capped CdTe
Quencher	2,4-DNT	NMA
Role of quencher	Acceptor of electron	Donor of electron
Strength of binding	Moderate	Weak
Stochastic model	Fits all the concentration range well enough	Fits only high concentration data well enough
Dominant path of quenching (Lifetime)	Complexation	Collisional
Average number of quencher molecules attached (highest concentration data)	1.73 Higest [DNT]=17mM	0.34 Highest [NMA]=161mM

SUMMARY

Excited-state processes are ubiquitous in chemistry, biology, and material sciences. In-plant biology photosynthesis, an excited state process is crucial for living organisms. Other important chemical processes including optical absorption, charge separation and recombination, energy relaxation, energy transfer, etc play important roles in various semiconductor devices including light-harvesting devices and light-emitting diodes. A large number of devices use semiconductor quantum dots, for their rich spectral properties, high charge mobility, and charge transfer properties, all these properties can be tuned by changing the particle sizes.

In this thesis, time-resolved area normalized spectra (TRANES), a modified version of the time-resolved emission spectra (TRES) is extensively used to develop a model-free approach for the analysis of excited-state energy transfer kinetics from a semiconductor nanocrystal to an oppositely charged molecular fluorophore.

The distribution of small molecules over the surface of semiconductor nanocrystals alters the conventional charge transfer mechanism. Therefore, we utilized a stochastic kinetic model to study charge transfer processes involving these nanocrystals and small quencher molecules. We observed a charge transfer process that can be evaluated by using the stochastic kinetic model, for high quencher concentration regime, while at low quencher concentrations, Stren-Volmer analysis seems to be appropriate.

This thesis delves into the mechanistic understanding of various excited state processes, involving in the new age materials. The mechanistic understanding is crucial for the modifications in existing methods and the rational design of next-generation devices.

CHAPTER 1

INTRODUCTION

The interaction of electromagnetic radiation with the matter has been studied by researchers in several optoelectrical applications.[1–5] When a molecule interacts with the light of a suitable wavelength, it absorbs. Absorption of the light occurs in the femtosecond timescale. As a result of absorption, the molecule enters the excited state from the ground state. Subsequently, these excited state molecules go back to the ground state through various radiative and non-radiative channels, which involve radiative as well as non-radiative pathways. Non- Radiative pathways involve the dissipation of energy in the form of heat, whereas the radiative pathways involve the emission of a photon. Generally, right after absorption, the molecule is excited to some higher vibrational levels of S_1 or S_2, as explained by the Frank Condon principle. Within the span of few picoseconds, the fluorophore relaxes to the lowest vibrational state of S_1 and this is known as internal conversion. Internal conversion is a non-radiative deactivation process. Among the radiative deactivation channels, fluorescence is the most common. It involves the transition of the molecule from the lowest vibrational level of the first excited state to the ground state without any change in the spin multiplicity (S_1 to S_0 transition). This relaxation is accompanied by the emission of a photon. The phenomenon was first observed by Sir John Frederick William Herschel in 1845 upon exposing a quinine solution to sunlight. Fluorescence takes place in the timescale of few nanoseconds.

The significance of fluorescence lies in its immense applications starting from imaging in biology to chemistry and material sciences. Fluorescence has huge importance in several detection techniques, flow cytometry, solar cells, DNA sequencing, forensics, are the few among many others.[6–11] Apart from internal conversion and fluorescence, there are other radiative and non-radiative processes which include intersystem crossing and phosphorescence. All these processes can beautifully be illustrated by the Jablonski diagram, named after Professor Alexander Jablonski. A typical Jablonski diagram is depicted in SCHEME 1.1.

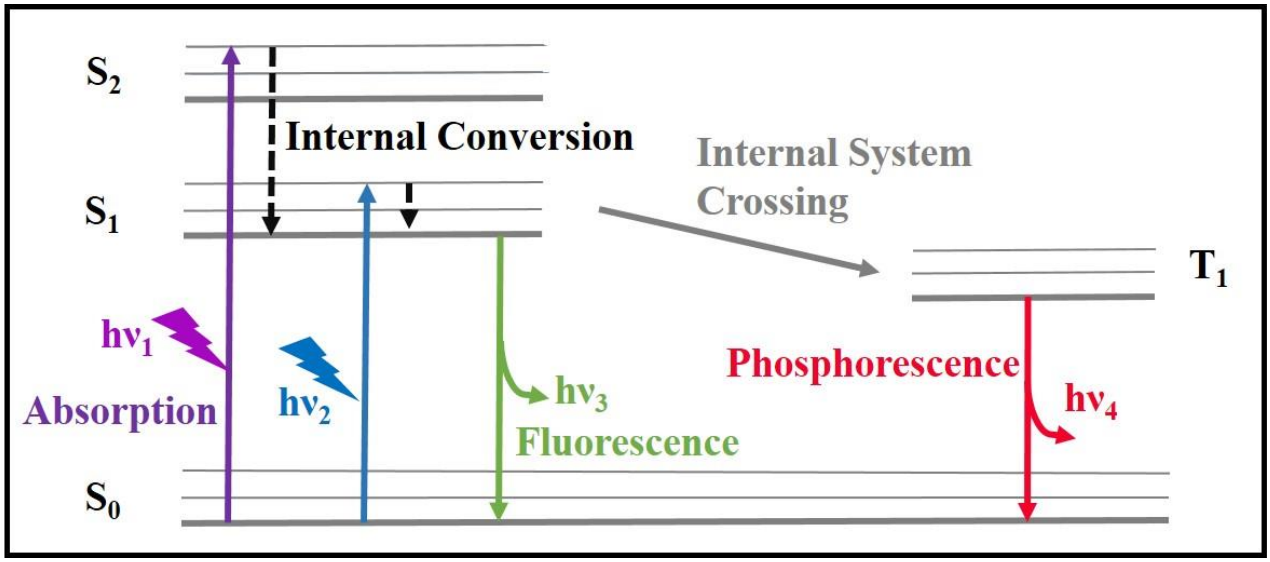

SCHEME 1.1. Jablonski diagram illustrating the absorption of a photon, followed by various relaxation (radiative/non-radiative) processes. [21]

The transition of a molecule from S_1 state to T_1 state is termed as intersystem crossing, which is a non-radiative process with a timescale of 10^{-8} to 10^{-3} nanoseconds. While the radiative relaxation of a molecule from the T_1 state to the S_0 state is known as phosphorescence. This is a forbidden transition induced by the heavy atoms present in the molecule/system. Phosphorescence is usually a slow process and the associated timescale is few microseconds to even seconds in a few cases.

The next part of this chapter a brief description of the various photophysical phenomenon such as Förster resonance energy transfer (FRET), Photoinduced Electron Transfer (PET), and the key concepts used in the thesis work such as Rotational anisotropy decay, Time Resolved Emission Spectrum (TRES), Time Resolved Area Normalized Emission Spectrum (TRANES), Quantum Dots (QDs) and their recent progress are discussed. The discussion is followed by a few case studies of QDs participating in FRET and PET processes. All these phenomena are widely studied in the present thesis work and their real applications are explored.

1.1 Excited-State Processes

After photoexcitation, the fluorophores may undergo various excited-state processes. Electron or hole transfer, energy transfer, proton transfer, photodissociation, conformational changes, and molecular motions, are a few examples of excited-state processes among many others. These excited state processes and their respective timescales are illustrated in SCHEME 1.2.

Mechanistic investigations of the fast processes illustrated in SCHEME 1.2 and associated timescales are of paramount importance.[12a,12b] Further studies, and analysis of experimental data using an organic dye in solvent provide an insight into the fundamental processes like solvent reorganization around a solute dipole, dynamic heterogeneity in quasi confined medium, micellization of surfactant molecules, the scaffolding of supramolecular assemblies, etc.[13–19]

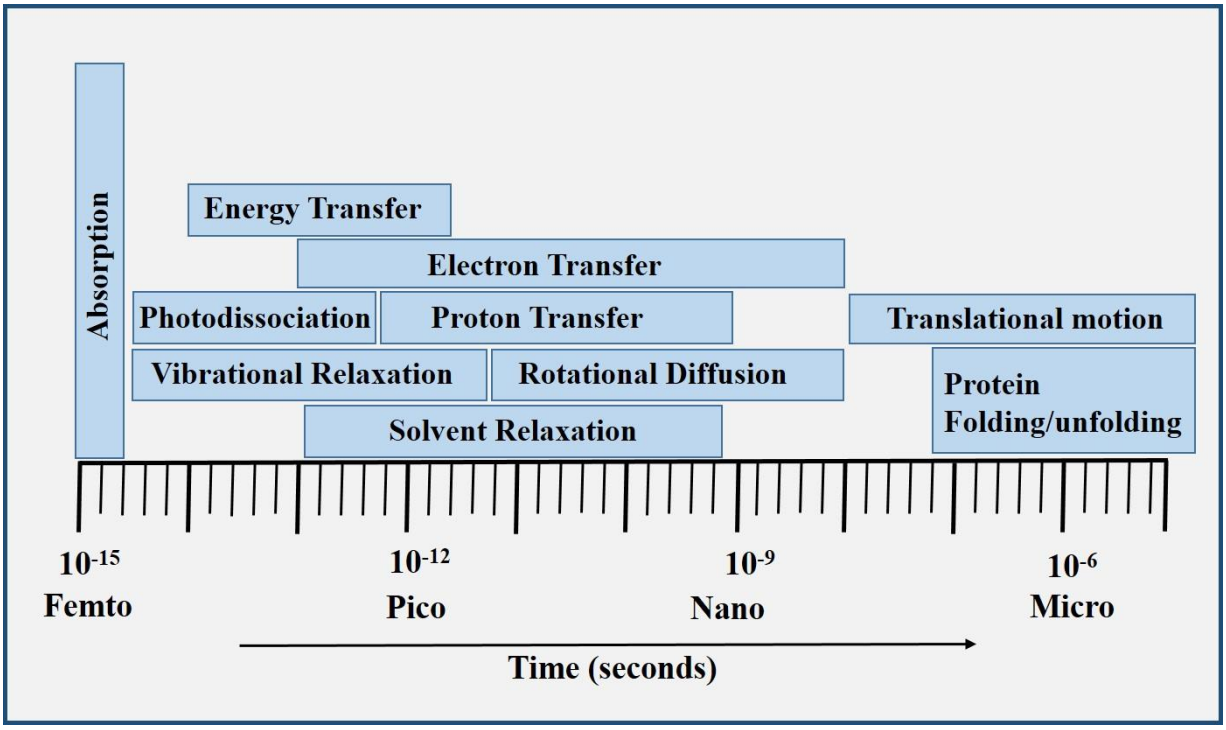

SCHEME 1.2. A schematic representation of several fast processes along with their respective timescales.

Among all the fast processes described in SCHEME 1.2, in this thesis, we have focused mostly on two excited-state processes namely, energy transfer and electron transfer processes for their widespread applications. Hence a detailed description of energy transfer and electron transfer is provided in the subsequent sections.

1.1.1 Förster Resonance Energy Transfer (FRET)

In FRET a nonradiative energy transfer takes place when the emission spectrum of a fluorophore (donor) overlaps with the absorption spectrum of another molecule (acceptor), residing at the proximity, which may or may not be a fluorophore itself. An efficient FRET requires the largest overlap in the energy profiles and the smallest separation between the donor and acceptor

molecule. The word Förster in FRET recognizes the contributions of a German physical chemist, Theodor Förster, in energy transfer studies.

1.1.1.1 Theory and Mechanism of FRET

In a FRET process, both donor and acceptor are considered to be point dipoles. This approximation has been proven to be a good fit for most of the FRET processes.[20] When electromagnetic radiation of suitable wavelength strikes the donor fluorophore, it absorbs and gets excited. During FRET the electron of the photoexcited donor relaxes back to the ground state and its energy is transferred non-radiatively to the acceptor molecule resulting in the excitation of the acceptor. FRET does not involve the emission of a photon from the donor rather it takes place non-radiatively through the dipole-dipole coupling. The excited state acceptor relaxes back to the ground state. If the acceptor is fluorescent then it emits, otherwise, the excess energy is released in the form of heat while returning to the ground state.. (SCHEME 1.3)

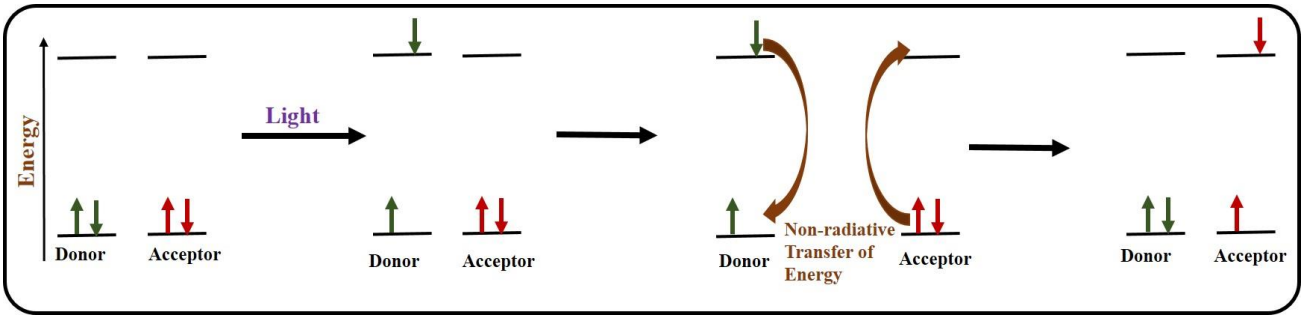

SCHEME 1.3. A pictorial representation of Resonance Energy Transfer between a donor-acceptor pair.[21]

The following equation represents the rate of FRET and can be obtained from the classical and quantum mechanical approaches.

$$k_{\mathrm{T}}(r) = \frac{Q_{\mathrm{D}}\kappa^2}{\tau_{\mathrm{D}} r^6}\left(\frac{9000(\ln 10)}{128\pi^5 \mathrm{N}\eta^4}\right)\int_0^\infty F_{\mathrm{D}}(\lambda)\varepsilon_A(\lambda)\lambda^4 d\lambda \qquad (1.1)$$

where Q_D represents the donor's quantum yield in the absence of acceptor, κ^2 is the orientation factor, τ_D is the lifetime of the donor in the absence of acceptor, *r* is the distance between the donor and acceptor molecule, N represents the Avogadro's number, η represents the refractive index of the medium.

$F_D(\lambda)$ represents the fluorescence intensity for $\Delta\lambda$ wavelength in the area normalized fluorescence spectrum of the donor. $\varepsilon_A(\lambda)$ is the extinction coefficient of the acceptor at $\Delta\lambda$ wavelength. The term $\int_0^\infty F_{\mathrm{D}}(\lambda)\varepsilon_{\mathrm{A}}(\lambda)\lambda^4 d\lambda$ represents the extent of spectral overlap between the donor's emission profile and the acceptor's absorption profile. The entire term $\frac{9000(\ln 10)\kappa^2 Q_{\mathrm{D}}}{128\pi^5 N n^4}\int_0^\infty F_{\mathrm{D}}(\lambda)\varepsilon_{\mathrm{A}}(\lambda)\lambda^4 d\lambda$ is represented in terms of the Förster distance as follows,

$$R_0^6 = \frac{9000(\ln 10)\kappa^2 Q_{\mathrm{D}}}{128\pi^5 N n^4}\int_0^\infty F_{\mathrm{D}}(\lambda)\varepsilon_{\mathrm{A}}(\lambda)\lambda^4 d\lambda \qquad (1.2)$$

From equation 1.1 and equation 1.2, the rate of FRET becomes,

$$k_T(r) = \frac{1}{\tau_D}\left(\frac{R_0}{r}\right)^6 \qquad (1.3)$$

1.1.1.2 Factors Affecting FRET

The rate and efficiency of FRET between the donor and acceptor depend upon several factors like the extent of spectral overlap between the donor's emission and acceptor's absorption, donor-to-

acceptor distance, the relative orientation of the transition dipoles of donor and acceptor, and the quantum yield of the donor.[21]

The relative orientation between donor and acceptor is elucidated by the orientation factor which is represented by, κ^2. The value of κ^2 ranges from 0 to 4 as the orientation changes from perpendicular to parallel. The average value of κ^2 is generally taken to be 2/3, which accounts for the rotational diffusion of randomized donors and acceptors right before the RET.[21] Similarly, a donor with a higher quantum yield will participate in more efficient RET compared to the ones with lower values of quantum yields.

The following sections will shed some light on how spectral overlap and donor-to-acceptor distance impacts the FRET process.

1.1.1.2.1 Effect of Donor-to-Acceptor Distance on FRET

The impact of distance on the rate of an energy transfer process is huge. The rate of energy transfer is inversely proportional to the sixth power of distance as given by equation 1.3. The physical significance of the Förster distance can be understood as the distance between donor and acceptor at which FRET efficiency is 50% (Figure1.1).

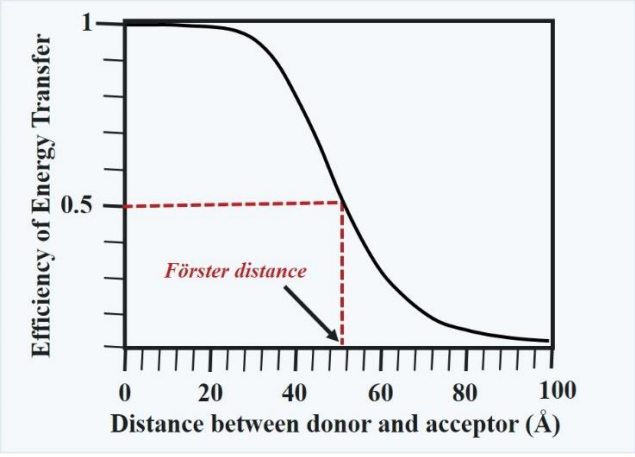

Figure 1.1. Graphical representation of variation in the FRET efficiency as the function of donor-to-acceptor distance. [21]

1.1.1.2.2 Effect of Spectral Overlap on FRET

As discussed in the earlier sections, the amount of spectral overlap between the donor's emission profile and acceptor's absorption profile influences the Forster distance which in turn affects the efficiency of a FRET process. Greater is the extent of spectral overlap between the pair faster and more efficient will be the FRET process.

Upon substituting the values of constants in equation 1.2, the relationship between Forster distance and spectral overlap can be mathematically represented as,

$$R_0 = 0.211\left[\kappa^2 \eta^{-4} Q_D J(\lambda)\right]^{1/6} \qquad (1.5)$$

Where κ^2 is the orientation factor, η is the refractive index of the medium, Q_D is the fluorescence quantum yield of the donor, and $J(\lambda)$ is the spectral overlap between emission of the donor and absorption of the acceptor.

A good spectral overlap results in an increased value of Forster distance which in turn results in a faster FRET [equation (1.1), and (1.2)]. One such spectral overlap is depicted in Figure 1.2 as an example.

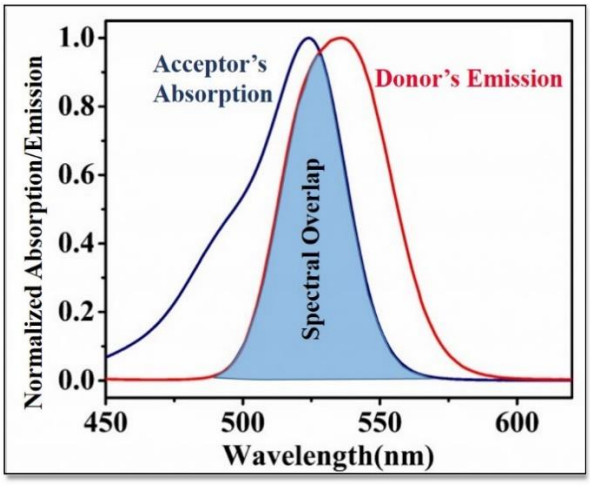

Figure 1.2. The blue shaded region represents the spectral overlap between the absorption profile of an organic dye, R6G, and the emission profile of a CdSe/ZnS core-shell quantum dot. [21]

The importance of spectral overlap is prevalent in every FRET-related study from designing FRET-based sensors to identifying the FRET among other quenching mechanisms.[22,23] For instance, Bawendi and Nocera reported a QD FRET-based ratiometric pH sensor.[22] The sensing mechanism was based on the changes in the extent of spectral overlap between the quantum dot emission spectrum and the dye's absorption spectrum. They used a pH-sensitive dye Squaraine whose absorption spectrum changes with the variation in the pH of the medium. The spectral overlap increased as the pH of the medium was lowered and resulted in an increased FRET efficiency and hence the sensing was carried out.

The importance of examining the spectral overlap while understanding a photoinduced excited-state process can also be realized by another study carried out by Stewart et al.[23] The group reported quenching in the PL of a series QDs linked to fullerene by peptides bridges. These QDs were emitting at different wavelengths and found to interact with fullerene by not only charge transfer but also FRET which could only be inferred after looking at the spectral overlap. Both the mechanisms, charge transfer and FRET, were reported to compete with each other. This competition was found to have a strong dependence on the extent of donor-acceptor spectral overlap as suggested by a series of photophysical experiments carried out by the group.

1.1.1.3 Applications of FRET

As can be seen from equation (1.1), the rate of FRET is inversely proportional to the sixth power of donor-to-acceptor distance. Hence FRET rates have been utilized to measure distances in various biological systems which in turn helps in understanding their structural biochemistry.[24–26] For example, a protein can exist in various forms like monomeric, tetrameric, helical, or random coil state depending on the surrounding conditions and the temperature. Every form will have a

different donor-acceptor (D-A) pair distance which can be calculated from the rate of FRET and in turn, the calculations of D-A distances will shed light on the structural details of the peptides.

Apart from the distance measurements, the presence or absence of FRET has also been utilized to gain important structural insights. For example, protein folding and unfolding have been studied from observing the presence or absence of FRET in many cases.[27–30] The occurrence of FRET in these studies has been linked to the conformation which brings the donor and acceptor closer in a way that can result in an efficient FRET.

Apart from the structural insights, FRET can be used as a tool in numerous sensing applications.[31–34] Ren et al. proposed a FRET-based sensor for the detection of H_2O_2 and glucose.[33] The sensor consisted of a QD based assay surface conjugated with horseradish peroxidase (HRP). To these conjugates, they added an acceptor dye-labeled tyramide molecules. FRET between the donor QD and acceptor dye switches on in presence of H_2O_2 or glucose. FRET happens in presence of H_2O_2 due to the covalent coupling of tyramide to the tyrosine functionality present on the side chains of commercial QD. FRET results in the overall fluorescence quenching of QD and the sensitization of acceptor dye molecules. The extent of sensitization is a direct measure of H_2O_2 concentration.

Algar et al. proposed a multi-donor concentric FRET system for biosensing applications.[34] They developed a QD-based assay linked to two fluorescent dyes A647 and A488. A647 acts as an acceptor in a multi-donor concentric FRET configuration having two donors QD and A488. A647 didn't have any absorption at 400 nm or 460 nm whereas QD exhibits a wide absorption range including both the wavelengths. On the other hand, A488 shows a good absorption at 460 nm with no absorption at 400nm. The extent of A647 sensitization between 400 nm and 460 nm was utilized to obtain a quantitative analysis of nanomolar concentrations of trypsin through the excitation ratio.

Many researchers have exploited FRET to study DNA and RNA dynamics.[35,36]

In the present thesis work, considering the importance of FRET, we have made efforts to contribute to the analysis of FRET by providing a model-free approach to extracting FRET timescales from complex lifetime profiles of donor and acceptor.

1.1.1.4 Existing literature methods for the analysis of FRET

One of the most used models for calculating different parameters related to the FRET is the Forster model. The model has already been described in much detail in the previous sections of this chapter.

In addition to this, many researchers have used the acceptor rise time analysis to calculate the FRET timescale and rate in a lot of their works.[37,38] In this approach, the rise time/growth time in the lifetime decay profile of the acceptor fluorophore is utilized to calculate the FRET timescale. For instance, in one of the works by K. Bhattacharyya and coworkers FRET was studied between coumarin153 and Rhodamine 6G in two different micelles namely, a neutral PEO_{20}–PPO_{70}–PEO_{20} triblock copolymer (P123) micelle and an anionic micelle sodium dodecyl sulfate (SDS). They reported a FRET timescale of 0.7 and 13ps for SDS micelle while 1.2 and 24ps for P123 micelle. These timescales of FRET were obtained from the rise time of the acceptor's lifetime decay profile which in this case was Rhodamine 6G.[38]

Apart from this, FRET between the quantum dot/rods and dye molecule has also been studied using Tachiya's stochastic model by A. Patra and coworkers. A detailed description of the model will be provided in the latter part of this chapter. They considered a Poisson distribution of Nile red dye molecules over CdS quantum dots/rods. The Poisson distribution of Nile red dye molecules was incorporated into the lifetime decay equation of CdS quantum dots/rods. This gave them the

equilibrium constant of the complexations between dye molecules and Cds quantum dots/rod along with the quenching rate per dye molecule. [39]

1.1.2 Photoinduced Electron Transfer (PET)

Quenching in the fluorescence of a fluorophore may be observed upon adding certain electron-rich or deficient molecules. These electron-rich or deficient molecules are called quencher molecules. The quenching can be attributed to various excited state processes as discussed earlier. One of those processes is PET. Unlike FRET, PET requires an orbital overlap between the participating donor-acceptor pair. On the other hand, PET is not limited by the spectral overlap between the donor's emission and acceptor's absorption. [40]

Given the appropriate extent of orbital overlap, in a typical PET process, quenching of the fluorescence results when the excited state fluorophore undergoes an electron transfer (to or from the quencher) before it relaxes back to the ground state. The electron transfer from the fluorophore or to the fluorophore takes place in the presence of an electron-donating or accepting moiety. The species giving out the electron is called the electron donor whereas, the species accepting the electron is known as the electron acceptor. After the electron transfer from donor to acceptor, the donor gains a positive charge while the acceptor gets a negative charge, and as a result, an excited state charge transfer complex is formed (SCHEME 1.4). This charge transfer complex may or may not emit while relaxing back to the ground state and in this process, and overall fluorescence from the fluorophore diminishes. SCHEME 1.4 illustrates a typical PET process.

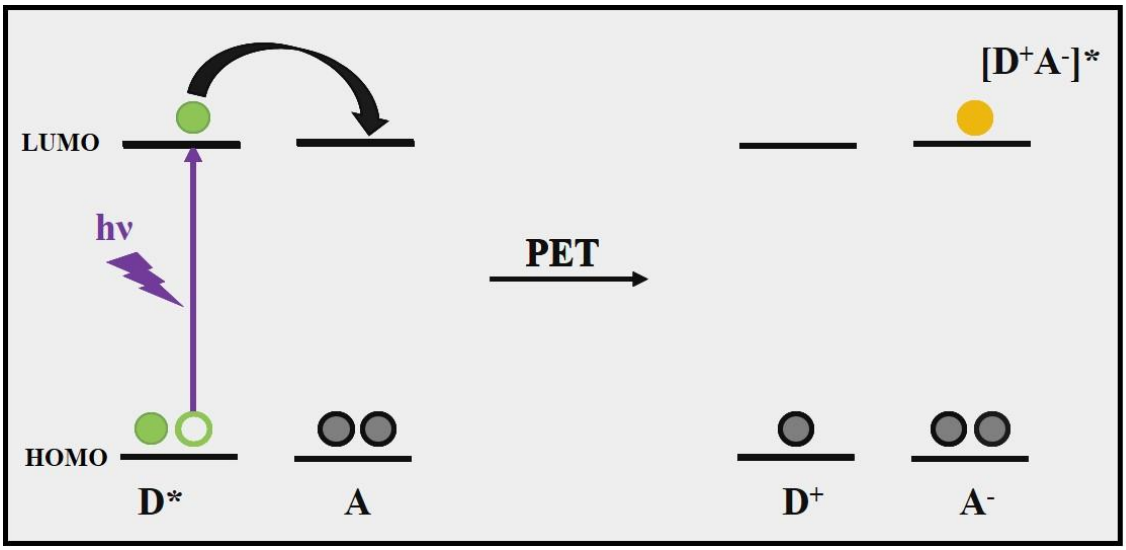

SCHEME 1.4. Schematic representation of a typical PET process involving a fluorescent donor and a quencher molecule. [21]

1.1.2.3 Thermodynamics of PET

Studying the thermodynamics of a PET reaction is of paramount interest as it provides insight into the quenching process and thereby the development of next-generation devices.[41–45]

In a typical PET process, an electron is transferred from donor to acceptor after the photoexcitation of either of them. PET results in the formation of an excited-state charge-transfer complex, $[D^+A^-]^*$. Photoexcitation of donor/acceptor enables the charge transfer to happen which was not possible in the ground state due to a positive chemical driving force associated with ground state PET. Solvation of the ions of the charge-transfer complex may further result in a decrease in its energy. This complex may emit in the form of exciplex or get quenched and relax back to the ground state.

Estimation of chemical driving force associated with a PET reaction can be obtained by the Rehm Weller equation as follows[46]:

$$\Delta G = E(D^+ / D) \; - \; E\left(A / A^-\right) \; - \Delta G_{00} - \; e^2 / \varepsilon d \qquad (1.3)$$

Where ΔG is the free energy change in the PET process.

$E(D^+/D)$ and $E(A/A^-)$ is the reduction potentials of donor and acceptor respectively. Since both are reduction potentials, the equation has opposite signs for them. The donor is getting oxidized while the acceptor is taking up the electron and getting reduced.

ΔG_{00} is the free energy change of S_0 to S_1 transition of the fluorophore (donor or acceptor).

The last term on the right is the coulombic attraction energy experienced by the ion pair following electron transfer reaction, ε is the dielectric constant of the medium, and d is the distance between the charges.

1.1.2.2 Applications of PET

Quenching of fluorescence of several organic dye molecules by small organic molecules like aniline (and its derivatives), indoles, amines, etc., via the PET process, is well documented in the literature.[47–51] A strong correlation between ΔG values and the rate of electron transfer is observed in these reports. More negative free energy values tend to result in faster PET. Linked donor-acceptor pairs also tend to result in a much faster quenching compared to free donor and acceptor due to the lack of control from diffusion as shown by several research groups.[52,53] In such cases, the length of linkage is also important as it affects the rate of PET quenching. The rate of PET decreases as the length of linkage increases.[52,53]

PET has emerged to be a powerful tool in structural biology to study protein kinetics that controls crucial biological functions. Quenching of tryptophan fluorescence is exploited to study the structure and kinetics of proteins.[53] While studying non-fluorescent DNA, fluorescent markers are used which take part in PET reaction and thereby provide the structural changes during a kinetic process. The extent of PET depends on the DNA base as well as on the structure and properties of

the fluorophore used. Among the four DNA bases, guanine tends to be the most efficient quencher due to its strongest electron-donating nature. PET has been studied in double-helical DNA. The dependence of lifetime and quantum yields of the oligomers on the base sequence provides an insight into the DNA structure nearby.[54–56]

PET has also been used in biosensing applications. Willner et al. exploited the PL quenching of CdSe/ZnS QDs to design DNA sensors and also to sense telomerase activity.[57] Along with the sensing of DNA Willner's research group has also utilized PET to design many other sensors for detecting explosives,[58,59] enzyme activity,[60] metal ions[61], etc. In recent times, PET quenching has also been studied via the single-molecule detection technique.[62,63] Conformational changes have been detected and explained by fluorescence blinking behavior in these experiments. The blinking behavior in these experiments was attributed to the PET that is favored by one conformation but not by the other conformations. Though other factors also result in fluorescence blinking, for example, the transition to the triplet state, which was ruled out based on the fast timescale of the blinking which does not support slow timescale of triplet transition.[63]

In the present thesis work, considering the tremendous potential of PET in real applications, we have dedicated two chapters (Chapter 5 and 6) to understand the PET mechanism in complex systems.

1.2 Time-Resolved Emission

The emission spectrum of a fluorophore is a graphical representation of fluorescence intensity as a function of emission wavelengths (nm). The most basic type of emission spectrum is the steady-state emission spectrum. The steady-state emission spectrum is the emission profile of a fluorophore that is obtained from the equilibrated excited state of the fluorophore. A continuous

beam of light is used as an excitation source and the emission is obtained from the excited state (in equilibrium) of the fluorophore. Due to the fast timescale of fluorescence s, as soon as the sample is excited, the steady-state is attained.

On the other hand, time-resolved measurements involve the use of a pulsed excitation source. The pulse width of which is kept much smaller than the average lifetime of the fluorophore, to obtain accurate time-resolved measurements. The graph of fluorescence intensity decay with time is plotted in a time resolved measurement. The time evolution of fluorescence is exploited by fitting with an exponential decay function to obtain the excited state lifetime. More details of these measurements are provided in the next chapter.

Time-resolved measurements provide an insight into a photophysical process. The timescale for this photophysical process is faster than the fluorescence lifetime of the reporter dye. In the subsequent subsections, the two kinds of time-resolved emission spectrum namely, Time-resolved emission spectrum (TRES) and Time-resolved area normalized emission spectrum, have been discussed.

1.2.1 Time-Resolved Emission Spectrum (TRES)

Fluorescence lifetimes may vary with the emission wavelength. This variation is due to various excited state processes of the fluorophore taking place during its stay in the excited state. In other words, as time progresses, due to the change in the energy of the excited state of the fluorophore, emission wavelength changes. This variation in the emission profile within the lifetime of the fluorophore can be captured in time-dependent emission spectra termed as “Time-Resolved Emission Spectra (TRES)”.[64]

The most common variation is due to excited state solvation, causing the increase of the lifetime at red emission wavelengths while shortened lifetime at blue emissions.[65] To visualize such changes in the emission profile of the fluorophore, right from the excitation of the fluorophore till the time it reaches an equilibrated excited state, TRES are generated. TRES estimates the timescale of the excited state process (which is solvation in this particular case) causing the emission peak shift.

Apart from the spectral shift, sometimes the evolution of new peaks is also observed in TRES indicating multiple distinct emissive states. These emissive states may or may not be dependent upon each other.[66,67] Hence studying TRES may provide a whole new perspective to the excited state analysis.

The procedure for the generation of TRES is provided in the subsequent chapter (Chapter 2).

1.2.2 Time-Resolved Area Normalized Emission Spectrum (TRANES)

TRES, as described in the previous section is a wonderful way to study the excited-state processes which involve the emission peak shift. Despite being a very popular technique, TRES has few limitations. The major limitation of TRES arises due to the natural excited state decay process of the fluorophore under study. The timescale of this natural decay process is entangled with the timescale of excited state kinetics of interest. The separation of these two is tedious at times. To overcome this limitation, N. Periasamy and coworkers proposed the use of TRANES which are area normalized TRES.[68] TRANES is the modified version of TRES. Compared to TRES, TRANES provides a better understanding of excited-state processes since the latter is independent of the excited state lifetime of the fluorophore.[68-74]

Mathematically, TRANES are obtained from area normalization of each TRES spectrum (Figure 1.3). A detailed description of the procedure of TRANES generation is provided in the next chapter. The area normalization results in a constant area under the curve for each TRANES spectra irrespective of the time. Since the area under the curve of an emission spectrum is proportional to the excited state population of the fluorophore, keeping it constant would mean that the decrease in the total population (intensity) due to natural excited state decay processes is virtually stopped. Hence, the effect of the natural excited state decay process can be eliminated and one can have a clearer picture of the process of interest.

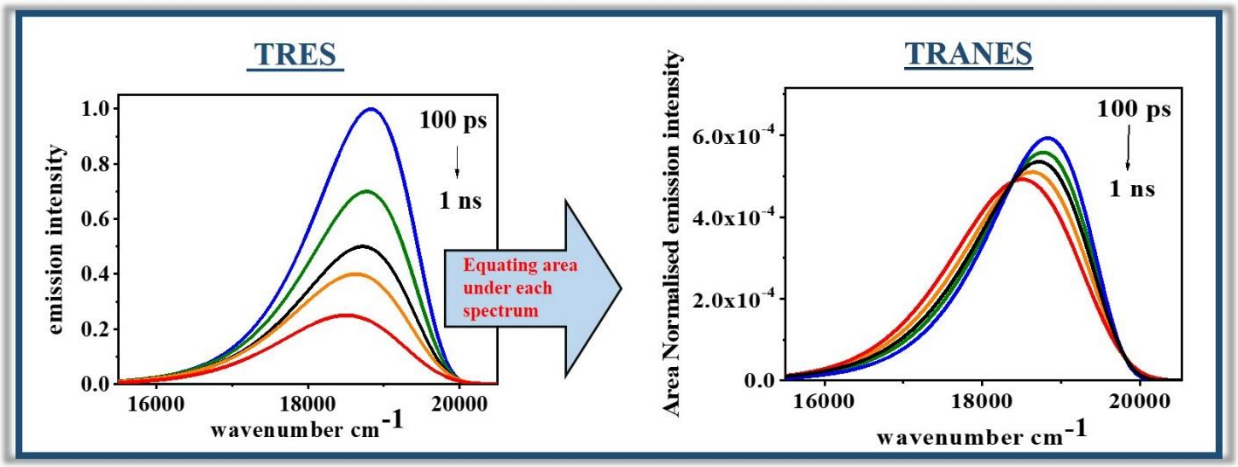

Figure 1.3. TRANES generation from TRES by area normalizing the TRES.[68]

N. Pariasamy and coworkers have already reported several advantages of TRANES over TRES. The intensity of TRES decreases as time progresses due to natural excited state decay processes, and the observation of the process of interest mixes with the natural excited state decay kinetics leading to false observations. For example, emission from two emissive species (differing in their lifetimes and emission peak positions) could be confused with the solvation phenomenon if only TRES is studied. While upon generating TRANES one can discriminate between the two processes. In the case of solvation, TRANES would provide a gradual shift in the spectrum peak

whereas in the case of emission from two species TRANES would lead to the appearance of an isoemissive point.

In the present thesis work, we have used the concept of TRANES to capture, visualize, and quantify bimolecular FRET in a QD-Dye FRET pair.

1.2.3 Applications of TRANES

Since the TRANES was reported for the first time by N. Pariasamy, researchers have been using it to study several excited-state processes.

S. K. Pal and coworkers studied the excited-state proton transfer and solvation dynamics of 1-naphthol in nanoscopic water clusters produced in hydrophobic solvent dioxane. They used TRANES as a tool to verify the two types of emissive species present in the water dioxanes mixture.[75] The presence of one isoemissive point in the TRANES generated for 1-naphthol in water dioxane mixture confirmed the presence of two emissive species: neutral naphthol and naphthol in anionic form. H. Pal and coworkers investigated H aggregate and H dimer formation of Coumarin 481 dye in an aqueous solution.[76] In their study, with the help of TRES and TRANES, they reported the emission from three different emissive species in the aqueous solution. According to their report, these three distinctly emissive species were kinetically decoupled. They concluded the three emitting species to be monomeric, dimeric, and trimeric Coumarine 481 in the aqueous solution. S. Ghosh and coworkers studied excited-state proton transfer kinetics of HPTS dye in reverse micelles. The group used TRANES as a tool to measure the timescale of proton transfer not only from the population depletion of the HPTS but also from the population growth of the deprotonated form of HPTS and both exhibited a similar timescale.[77]

Lin and coworkers reported the multiemissive states as the reason behind the origin of the excitation wavelength-dependent fluorescence of carbon dots. They concluded the presence of multiemissive states using TRES and TRANES analyses.[67]

1.3 Time-Resolved Fluorescence Anisotropy Decay

In any sample, the ground state fluorophores are randomly oriented. When a polarized excitation pulse falls upon this ensemble of fluorophores, the ones who have their transition moment integral aligned in the direction parallel to the excitation light, preferentially get excited. Due to this preferential excitation, the excited state of the fluorophores becomes partially polarized. Therefore, the emission obtained from these fluorophores will also be polarized to a certain extent. This extent of polarization of fluorescence is measured in terms of fluorescence anisotropy. As time passes, fluorescence anisotropy decays as the fluorophores get more time to reorganize themselves via rotational diffusion (SCHEME1.5).

To obtain a typical fluorescence anisotropy decay curve (anisotropy vs time curve), the decay of fluorescence emission intensity in the vertical ($I_{\parallel}$) and perpendicular direction ($I_{\perp}$) (to the direction of polarized excitation) are measured. Then the following equation is used to plot the Time-resolved fluorescence anisotropy decay curve

$$r(t) = \frac{I_{\parallel}(t) - G I_{\perp}(t)}{I_{\parallel}(t) + 2 I_{\perp}(t)} \qquad (1.4)$$

An additional instrumental correction factor G is introduced in the equation to eliminate the error induced due to the difference in the sensitivity of the instrument in the two different measurement directions.

For the samples, containing the fluorophores which rotate with a single correlation time, i.e. the fluorophore molecules depolarize through just one channel, the anisotropy decay curve can be expressed using the following equation

$$r(t) = r_0 \exp(-t / \tau_r) \qquad (1.5)$$

In the above equation, r_0 represents the zero-time anisotropy value. τ_r represents the rotational time of the fluorophore in the specific solvent. The r_0 value falls in the range of 0.2-0.4 depending upon the angle between excitation and emission dipole.

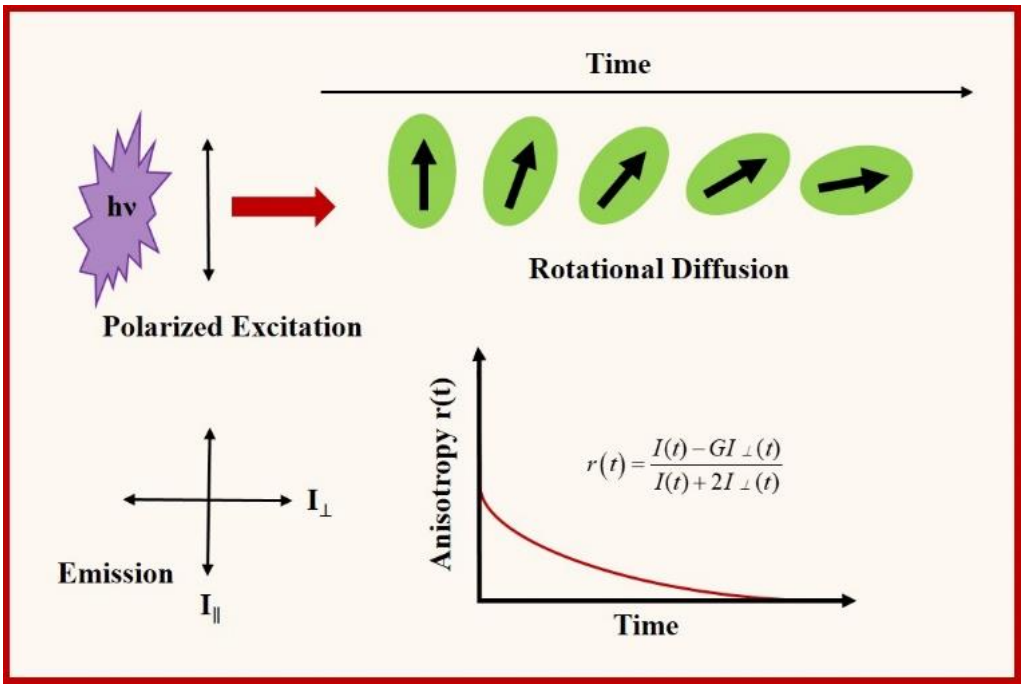

SCHEME 1.5. A schematic representation of a typical fluorescence anisotropy decay measurement. The fluorescence emission intensity is measured in the parallel and perpendicular direction to the polarized excitation. Due to the physical rotation of emission dipole over time, an anisotropy decay profile is obtained.[21]

The rotation of a fluorophore in a solvent is ruled by two of the main factors: hydrodynamic size and viscosity of the medium. Therefore, by knowing the rotational time of a fluorophore from the measured rotational anisotropy decay profile, one can get information about the hydrodynamic size and viscosity of the medium using the popular Stokes-Einstein-Debye equation,

$$\tau_r = \frac{4\pi\eta r_h^3}{3kT} \tag{1.6}$$

Here, r_h is the hydrodynamic radius of the fluorophore molecule, k is the Boltzman constant and T is the temperature at which the experiment is carried out, and η is the viscosity of the solvent medium.

The applications of fluorescence anisotropy study are not only limited to the size and the viscosity determination but various researchers have utilized the information to obtain important conclusions. For example, Lian and coworkers have used time resolved anisotropy decay measurements to confirm the binding of Rhodamine B (RhB) with CdS quantum dots.[78] They observed a significant increase (~8ns) in the rotational time of RhB in the presence of QD compared to that of free RhB (~0.2ns) indicating the binding between RhB and CdS QD.

In the present thesis work, we have also utilized the time resolved anisotropy decay measurements to obtain the size of QD and also other important insights in different experiments.

1.4 Quantum Dots

The demand for clean and renewable energy alternatives has motivated researchers of exploring solar energy over fossil fuels. Among all the trending clean energy alternatives, solar energy is one of the most abundant, safe, and green energy sources. Solar cells are used to harness solar energy

from the sun and utilize it to generate electricity.[79–83] Many researchers are putting constant efforts into the designing and development of efficient solar cell materials which include; single and polycrystalline cells, sustainable chalcogenides, Quantum Dots, organic photovoltaics, etc. Among all of these the quantum dots are proven to be one of the most potential candidates because of their astounding fluorescent properties like high fluorescence quantum yields and tunable optical and electrical properties.[84–88] These features possessed by quantum dots, make them a potential candidate not only for the solar cell applications but also in various fields including optoelectronics, photocatalysis, biology, etc.[89,90]

The energy levels of bulk semiconductors form bands: valence band and conduction band, such that, at zero kelvin, the valence band is filled whereas the conduction band is completely vacant. A specific energy gap divides the two bands. When an electron gets excited it reaches the conduction band and a corresponding hole is created in the valance band. As a result of this, an electron-hole pair is generated which is bound to each other from a finite distance. This bound electron-hole pair is called an “exciton”.

Quantum dots are made up of semiconductor materials. More precisely, quantum dots are nanoscale semiconductor materials in which the quantum confinement phenomenon comes into effect. These nanoscale semiconductors are called quantum dots because their nanoscale size results in the confinement or localization of their electrons to a point in space with no freedom in any dimension.[91]

Due to their nanoscale size and quantum confinement effect, quantum dots show properties that are intermediate to molecular and bulk properties. The following section sheds some more light on the quantum confinement effect and band gap properties in quantum dots.

1.4.1 Properties of Quantum Dots: Quantum Confinement and Bandgap

When the size of a nanoscale semiconductor approaches a range similar to that of exciton radius, quantum confinement effects become evident. Due to the confinement of their electrons to a point in space, the phenomenon is termed the quantum confinement effect.[91] As described in the earlier section, nanoscale semiconductors show a strong quantum confinement effect which increases bulk bandgap with a decrease in the size of the semiconductor. Due to the increase in bandgap the absorption band edge shifts to the blue side as shown in SCHEME 1.6.

Electronic transitions in the increased bandgap are responsible for the interesting and unique spectroscopic properties of the nanoscale semiconductor. In a real case scenario, apart from the states outside the bandgap (lying within the valence band and conduction band), there are states within the bandgap due to the defects present in the quantum dots.[92] These defects are the result of nonstoichiometry or unsaturated bonds.

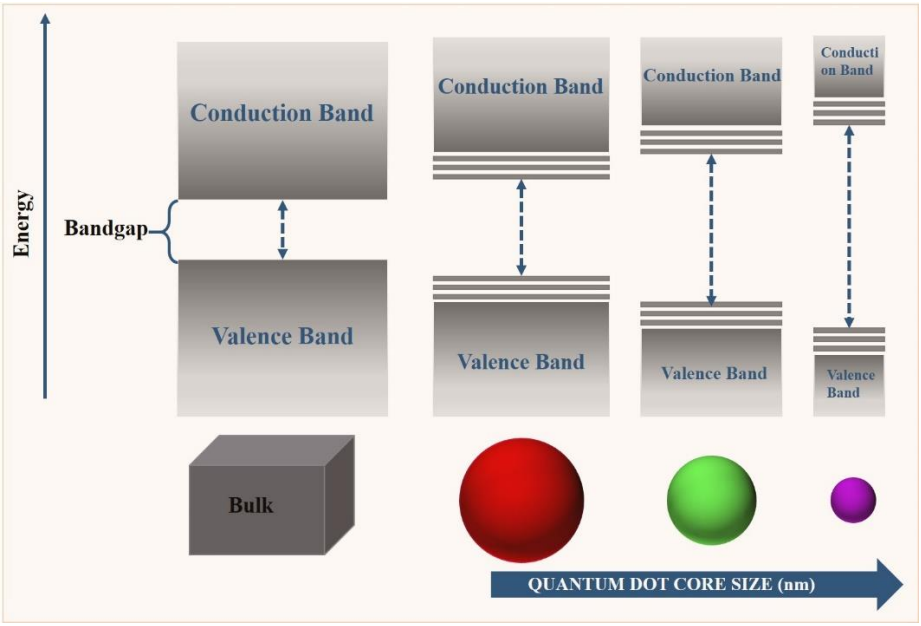

SCHEME 1.6. A pictorial representation of the effect of particle size on the energy bands and the bandgap of bulk semiconductors.[91]

Further, these nanocrystals can be designed or modified such that they can be used for a specific application. Size-dependent and tunable emission, narrow emission spectrum, high quantum yields and extinction coefficients, continuous absorption feature, and absence of photobleaching are some of the properties of these quantum dots which are responsible for their increasing demands in numerous applications including fluorescent imaging, solar cells, optoelectronic devices, etc.

In addition to the above-mentioned features of QDs, QDs also possess a huge surface-to-volume ratio, unlike organic dye molecules. This can be used as an advantage and various assemblies can be designed by surface engineering the QD.[93]

In the present thesis work, we have synthesized and studied various batches of semiconductor quantum dots. A brief introduction of literature methods of quantum dot synthesis is provided in the following section.

1.4.2 Synthesis of Quantum Dots

In the available literature, two fundamentally different approaches have been reported for the quantum dot synthesis namely, the top-down approach and the bottom-up approach.

1.4.2.1 Top-down Approach

As the name suggests, in a top-down approach, the nanomaterial is obtained from the bulk material. In a typical top-down approach, various tools and methods are utilized to cut the bulk semiconductor and bring it down to the nanoscale dimension (SCHEME 1.7). Powders from bulk materials have been obtained from the milling and grinding.[94,95] Apart from milling and grinding, methods like optical lithography, chemical etching, the use of electron or ion beams have also been implemented to obtain nanoscale materials from bulk.[96–98]

1.4.2.2 Bottom-up Approach

On contrary to the top-down approach, precursor molecules are utilized to create nanomaterials in a bottom-up approach (SCHEME 1.7). Both liquid-phase and gas-phase synthesis have been reported in the bottom-up approach.[99,100] In a gas phase method, the molecules of the nanomaterial to be synthesized are mixed in the gaseous phase. The synthesized material obtained in the gas phase is condensed to get nanoscale materials.

In the solution-phase method, the idea of arrested precipitation is deployed to obtain nanoscale materials. Upon starting at the molecular level in the solution, as the particle size grows to the nanoscale, further growth is banned using stabilizers.[101] Generally, surfactants are used as stabilizers. The stabilizers bind to the surface of growing particles and arrest further growth which may lead to the formation of bulk. Various ionic, as well as covalent surfactants, have been used as stabilizers. Other than the stabilizers, arresting has been achieved by using various synthesis templates such as micelles, membranes, zeolites, etc. drastic changes in temperature and pressure have also been reported to prevent undesired excessive growth.[102–104]

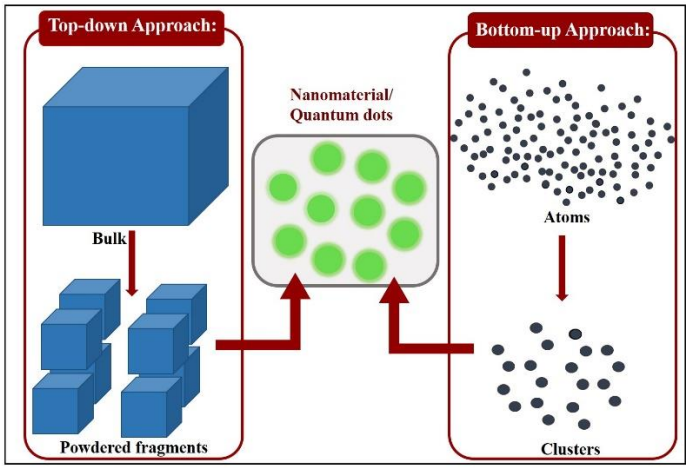

SCHEME 1.7. A pictorial representation of the top-down and bottom-up synthesis of nanomaterials. The left panel of the picture illustrates the top-down approach while the right panel illustrates the bottom-up approach.

1.4.3 Types of Quantum Dots

1.4.3.1 Core type Quantum Dot

Core type quantum dots are synthesized from a single metal component precursor, for example, cadmium QD, leads QD, zinc QD, chalconide QD (sulfur, selenium, tellurium, etc). To prevent aggregation, the surface of these quantum dots is covered with a stabilizer such as surfactants (SCHEME 1.8). The use of a stabilizer helps in providing photostability and solubility to the colloidal quantum dot solution. trioctylphosphine oxide (TOPO), Long-chain carboxylic acid, and amines have been used as stabilizers by various researchers across the globe.[105,106] A wide variety of core type quantum dots can be prepared in such a way that it covers the entire visible region. In the present thesis work, we have synthesized and worked with core type quantum dots to gain mechanistic insight into the Photo-Induced Electron transfer processes.

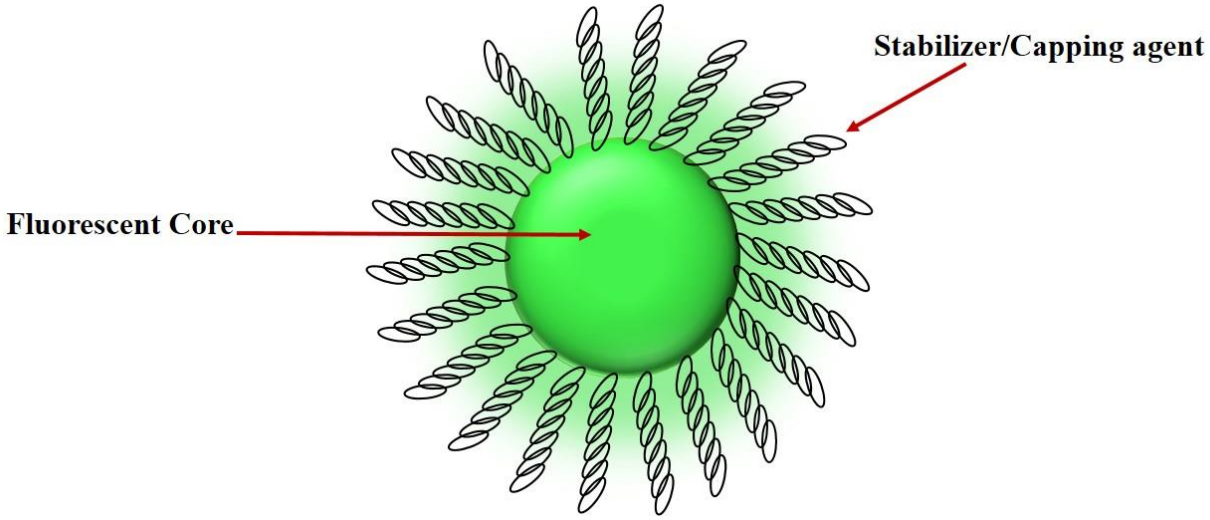

SCHEME 1.8. A pictorial representation of core type quantum dot with a fluorescent core and long-chain surface molecules acting as stabilizers or capping agent to prevent the aggregation of quantum dots.[105]

1.4.3.2 Core-Shell type Quantum Dot

Coating the core type quantum dot with an epitaxial-type shell of another semiconductor by growing it on the core surface, increases its photostability and passivates the surface trap states present at the core (SCHEME 1.9). Shell provides a physical barrier between the fluorescent core and the surroundings. This results in a core-shell type quantum dot with an enhanced fluorescence quantum yield compared to the core quantum dots. Shell also isolates the heavy metal core (for example Cadmium) from the external environment. This isolation is useful for its noncytotoxic application for biological purposes. In the present work, we have utilized core-shell quantum dots for a qualitative and quantitative study of the resonance energy transfer process by a new approach of data analysis.

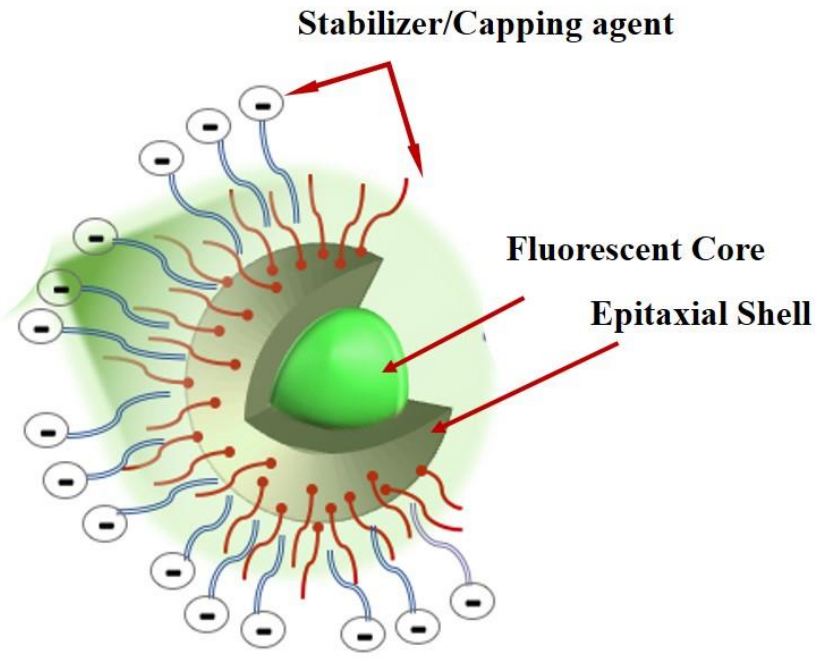

SCHEME 1.9. A pictorial representation of core-shell type quantum dot with a fluorescent core inside a non-fluorescent shell and long-chain surface molecules acting as stabilizers or capping agent to prevent the aggregation of quantum dots.

1.4.3.3 Alloyed Quantum Dot

Alloyed Quantum dots bring a different concept to the table, for tuning the bandgap. As discussed in the earlier subsections, size can be varied to tune the bandgap and inturn the optical properties of quantum dots. In recent advancements, alloyed quantum dots have given a new insight into tuning the optical properties by changing the composition of the quantum dot.[107–109] Alloyed quantum dots are prepared by alloying two types of semiconductors and have different band gaps. The optical properties can be changed by changing the composition of these semiconductors in the alloy.

1.4.4 Applications of Quantum Dots

Due to the interesting optoelectronic properties of QDs, they have gained much popularity among researchers across the globe. Recently Reisner et al. used CdS QD as a photocatalyst to convert formic acid into H_2 and CO.[110] Surface capped CdS QD was reported to selectively release H_2 whereas uncapped CdS QD selectively produced CO. H_2 has an important application as a clean energy source while CO holds significant industrial importance.

Similarly, clean energy demand has arisen the interest of the researchers in H_2O splitting to obtain H_2. Palomares et al. have investigated the usefulness of QDs as a photocatalyst in water splitting to obtain H_2 by examining the efficient and limiting reactions in the hydrogen evolution mechanism.[111]

Park et al. used CdS QDs embedded on the surface of SiO_2 beads as a photocatalyst for the regeneration of NADH.[112] The reported CdS-SiO_2 catalyst was capable of bearing repeated uses and found to have high catalytic activity.

1.5 Förster Resonance Energy Transfer involving quantum Dots

As described in the previous sections of this chapter, FRET has become a very important tool in biology as well as in chemistry. In a couple of decades, researchers worldwide have performed various FRET experiments involving quantum dots owing to their novel optical properties and easy synthesis methods. Among all the FRET experiments performed with QDs, depending upon the spectral properties of the interacting species, QDs have played roles of the donor as well as an acceptor. QDs have been used as energy donors for a wide range of organic dyes, fluorescent proteins/polymers, metal nanoparticles in several FRET experiments.[113] The invincible popularity of QDs as donors in the FRET systems can be explained in terms of its narrow and tunable emission which allows easy tailoring of the spectral overlap. Unlike the narrow emission spectrum of QDs, the absorption spectrum of QDs is quite broad. Again this broad absorption can be advantageous for a FRET donor as it provides the researcher with the freedom to choose an excitation wavelength for donor QD such that direct excitation of the acceptor could be avoided. Additionally, the large surface area of QDs (which is lacked by an organic fluorescent dye molecule) allows the interaction of a single QD donor to multiple organic dye acceptor molecules leading to an efficient FRET process. For example, Tachiya and coworkers have considered a passion distribution of N acceptor molecules over the surface of a single quantum dot.

On the other hand, QDs have also been implemented as FRET acceptors in various FRET assemblies consisting of fluorescent polymers, rare earth metal chelates, and other QDs as donors.[114–119]

1.6 Photoinduced Electron Transfer involving Quantum Dots

Photoinduced electron transfer is an underlying phenomenon in most energy conversion devices as the absorption of light results in the generation of free charge carriers. Increased green energy demands have led researchers to design and modify novel photovoltaic devices.[79,120–127] Constant efforts are being put by researchers around the globe to develop materials for next-generation photovoltaic devices with improved efficiencies. One of these new generation materials is quantum dots. The size-dependent electronic structure of quantum dots has made them a highly potent candidate for various energy conversion devices. For the efficient use of quantum dots in solar energy conversion devices, an in-depth mechanistic understanding of PET involving quantum dots is important.

A significant amount of research has been performed to understand the mechanistic aspects of PET in quantum dots under different environments and circumstances. Kamat and co-workers have reported various instances and in-depth analysis of PET between QDs and semiconductor materials.[128,129] Later on, they reported PET between CdSe quantum dots of different sizes and metal oxide nanoparticles of ZnO, SnO2, TiO2. In this work, the PET from a single quantum state of quantum dots to a continuum electronic state of metal oxides was linked to the strong chemical driving force.[128]

Lian and coworkers studied the interfacial electron transfer between CdS quantum dot and rhodamine B molecule attached to its surface. In this work, they reported multiple exciton generation and an ultrafast PET component in the range of a few picoseconds.[78]

Later on, Tachiya and coworkers studied the complexity caused by quantum dot structure and the interaction of multiple molecules with a single quantum dot in a resonance energy transfer process.

They assumed a poison-type distribution of multiple quencher molecules over a single quantum dot surface.[39]

Ghosh et. al. studied the PET involving various core/core-shell type quantum dots and small organic molecules. They studied the different regimes of PET kinetics (stationary and nonstationary) and also, the effect of the size of the QD, the chemical driving force, inherent quenching sites, and diffusion to the overall PET rate of the system.[131,132] In the present thesis work, we have utilized the knowledge of reported literature and attempted an in-depth mechanistic understanding of PET involving single QD and multiple quencher molecules. We thoroughly examined the different PET processes using various models and commented on the best choice of model one should adopt in a given scenario.

1.7 Isothermal Titration Calorimetry (ITC)

With the help of experimental heat measurements by the ITC, one can obtain the values of enthalpy (ΔH), binding constant (K_a), entropy, and stoichiometry of different simple and complex systems. Therefore one can have a complete picture of all the thermodynamical aspects corresponding to a binding process in a complex system.

Using ITC researchers across the globe have studied vast surfactant assemblies including aggregation of surfactants to form micelles,[133] polymer-surfactant interactions,[134] the interaction between surfactants and colloidal particles,[135,136], etc. These studies help know the effect of the hydrocarbon chain and the polar headgroup on the process of micellization along with the structural insights of polymer surfactant assemblies.

Apart from the surfactant assemblies, ITC has also been employed to study various biomolecular interactions with small molecules. For example, Gerhard Klebe et al. used ITC to study the effect

of water displacement and rearrangement on the thermodynamics of ligand binding taking thermolysin protein as a model system.[137]

Various protein-nanomaterial interactions have also been studied using the ITC technique. K. Mohr and coworkers used ITC to study the interaction of human blood plasma proteins and HSA to hydroxyethyl starch (HES) nanocapsules to form soft protein corona.[138]

We have utilized the ITC technique throughout this thesis to investigate and obtain thermodynamic parameters of the complexation/binding between the small quencher and nanoparticle surface.

1.8 Scope of the Thesis

The present thesis work is divided into a total of six chapters. The first two chapters are introduction and instrumentation chapters respectively. The rest four chapters are work chapters. The introduction chapter has been outlined to provide the basic knowledge of concepts, relevant to the thesis work, and their state of the art. The second chapter which is the instrumentation chapter is designed to provide an overview of the instrumentation used to carry out the thesis work and their working principles.

The rest four chapters are comprised of the strategic workflow. In these four chapters, we have studied two of the various excited state processes namely, Förster resonance energy transfer and photoinduced electron transfer involving nanoscale semiconductor systems known as "Quantum dots".

In the third chapter, we have studied FRET in a core-shell QD and an organic dye molecule "R6G" FRET pair. This FRET study was carried out by proposing a new approach using the already existing TRANES method. Our proposed method is model-free and a useful tool to capture,

visualize, and quantify a FRET process. The method can be implemented in any FRET system. QD-R6G system was taken just as a model system in this case.

Apart from quantifying the FRET timescale, TRANES were also used to investigate the effect of donor-acceptor lifetimes on the FRET analysis. A set new of TRANES was simulated for this purpose and the details of the same are provided in the fourth chapter.

In the last two chapters, a detailed discussion of PET between synthesized CdTe Quantum dots and two small quencher molecules: Dinitrotoluene and N-methylaniline, is provided. ITC technique was utilized to explore the interaction between these small quencher molecules and the QDs. With the help of ITC and other fluorescence studies, two types of complex formation were observed: emissive and non-emissive complexes. A stochastic kinetic model along with the classical Stern-Volmer analysis was used to provide a complete picture of the PET process.

CHAPTER 2

Adopted Methodologies and Instrumentation

In this chapter, the various instrumental, as well as theoretical methods adopted for the present research work will be discussed briefly. Instrumental methods explain the working principle of various instrumental techniques, while theoretical methods describe the data analysis part of the experiments carried out using different instruments.

Various instrumental techniques have been used to study different excited-state processes. As this thesis mainly focuses on excited-state processes, fluorescence-based techniques have been extensively used including steady-state measurements, time-resolved fluorescence measurements, rotational anisotropy measurements, and fluorescence correlation spectroscopy. This chapter will also talk about the techniques like ITC (isothermal titration calorimetry) to measure heat changes and binding constant of a reaction, and DLS (Dynamic Light Scattering) and HR-TEM to measure particle size of the synthesized Quantum Dots.

On the other hand, various theoretical methods, for an in-depth data analysis and understanding of the processes, have been adopted. This chapter will also discuss the methods including the construction of Time-Resolved Emission Spectra and Time-Resolved Area Normalized Emission spectra, calculation of Quantum Yields (QY) of fluorescent materials used, and energy band calculations for the synthesized quantum dots.

Along with the instrumental and theoretical methods, this chapter also discusses the materials and reagents used in carrying out the present research work.

2.1 Materials and Reagents

In chapters 3 and 4 of the present thesis, we have used negatively charged water-soluble CdSe/ZnS quantum dot as a donor in our FRET analysis. These quantum dots were purchased from Invitrogen-Thermo Fisher Scientific (Catalog number-Q21341MP, Lot-1705907). The dilute solutions of these quantum dots were used without further purification. All the experiments were performed within one month of the purchase. The spectral signatures, fluorescence quantum yield, and the particle size of the quantum dot remained stable even after six months from the date of receiving the sample. The Rhodamine-6G dye (99%, used as an acceptor) was purchased from Sigma-Aldrich. All the experiments were performed in the aqueous solution of MilliQ water from Merck Millipore.

In chapters 5 and 6, we used tellurium powder (99.8%), cadmium acetate dihydrate (>98%), dodecylamine (98%), trioctylphosphine (97%), HPLC grade methanol (99.9%), and toluene (99.8%) for the synthesis and purification of CdTe quantum dots. 2,4-Dinitrotoluene (97%) and N-methylaniline (>99%) were used as quenchers in PET studies of the synthesized CdTe quantum dots. All the above-mentioned chemicals were procured from Sigma-Aldrich and used without further purification.

2.2 Steady-State Absorption Measurements

Steady-state electronic absorption spectra of the fluorophores and other compounds are widely used in the present research. The absorption experiments were carried out using dilute solutions (~ $10^{-5} – 10^{-6}$ $molL^{-1}$) of the samples to be studied and these samples were placed in a 1cm path length

quartz cuvette cell. All these steady-state absorption measurements were performed using the Jasco V-730 spectrophotometer region with a 0.17nm of wavelength resolution and 0.005 of least detectable Optical density. The optics of an absorption spectrophotometer are provided in SCHEME 2.1.

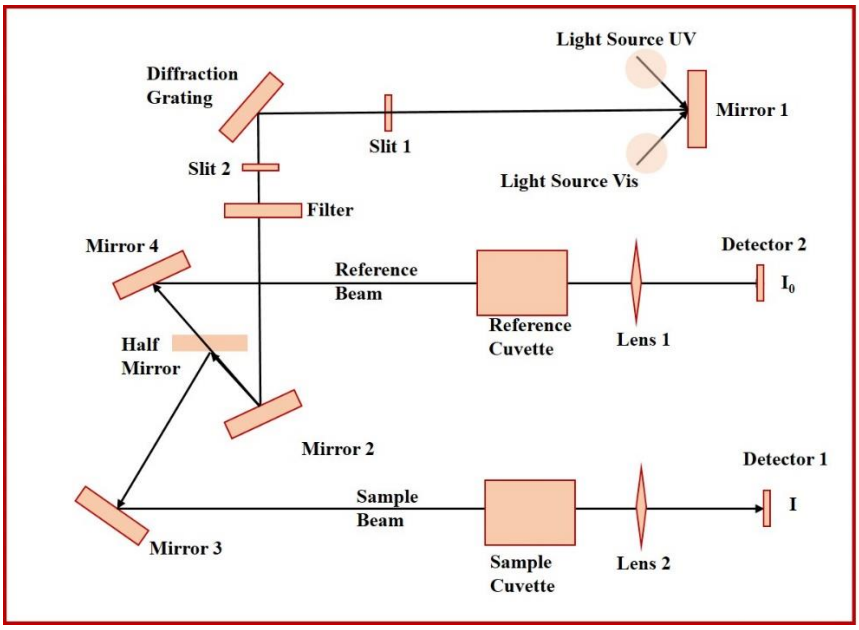

SCHEME 2.1. Schematic representation of the absorption spectrophotometer operable in UV to NIR region.

2.3 Steady-State Fluorescence Measurements

Steady-state fluorescence measurements were extensively used in the present research work. The spectra were obtained using a Cary Eclipse fluorescence spectrophotometer with a xenon lamp (Agilent Instruments) as the excitation source. An excitation beam from the Xe lamp is incident on the excitation monochromator to irradiate the sample (SCHEME 2.2). A beam splitter sends a part of this excitation beam to the detector. The emission monochromator at the perpendicular direction to this excitation source receives the emission light from the irradiated sample. A

photomultiplier tube (Hamamatsu; R-928F) collects the emitted photons of a particular wavelength (as selected by the emission monochromator) from the sample under investigation. The spectrum is corrected by the instrument to eliminate the instrumental response from the excitation and emission monochromators and the photomultiplier.

All the samples were placed in 1cm path length quartz fluorescence cuvette cells which were then put in the sample chamber of the instrument one by one.

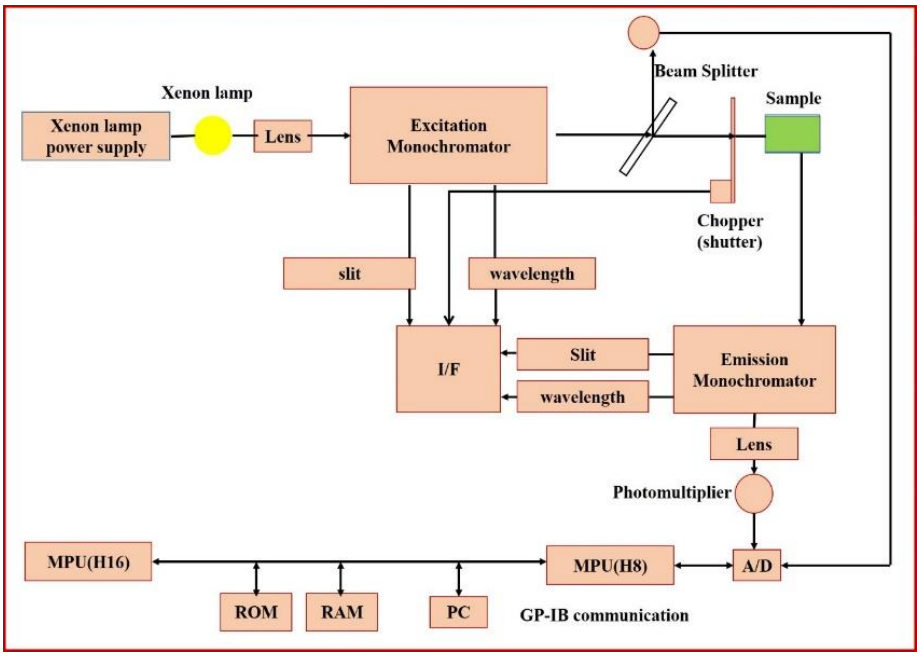

SCHEME 2.2. Schematic representation of the optics of a fluorescence spectrophotometer with Xenon lamp as the excitation source and photomultiplier tubes as a detector.

2.4 Time-resolved Fluorescence measurements

Time-resolved fluorescence measurement reveals a lot about an excited state process when compared to the steady-state fluorescence emission measurement. Time-resolved fluorescence measurement sheds light on the dynamic processes going on in the system under investigation

while steady-state fluorescence measurement provides an equilibrium picture of the sample under investigation.

Once the sample is excited to the higher electronic state, the population of the fluorophores in this higher electronic state decays as time progresses. This population decay is attributed to the radiative and various non-radiative decay processes of the excited state. The small change in the excited state population of molecules (*n(t)*) at any time *t*, is related to the rate of radiative (k_r) and non-radiative (k_{nr}) decay constant given by the following equation[21,139],

$$\frac{dn(t)}{dt} = (k_r + k_{nr})n(t) \qquad (2.1)$$

The number of molecules in the excited state at any time t is proportional to the fluorescence intensity of the sample at the same time t. Therefore, the time-dependent fluorescence intensity I(t), denotes the excited state population and exhibits an exponential decay as time progresses.

$$I(t) = I_0 \exp(-t/\tau) \qquad (2.2)$$

The above equation τ represents the fluorescence lifetime of the molecule. The fluorescence lifetime of the molecule is the reciprocal of the total decay rate of the excited state population (radiative and non-radiative).

I_0 is the excited state population right after the excitation pulse is sent (theoretically, at zero time after the excitation).

This section described the theoretical aspect of the lifetime while for the experimental measurements of these lifetimes “Time correlated Single Photon Counting (TCSPC)” technique was used which is described in the subsequent section.

2.4.1 Time-Correlated Single Photon Counting

The basic task of the TCSPC setup is to measure the time difference between the short excitation pulse and the first detected photon from the sample. These time differences are stored in the form of a histogram. When this same event is performed repeatedly, the obtained histogram represents the lifetime decay profile of the sample.

For this purpose, the instrument uses a pulsed laser excitation source. In the present thesis, we have used a series of picosecond diode lasers emitting laser pulses of ~375nm, 405nm, and 445nm. These lasers have a very short pulse width of ~90ps. The emitted fluorescence intensity from the sample is adjusted so that only one photon is detected per 100 excitation pulses.[21]

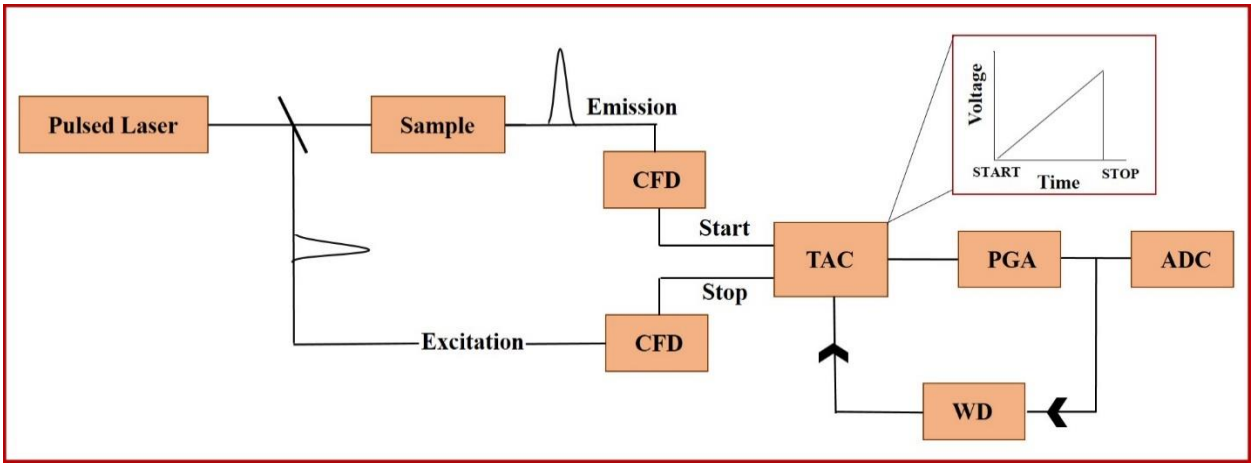

SCHEME 2.3. Schematic representation of a typical TCSPC setup and the working principles.[21]

To begin with, the sample is excited via the desired wavelength pulsed excitation laser (SCHEME 2.3). A part of the pulsed excitation is directly sent to the constant function discriminator (CFD). CFD accurately measures the arrival time of the pulse. As soon as the CFD passes this signal to the time to amplitude converter (TAC), it generates a voltage ramp. This pulse acts as the start signal for the TAC. The second part of the pulsed excitation is sent to the sample from where a single emitted photon is detected and the accurate time of the arrival of this photon is again

measured by another CFD, which further sends a single to TAC to stop the voltage ramp. This pulse acts as the stop signal for the TAC. The information is stored in TAC (in the form of voltage), is proportional to the time difference between the excitation and emission pulses.

A reverse mode TCSPC just does its job in a reverse manner. It assumes the start pulse to be the one from the sample (the single emitted photon) and the stop pulse to be the one directly sent from the excitation source. All the experiments were performed using a reverse mode TCSPC from Edinburgh Instruments (model OB-920).

To obtain better signals the voltage obtained from TAC is amplified using a programmable gain amplifier (PGA). This amplified signal is converted to a numerical value with the help of an analog-to-digital converter (ADC). The rest unwanted false noise signals are reduced with the help of a window discriminator.

This can be considered as one event and many such events are repeated several times and stored in a multichannel analyzer (MCA), which results in the desired histogram of decay with the number of photon counts on the y-axis and time difference on the x-axis.

2.4.2 TCSPC Lifetime Data Analysis

TCSPC setup can accurately provide the lifetime of only those fluorophores for which the lifetime decay profile is longer than the excitation pulse.

An excited state emission decay profile [P(t)] of a sample is obtained via TCSPC. Subsequently, it is convoluted with the excitation lamp profile [I(t)]. All together both these functions form a sample response function I(t). This fluorescence lifetime [F(t)] of the fluorophore must be

deconvoluted from the lamp profile [Q(t)] to obtain the actual fluorescence lifetime of the fluorophore. To do so the lamp profile was recorded in every experiment in the form of IRF, using a scatterer solution in the TCSPC setup.

The time-resolved fluorescence intensity decay profile obtained from TCSPC can be expressed in the following form:

$$F(\mathrm{t}) = \int_0^{\mathrm{t}} I(t')P(t-t')dt' \qquad (2.3)$$

The above convolution integral is fitted into the raw experimental data [X(t)] using the Marquardt-Levenberg algorithm which is an iterative nonlinear least square method. The best-fitted parameters obtained represent the actual lifetime decay profile of the fluorophore free from the instrument response function. A sufficient number of data points must be obtained to perform the least square fittings. *F(t)* and *I(t')* are obtained experimentally.

Marquardt-Levenberg algorithm is an iteration procedure that searches for the best-fit parameters by controlled and directed minimization of the χ^2 value (known as "goodness of fit") as follows.

$$\chi 2 = \sum_k W_k^2 \frac{[F_k - X_k]^2}{n}$$

The index k represents the individual data point to be fitted and the summation expands over all these data points. W is the weighting factor. It depends upon the type of noise specific to the data which is inherited from the measurement method. n is the total number of free parameters The deviation of the points is expressed in the form of χ^2. The low value of χ^2 (between 1.00 and 1.20) represents a good fit. Many iterations are carried out to obtain a good fit.

2.4.3 Time-Resolved Emission Spectra (TRES) and Time-Resolved Area Normalized Emission Spectra (TRANES)

Time-resolved emission spectra are the series of fluorescence emission spectra obtained at various time intervals in the range of hundreds of picoseconds to a few nanoseconds depending upon the fluorophore lifetime. Each TRES spectrum represents the emission profile of the sample at a given time t.

The construction of TRES can be performed using the information from both steady-state fluorescence measurements and fluorescence lifetime measurements of the sample at different wavelengths, following the method first proposed by Maroncelli and Fleming.[140] In this method, the steady-state intensity at a given wavelength is combined with the fluorescence lifetime of the sample at that wavelength to obtain the final TRES spectrum. Covering the entire region of the emission spectrum of the fluorophore, fluorescence lifetimes are recorded at different emission wavelengths, with a 10nm, interval typically. To proceed further, the time-integrated intensity is obtained mathematically, as follows[140]

$$A(\lambda) = \frac{I_{ss}(\lambda)}{\int_0^\infty \sum_j a_j \exp\left(-t/\tau_j\right)} \tag{2.4}$$

Here, $I_{SS}(\lambda)$ is the steady-state fluorescence intensity at a wavelength λ, obtained from steady-state emission spectrum, and τ_j is the excited state fluorescence lifetime of the fluorophore and the number of exponents in the lifetime is represented by j.

The multiplication of integral function with lifetime function will provide the wavelength-dependent fluorescence intensity at a time t as follows,

$$I(\lambda, t) = \frac{I_{SS}}{\sum_j a_j \tau_j} \sum_j a_j \exp\left(-\frac{t}{\tau_i}\right) \quad (2.5)$$

This equation provides various intensity points associated with the wavelengths for a given time t. These points can further be fitted using a lognormal fitting function to obtain a clear picture of the fluorescence emission profile of the fluorophore at a given time t. the best-fitted curve represents the TRES at time t. The lognormal fitting function can be given as follows

$$y(x) = \frac{b_i}{x - a_i} exp(-c_i^2)\, exp[-\frac{1}{2c_i^2}\{ln(\frac{x-a_i}{b_i})\}^2] \quad (2.6)$$

Where $a_i = x_i^0 - H_i\left(\frac{\rho_i}{\rho_i^2 - 1}\right)$; $b_i = H_i\left(\frac{\rho_i}{\rho_i^2 - 1}\right)\exp(c_i)^2$; $c_i = \frac{\ln(\rho_i)}{\sqrt{2\ln 2}}$

In the above equations, x_i^0, H_i & ρ_i are the emission peak position, FWHM (full width at half maximum) and asymmetric factor of the spectrum of i^{th} emitting species.

Similarly, a set of fluorescence emission spectra can be generated and fitted using the lognormal fitting function as given in equation 2.6 for different times and referred to as TRES. TRES has been extensively used to study many excited state processes, one of them being the excited state solvation dynamics.

On the other hand, TRES has certain limitations, for example, the intensity of TRES decreases due to the natural excited state decay processes. To overcome this limitation, we have utilized TRANES in our studies. The method TRANES was first proposed by Periasamy and co-workers.[74]

TRANES is the modified version of TRES. To obtain TRANES each of the TRES spectra is area normalized as follows:

$$Time\ Resolved\ Area\ Normalized\ Emission\ Spectrum\ at\ time\ t = \frac{Emission\ Spectrum\ at\ time\ t}{Area\ under\ the\ emission\ spectrum\ at\ time\ t}$$

The physical significance of performing this normalization is that the excited state population of the system under investigation is kept constant so that the natural excited state decay process can be stopped virtually and the processes of interests can be studied in a better and clearer way, free from natural excited state decay process.

2.5 Time-Resolved Fluorescence Anisotropy and Rotational Dynamics

Fluorescence anisotropy studies have been carried out at various points in this research work to obtain the hydrodynamic size and other useful information. All the fluorescence anisotropy experiments were performed using TCSPC from Edinburgh Instruments (model OB-920).

To measure the anisotropy, fluorescence intensity is collected first in the direction parallel to the polarized excitation ($I_{\parallel}$) and subsequently in the direction perpendicular to the polarized excitation ($I_{\perp}$). The obtained values are used in the following expression of fluorescence anisotropy,[140]

$$r(t) = \frac{I_{\parallel}(t) - GI_{\perp}(t)}{I_{\parallel}(t) + 2GI_{\perp}(t)} \qquad (2.7)$$

Here, G is the instrumental correction factor since the sensitivity of the instrument in the parallel and perpendicular directions is not the same. The value of G in this our work is obtained by the

tail matching method using a standard dye (Coumarin 153) which rotates fast and smooth in a simple solvent like methanol or ethanol.

The above expression (equation 2.7) describes an anisotropy decay with time for a spherical fluorophore molecule, which depolarizes through molecular rotation, this decay of anisotropy can be fitted with a simple exponential function as

$$r(t) = r_0 \exp(-t / \tau_r) \qquad (2.8)$$

Here, r_0 is the initial anisotropy value, τ_r is the rotational diffusion time of the fluorophore in the corresponding solvent.

2.6 Isothermal Titration Calorimetry (ITC)

ITC is a technique employed to measure various thermodynamical aspects of a reaction. The technique is mostly used to study heat changes associated with the interaction of small molecules/ligand to a large molecule/ macromolecule in the solution phase. Depending upon the nature of the interaction between the two molecules, heat is either released or absorbed. As the name "Isothermal" suggests, ITC measures these changes by maintaining a constant temperature between a reference cell and the sample/reaction cell. Constant power is supplied to compensate for the temperature changes in the cell. The amount of power supplied to maintain the isothermal condition is instantaneously recorded by the instrument. The enthalpy of the reaction is calculated by integrating the power supplied over time.

The measure of heat released/absorbed upon the addition of ligand to the macromolecule sample can be expressed by the following equation[141]

$$Q = V\Delta H[M]\{\frac{K_a\,[L]}{1+K_a\,[L]}\} \quad (2.9)$$

In the above equation, V represents the volume of the reaction cell, ΔH represents the enthalpy of binding per mole of ligand, [M] is the overall concentration of the macromolecule in the reaction cell, K_a is the binding constant associated with the reaction, and [L] is the concentration of unbound ligand.

In the present work, we have used ITC to obtain the binding constants between quantum dots and small organic molecules. These ITC studies were performed in the Malvern MicroCal iTC200 calorimeter. The working principle of the instrument is described in the following paragraphs.[142]

In this ITC instrument, there are two cells: a sample cell and a reference cell. Both of these cells are identical and made out of a chemically inert material "Hastelloy". The temperature difference between these two cells is maintained at zero (an isotherm is maintained) through a constant power supply.

The reactant cell is loaded with the macromolecule sample. While the other reactant (small molecule) is loaded in the injector syringe with a syringe volume of 40 μL.

Small volumes of about ~1μL of the titrant are injected at regular intervals of time, into the sample cell. Depending upon the nature of the reaction, exothermic or endothermic, the temperature of the sample cell changes. Constant power is supplied to either of the cells to maintain this temperature difference to zero.

The measure of this power is then converted into the heat change and plotted with the mole ratio of the reactants (moles of titrant/ moles of sample cell reactant). The obtained graph is used to get thermodynamic parameters associated with the reaction such as enthalpy of the reaction, entropy, and binding constants as shown in SCHEME 2.4.

Therefore, in this manner, from the slope of the graph, we obtained the binding constant of the reactions we studied.

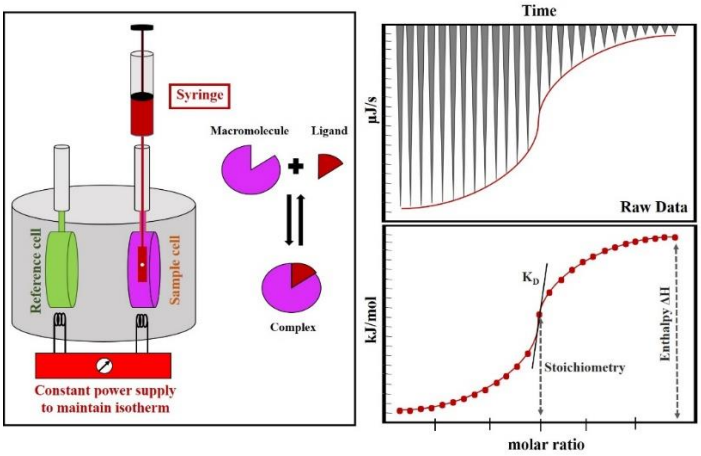

SCHEME 2.4. A schematic representation of an ITC instrument and the data collection.

2.7 Dynamic Light Scattering (DLS)

Dynamic Light Scattering (DLS) was used to measure the hydrodynamic radius of different quantum dots used in this work.

The technique works on the principle where it uses laser light to illuminate the particles under investigation, some of this light is scattered by the particles.[143] Due to the Brownian motion of the particles, the intensity of the scattered light fluctuates over time i.e. the scattering is dynamic. The detected light from the ensemble of diffusing particles provides a fluctuating intensity signal. The rate of these intensity fluctuations is dictated by the hydrodynamic size of the particle: Smaller particles diffuse quickly while the larger particles diffuse slowly. These intensity fluctuations are exploited to generate an autocorrelation function. The correlation curve decays rapidly for smaller particles and slowly for larger particles. The value of the translational diffusion coefficient is then

extracted from this autocorrelation function. The size information from the diffusion coefficient is obtained using the Stokes-Einstein equation:

$$d_H = \frac{kT}{3\pi\eta D} \tag{2.10}$$

We used Nano-ZS (Malvern) instrument to carry out the DLS experiments. The instrument has a 4MW He-Ne Laser (632nm) as the illumination source. All the samples were placed in a 1cm path length glass cuvette with transparent walls. Particular size measurement is repeated several times and these results are plotted in terms of hydrodynamic size distribution. The instrument provides size distribution in two modes (i) intensity mode and (ii) number mode.

2.8 Fluorescence Correlation Spectroscopy

To get an idea of the hydrodynamic diameter of QD (including the capping agent), another technique "Fluorescence Correlation Spectroscopy" was also performed.[144,145]

The translational diffusion constant of QD was measured using fluorescence correlation spectroscopy (FCS). FCS experiment was performed with a Zeiss LSM780 confocal microscope. Exceedingly dilute aqueous QD solution was excited using a 405 nm diode laser and rhodamine 6G (R6G) solution was excited by ~488 nm argon-ion laser. An oil immersion objective (63X, 1.4 NA) was used to excite the molecules within the confocal volume. Emission was collected using the same objective by two detectors (to avoid after pulse correlation). The autocorrelation function for a single particle diffusing through a 3-dimensional Gaussian confocal volume can be expressed as,[145]

$$G(\tau) = \frac{1-T+T\exp\left(-\frac{\tau}{\tau_{tr}}\right)}{N(1-T)}\left[1+\frac{\tau}{\tau_D}\right]^{-1}\left[1+\frac{\tau}{k^2\tau_D}\right]^{-\frac{1}{2}} \tag{2.11}$$

Where T is the fraction of the molecules in the triplet state and τ_{tr} is the triplet state lifetime. Triplet state kinetics was avoided using low laser power. τ_D is the diffusion time for the fluorescent molecule/particle and is related to the diffusion coefficient through the following equation,

$$D(t) = {\omega_{xy}}^2 \Big/ 4\tau_D \tag{2.12}$$

The transverse radius ω_{xy} (~ 290 nm) of the excitation volume was calibrated using R6G in water as a standard (D_t=426 μm^2/S). The hydrodynamic radius of the diffusing particle was obtained from the following Stokes-Einstein equation using the measured Dt value.

$$D_t = \frac{k_B T}{6\pi\eta r_h} \tag{2.13}$$

The measured QD dimension (obtained from HRTEM) and hydrodynamic diameter (obtained from FCS) were found to be nicely correlated.

2.9 HR-TEM measurements

We have used HR-TEM measurements to characterize the synthesized quantum dots as well as to obtain their core sizes. These core sizes were further utilized to obtain various information like energy band positions of the Quantum dots. These TEM measurements were performed on HR TEM JEOL, 200KV, Model No JEE-2100.

2.10 Brus Equation and the Bandgap in Quantum Dot

As described in the earlier section, when one approaches the nanoscale from bulk, the electronic states of the nanosystem change from bulk states. Prof Brus had proposed a model to quantify the change in the energies of electronic states and the band structures of nanoscale semiconductors

from bulk semiconductors.[146] The model uses bulk information, for example, effective masses of electrons and holes in the bulk semiconductor, to estimate the new band alignments in the semiconductor nanomaterial.

According to the Brus model, the band position of the valence band and conduction band in the new nanoscale semiconductor is represented by the following relations

$$E_{VB} = E_{VB}{}^{Bulk} + \frac{\hbar^2\pi^2}{2R^2 m_h^*} - \frac{1.8e^2}{4\pi\varepsilon_0\varepsilon R} \tag{2.14}$$

$$E_{CB} = E_{CB}{}^{Bulk} - \frac{\hbar^2\pi^2}{2R^2 m_e^*} + \frac{1.8e^2}{4\pi\varepsilon_0\varepsilon R} \tag{2.15}$$

Equations 2.14 and 2.15 can be utilized to get an expression of the new bandgap of the semiconductor nanomaterial.

$$E_{g*} = E_g + \frac{\hbar^2\pi^2}{2R^2}\left[\frac{1}{m_e^*} + \frac{1}{m_h^*}\right] - \frac{1.8e^2}{4\pi\varepsilon_0\varepsilon R} \tag{2.16}$$

Where, $E_{VB}{}^{Bulk}$, $E_{CB}{}^{Bulk}$, and E_g are the valance band, conduction band, and bandgap energies of bulk semiconductor material, ε is the dielectric constant of semiconductor and R is the radius of QD. m_h*and m_e* are the effective masses of hole and electron, respectively.

As can be seen in the above equations, all the expressions are dependent upon the bulk electronic properties.

2.11 Calculations of Fluorescence Quantum Yields (QY)

Fluorescence quantum yield is the ratio of the number of photons emitted by a fluorophore to the number of photons absorbed by the same. The Quantum Yield of a fluorophore signifies the efficiency of the fluorophore to fluoresce.

There are two methods by which quantum yields are generally calculated.

(i) Absolute method

(ii) Reference method

To obtain the QY of the fluorophores used in the present work we used a reference method, as the absolute method poses many difficulties.

In the reference method, we used a reference standard whose quantum yield is already known. Fluorescence from the sample is compared against this standard in terms of its steady-state fluorescence emission spectrum while the OD at excitation wavelength is the same for both, the sample and the reference standard. Here, similar absorption of light means both the solutions do not differ much in terms of their ODs at the excitation wavelength. For accurate measurements very dilute solutions of the fluorophores were used. The following relation is used and the QY of an unknown sample is calculated,[21]

$$\phi_f = \phi_f^{'} \frac{I_f A_f' \eta^2}{I_f' A_f \eta'^2} \qquad (2.17)$$

Here, Φ_f and Φ_f' are the quantum yields of the unknown and the standard sample respectively,

I_f and I_f' are the steady-state fluorescence intensities of the unknown and the standard respectively, which are measured by calculating the area under the curve of the fluorescence profile of the respective fluorophores.

Similarly, A_f and A_f' are the optical densities of the unknown and reference respectively.

η and η' are the refractive indices of the solvents in which unknown and reference are taken.

2.12 Calculation of Spectral Overlap Integral

As discussed in the previous chapter, the spectral overlap integral is the extent of overlapping between the absorption spectrum of the acceptor and the fluorescence spectrum of the donor. The mathematical expression of the overlap integral can be given by the following expression:[21]

$$J(\lambda) = \frac{\int_0^\infty F_D(\lambda)\varepsilon_A(\lambda)\lambda^4 d\lambda}{\int_0^\infty F_D(\lambda) d\lambda} \tag{2.18}$$

Where, F_D is the fluorescence intensity obtained from the area normalized (to the unity) emission spectrum of the donor (in absence of acceptor) while $F_D(\lambda)$ is the same for the wavelength range λ to $\Delta\lambda$ and $\varepsilon_A(\lambda)$ extinction coefficient of the acceptor at wavelength λ.

The unit of spectral overlap integral, $J(\lambda)$, is $M^{-1}cm^{-1}nm^4$ when $\varepsilon_A(\lambda)$ is expressed in the unit $M^{-1}cm^{-1}$ and λ is expressed in nm scale while $F_D(\lambda)$ is always dimensionless.

Förster distance (R_0) is calculated using the overlap integral as follows

$$R_0 = 0.211\left[\kappa^2\eta^{-4}Q_D J(\lambda)\right]^{1/6} \tag{2.19}$$

The Förster distance R_0 can be further used to calculate the FRET rate as follows:

$$k_T(r) = \frac{1}{\tau_D}\left(\frac{R_0}{r}\right)^6 \tag{2.20}$$

It is quite evident from equations 2.18, 2.19, and 2.20 that the rate of FRET has a linear dependence on spectral overlap integral.

2.13 Poisson Distribution

We have assumed a Poisson distribution of small quencher molecules over the quantum dot surface to study the interaction between the single quantum dot and multiple quencher molecules.

Poisson distribution is a probability distribution of a set of independent events taking place in a fixed interval of time of space with a constant mean rate. In the context of our studies, we have used Poisson distribution to obtain a probability distribution of small molecules over a single quantum dot particle. The distribution can be expressed as follows:[39]

$$\Theta(n) = \left(\frac{m^n}{n!} \right) \exp(-m) \qquad (2.21)$$

Where m and n are the average and the actual number of small molecules attached to a single quantum dot particle.

CHAPTER 3

Analysis of FRET Timescale: A Model-Free Approach

3.1 Introduction

Knowledge of photophysical processes taking place within semiconductor materials is important for developing next-generation nanomaterial-based assays with enormous possibilities in various applications.[147–161] Among all photophysical processes studied in quantum dots (QDs), photoinduced electron transfer (PET) and Förster resonance energy transfer (FRET) have attracted intense interest from researchers. [40,117,147–163] Recent developments of various FRET assays demonstrate tremendous applications of FRET mostly in biology, for example, as a spectroscopic ruler, in the development of biosensors, in vitro pH sensing, multiphoton cell imaging, determination of metabolic rates, and studying lipid rafts in cell membranes.[164–168] In materials chemistry, FRET is mostly used in QD-based nanosensors. Applications of these sensors include enzyme activity detection; pH sensing; detection of pollutants in the environment; and detection of biological entities, such as microorganisms and viruses.[169–173] In the study of the photophysical processes of QDs in a model system, many recent reports have preferred transient absorption spectroscopy over fluorescence spectroscopy for various reasons.[78] For instance, Lian et al. studied exciton dissociation in CdS QDs through electron transfer to the ground state of rhodamine B (RhB) dye by using transient absorption spectra of RhB.[78] The emergence of an absorbing species at $\lambda \approx$ 425 nm (owing to RhB^- formation), at the cost of ground-state bleaching of RhB at $\lambda \approx$ 545 nm, is a clear indication of the reduction of RhB. The significant separation of spectral signatures of this reaction pair removes the possibility of any FRET from QD* to RhB, as further confirmed

by the lack of stimulated emission from RhB (at $\lambda \approx 600$ nm).[78] Unlike fluorescence spectroscopy, individual bands in a transient absorption spectrum represent the fingerprints of transient species generated through different photophysical processes. In this way, transient absorption spectroscopy not only recognizes the nature of photophysical processes (i.e., FRET or PET) taking place within a system, also the timescale associated with these processes can be detected by studying the time evolution of transient absorption bands. On the other hand, fluorescence spectroscopy provides only information about the S_1-to-S_0 transition, and the fluorescence from S_1 can be affected by several phenomena; no unique bands characteristic of individual photophysical phenomena can be found in most cases. Despite this shortcoming, fluorescence spectroscopy has found tremendous application in biology, not just because of its simple instrumental measurement techniques, but because fluorescence spectra are much easier to elucidate, compared to the transient absorption spectra. The transient absorption spectrum is often tainted with absorptions from multiple absorbing species present within the medium, and therefore, one must have prior knowledge of the spectral signature of the absorbing molecule of interest. In this regard, fluorescence spectra have more integrity because all molecules can absorb, but very few of them can emit. Recently, many groups have used fluorescence spectroscopic techniques to study FRET in various nanoassemblies and their works suggest that careful analysis is highly warranted for obtaining pure FRET components. For instance, Zamkov et al. demonstrated the importance of spectral cross-talk analysis in the multifluorophore assembly for the determination of FRET efficiencies.[153] Successful FRET analysis requires a suitable fitting model or theoretical approach based on some meaningful approximations. In this context, a remarkable work by Patra et al. on FRET between CdS QDs (and quantum rod) and Nile Red is worth mentioning here.[39] They proposed that the binding of an acceptor (Nile Red) to a donor (CdS) would follow a Poisson

distribution. Good fitting of experimental data with the Poisson-based fitting analysis proposed by Patra et al. demonstrates that the interaction between the donor and acceptor in a bimolecular FRET process is not straightforward. Bearing in mind the inherent difficulties of transient absorption techniques, especially in biology, herein we establish a relatively model-free approach for the accurate determination of the energy-transfer timescale, and thereby, the donor-to-acceptor distance in a QD-based FRET assay by utilizing the bright and stable fluorescence of CdSe/ZnS QDs.[174] The accurate determination of the donor-to-acceptor distance justifies the acceptability of our approach. Our proposed method allows the accurate detection of FRET components, even when the emission band positions of donor and acceptor are very close. Herein, we used extensive spectral fittings to split the fluorescence from the two closely emitting species (donor and acceptor). We also fitted our data in a separate analysis by using the method reported by Patra et al., which showed that a large fraction of acceptor remained unbound, even at the highest acceptor/donor (≈2) molar ratio.

3.2 Our Model System

We used a water-soluble CdSe/ZnS core-shell QD which was purchased from Invitrogen-Thermo Fisher Scientific. The QDs were surfaced passivated by a negatively charged polymer layer with $–COO^-$ surface groups [SCHEME 3.1(a)]. Along with the negatively charged water-soluble QD we used a positively charged organic dye molecule, Rhodamine-6G (R6G) [SCHEME 3.1(b)]. All the solutions were performed in aqueous solutions using MilliQ water (Merck Millipore).

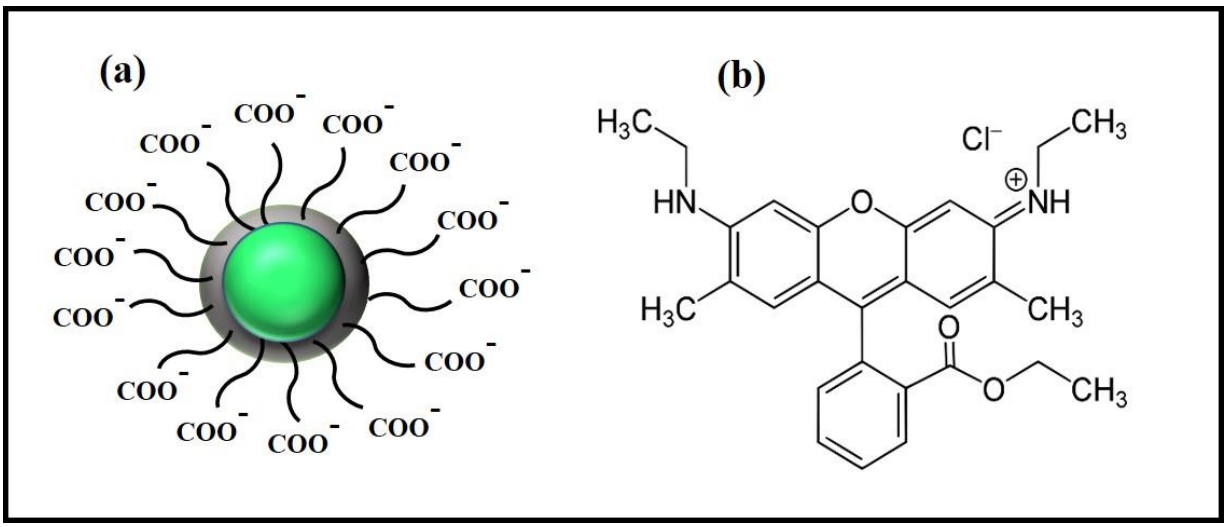

SCHEME 3.1. (a) Negatively charged CdSe/ZnS core-shell QD (b) positively charged R6G molecule.[174]

3.3 Interaction between QD and R6G: Rotational Anisotropy Decay Study

Due to the oppositely charged nature of QD and R6G, we had suspected an electrostatic attraction between the two. To confirm the complex formation, we performed a rotational anisotropy decay study. A much slower rotational anisotropy decay time (≈5 ns) of R6G in presence of QD was observed [Figure 3.1 (a)]. However, in the absence of QDs, R6G in water exhibited a fast single-component rotational decay time (≈230 ps) [Figure 3.1 (b)]. The initial anisotropy value (i.e., anisotropy at time zero (r_0)) of R6G, which is not affected by rotational diffusion of the R6G dipole, exhibited an exceedingly low value (r0 ≈0.015) when R6G was indirectly excited through FRET (by exciting the attached QD at λ_{ex}=375 nm; [Figure 3.1(a)]. However, when R6G was excited directly in the absence of QDs, the initial anisotropy value of R6G reached about 0.3, which is very close to the theoretical value of about 0.4 [Figure 3.1(b)]. The drop in the r_0 value of R6G is due to the indirect excitation of R6G by QD* through the FRET mechanism (Figure

3.1).[21] This was within our intuitive expectations as transition moments of the donor (QD) and acceptor (R6G) are expected to be randomly oriented within the QD–R6G complex.

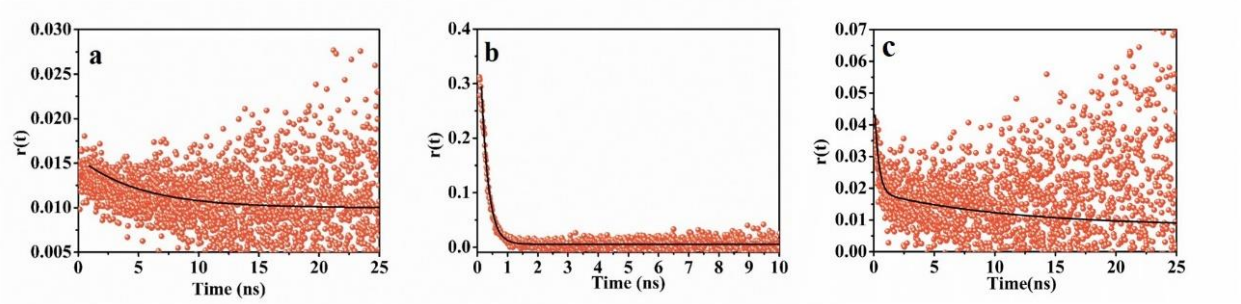

Figure 3.1. (a) The decay of rotational correlation function (r(t)) of R6G in water in the presence of QD (≈400 nM QD mixed with ≈400 nM R6G). The sample was excited at λ≈375 nm, at which QD exclusively absorbs, and the emission was collected at λ≈600 nm, at which R6G exclusively emits. (b) The decay of the rotational correlation function (r(t)) of R6G alone in the water. The sample was excited at λ≈445 nm and emission was monitored at λ≈600 nm. (c) The decay of rotational correlation function (r(t)) of R6G in water in presence of QD when the sample was excited at λ≈ 445 nm where both QD and R6G absorb.[174]

3.4 FRET Induced Quenching of QD Fluorescence

Lifetime and steady-state emission of QD in water was significantly suppressed in the presence of R6G as can be seen in Figure 3.2.

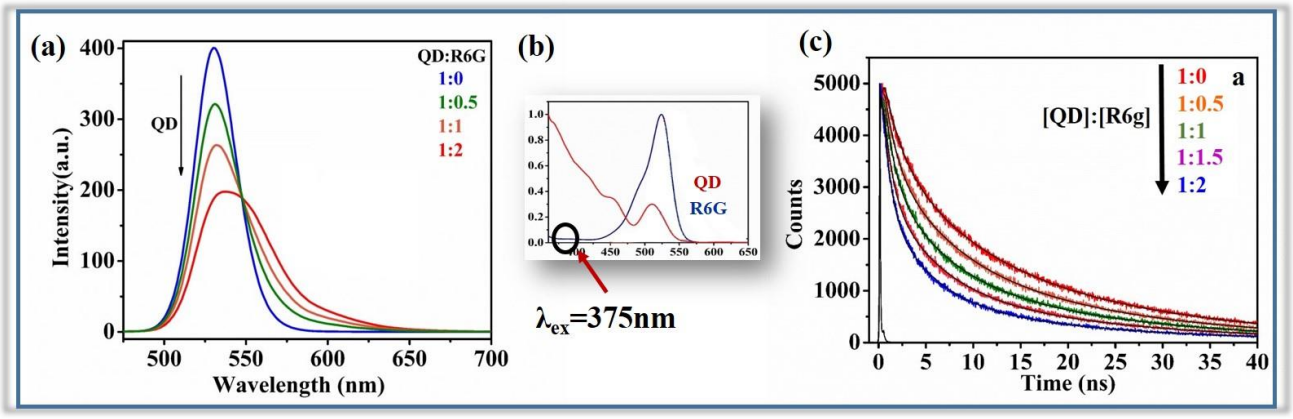

Figure 3.2. (a) Steady-state fluorescence quenching of QD on step by step addition of R6G to QD (water solution) (b) Absorption spectra of QD (red) and R6G (blue) showing huge absorption of QD at $\lambda_{ex} \approx$ 375nm while negligible absorption of R6G. (c) Quenching in the fluorescence lifetime of QD (water solution) on step by step addition of R6G. [174]

Three probable mechanisms could have caused the quenching of QD emission: (i) hole transfer from valance band (VB) of photo-excited QD (QD*) to the HOMO of R6G, (ii) electron transfer from conduction band (CB) of QD* to the LUMO of R6G and (iii) FRET from QD* to R6G through a non-radiative mechanism. Number (i) and (ii) are thermodynamically forbidden [Figure 3.3(a)].

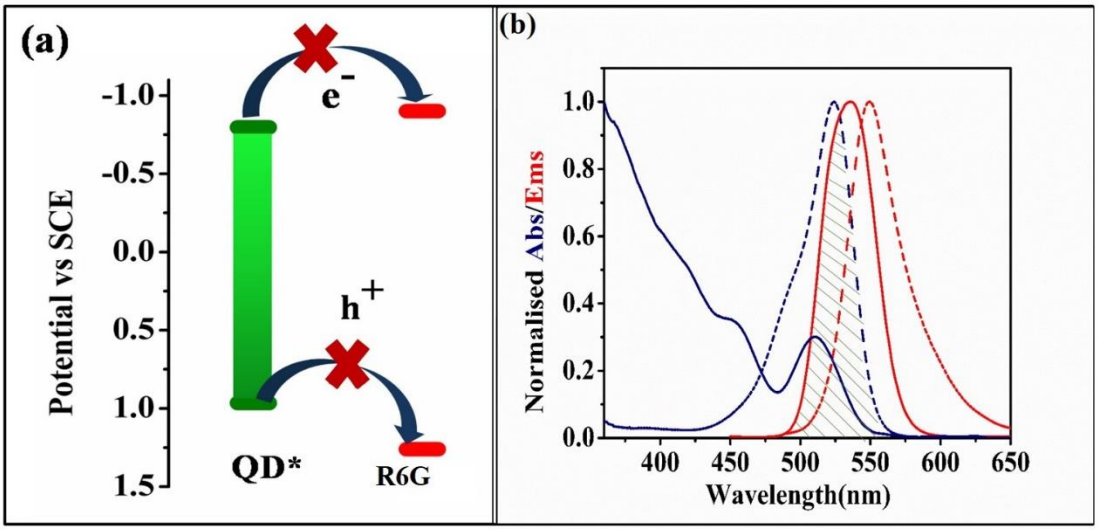

Figure 3.3. (a) Energy band alignment diagram of CdSe/ZnS QD-R6G couple. (b) Individual spectral profiles of QD and R6G where blue and red solid lines are the absorption and emission spectra of QD, while blue and red dotted lines are the same for R6G. The shaded region represents the spectral overlapping between QD's emission and R6G's absorption. [174]

R6G exhibits an oxidation potential of +1.26 V and reduction potentials of -0.9 V (vs SCE), respectively [Figure 3.3(a)].[175a] Energy of the lowest exciton state [$1S_{3/2}$(h)-1S(e)] of the QD* was calculated using Brus's assumption (i.e., QD as spherical well having an infinite potential barrier) and using equation 2.16 described in chapter 2 of the present thesis.[140]

In this bandgap equation, R is the radius of the QD core (~2.25 nm as obtained from high-resolution TEM measurement; Figure 3.4). Eg (~ 1.7 V) is the energy gap in bulk CdSe material. m_h*(=0.8 m_0) and m_e* (=0.2 m_0) are the effective masses of holes and electrons, respectively.[175b]

Following Brus's recipe (using ε=5.8 and rest mass of a free electron m_0= 9.1×10^{-31} kg), we obtained reduction and oxidation potentials of our excited QD, which were found to be ~ 0.965 V (SCE) and -0.796 V (SCE), respectively.

Therefore neither an excited state electron nor hole can be transferred from QD* to R6G [Figure 3.3(a)].

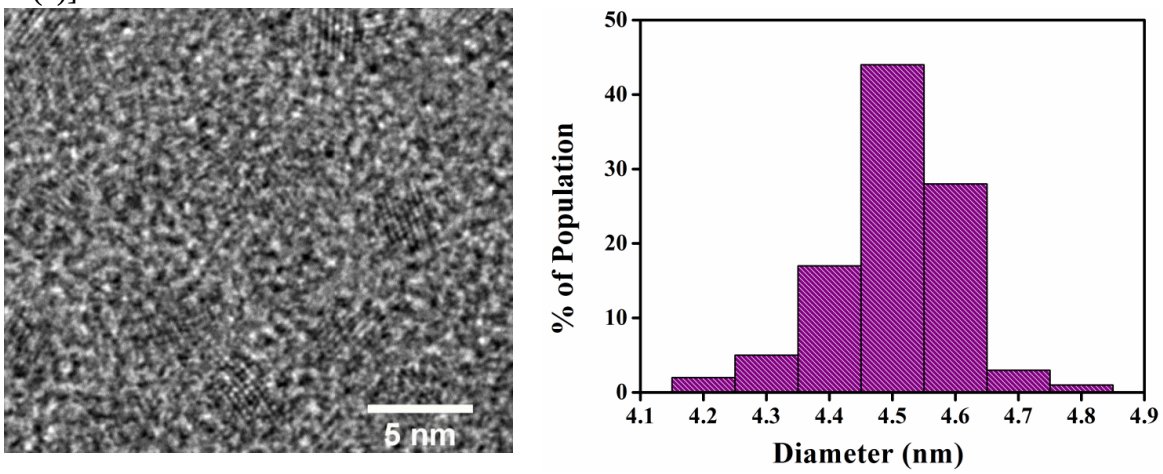

Figure 3.4. The left panel of the figure represents the high-resolution TEM image of CdSe/ZnS core-shell QD while the right panel of the figure represents the size distribution histogram for QD particles. The mean particle size from the histogram is ~4.5 nm (excluding the capping agent). [174]

Therefore, FRET would be the only possible mechanism here leading to the quenching of QD fluorescence in the presence of R6G (Figure 3.2). Figure 3.3(b) shows a nice overlapping between the spectral signatures of the donor and acceptor molecules, which is a prerequisite for obtaining an efficient FRET rate.

3.4.1 Steady-State Quenching Experiment

In Figure 3.5, we excited the QD-R6G complex at ~375 nm to excite the QD selectively [Figure 3.2(b)], and emission from R6G can be obtained only after FRET. Figure 3.5 shows an isoemissive

point. The total steady-state emission intensity of the sample at the iso-emissive point remained the same, irrespective of the amount of R6G added against a fixed concentration of QDs.

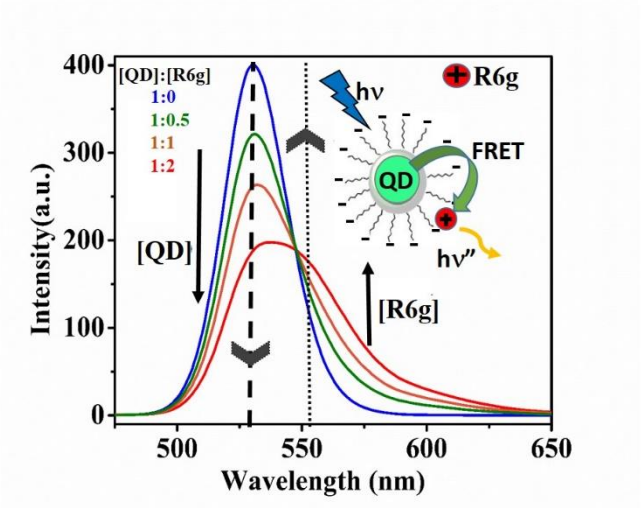

Figure 3.5. Steady-state emission spectra of QD-R6G FRET couple at various QD-to-R6G molar ratios. All the samples were excited at ~ 375 nm (where only QD absorbs [Figure 3.2(b)]). The concentration of QD was ~20 nM in all the samples. Dashed and dotted vertical lines represent the emission peak positions of QD (~531 nm) and R6G (~551 nm) respectively. The resultant emission peak positions of the complex are ~531 nm, ~531 nm, ~532 nm, and ~538 nm at QD-to-R6G mole ratios 1:0, 1:0.5, 1:1, and 1:2, respectively. [174]

The emergence of an iso-emissive point for the FRET pair indicates that the decrease in the fluorescence intensity of the donor is the same as the increase in fluorescence intensity of the acceptor. The appearance of an isoemissive point in a steady state is a sign of the presence of two emissive species coupled via a resonance energy transfer process. We only studied R6G-to-QD

molar ratios up to about two (i.e., up to the value at which the isoemissive point is retained); at higher molar ratios (>4) the isoemissive point was found to be disturbed significantly as can be seen from Figure 3.6.

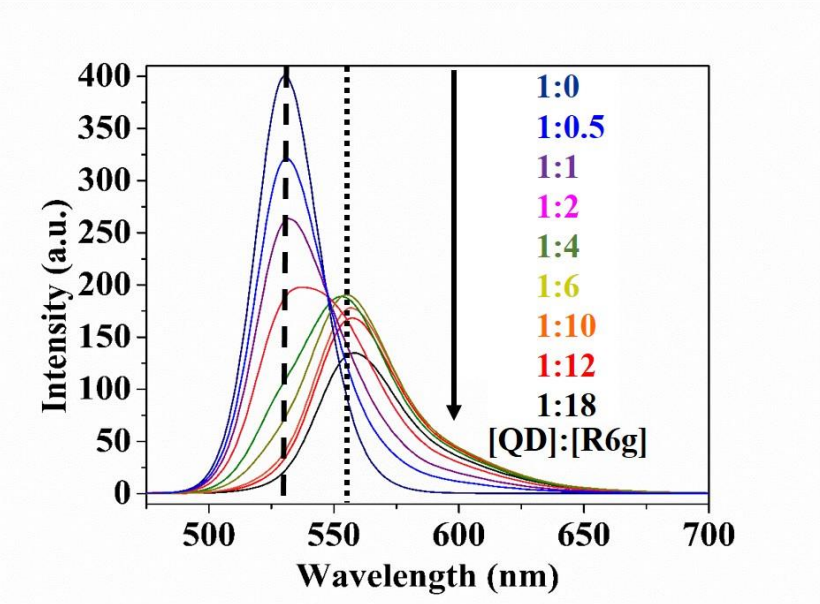

Figure 3.6. Steady emission spectra of QD-R6G complex in the water at different QD-to-R6G molar ratios at λ_{ex}~ 375 nm (at which, only QD absorbs). The concentration of QD was kept constant in all the samples (~20 nM). Dashed and dotted vertical lines represent the steady-state emission peak positions of QD and R6G respectively. The isoemissive point disappeared after the molar ratio of 1:4 (QD to R6G). At the high molar ratio samples (>4) the emission intensities of both the emitting species (QD and R6G) were found to decrease, which may be due to the onset of PET. This is in contrast to the low molar ratio samples, at which the intensity of QD fluorescence decreases at the cost of a concomitant increase in the R6G emission. [174]

3.4.2 Spectral Overlap Integral and FRET Efficiency

Figure 3.3(b) shows a significant spectral overlap between the donor emission with acceptor absorption, which yields a high value (~4.51×10^{15} $M^{-1}cm^{-1}nm^4$) of overlap integral parameter J(λ). A long Förster distance, as calculated from J(λ) for our FRET couple, enabled an efficient FRET, even at a long donor-to-acceptor separation (Figure 3.7). FRET efficiencies were calculated from both steady-state quenching data and lifetime quenching data and shown in Figure 3.7.

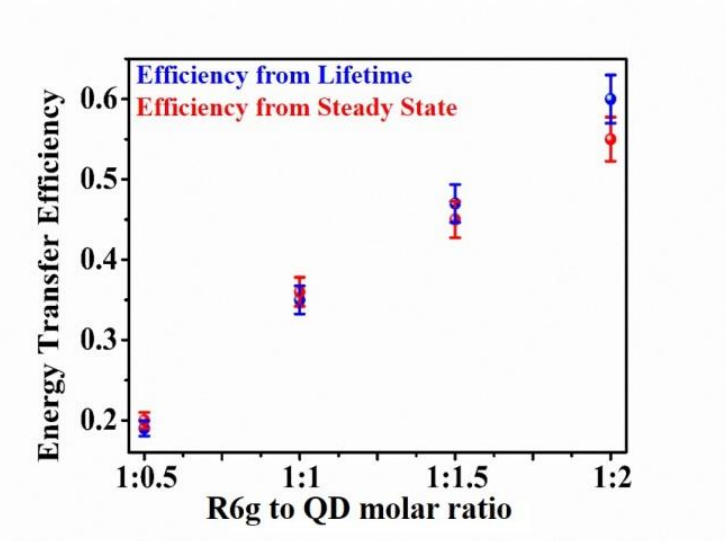

Figure 3.7. FRET efficiencies (E) for QD-R6G complex at different R6G-to-QD mole ratios. Blue balls representing the efficiencies calculated from lifetime quenching of QD, whereas red balls representing the same, calculated from the quenching of steady-state emission of QD. Emission peak positions of QD and R6G are quite close; the individual emission spectrum of donor and acceptor was obtained by splitting the overall emission spectrum of QD-R6G complex using a bi-lognormal fitting function [Equation (3.2)]. During the bi-lognormal fitting, we kept peak positions of QD and R6G fixed to their actual values in the pure spectrum (spectrum of only QD or R6G). The steady-state intensity was calculated from the area under the split emission spectrum. [174]

3.4.3 Lifetime studies of QD and R6G

The fluorescence lifetime profile of R6G (attached to QDs), which was obtained by exciting the QDs ($\lambda_{ex} \approx$ 375 nm, as R6G has negligible absorption at this wavelength), exhibited a rise component at the initial time which preceded the decay during the latter time [Figure 3.8 (b)]. However, this initial rise feature disappears if R6G is excited directly (in the absence of QD; pink curve: Figure 3.8(b)).

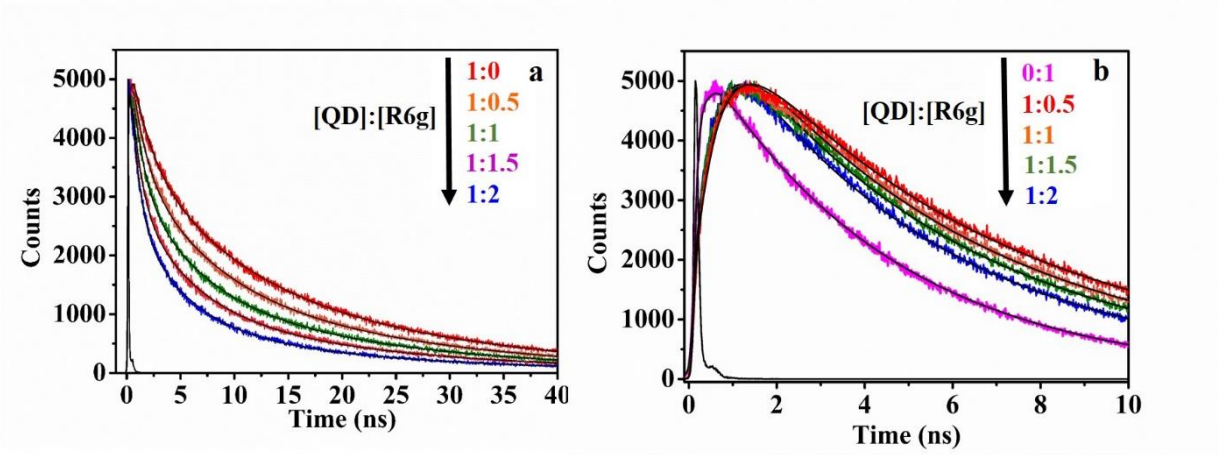

Figure 3.8. Excited-state lifetime decay curves of (a) QD (≈ 20 nM) emission collected at $\lambda_{em} \approx$ 510 nm and (b) R6G emission collected at $\lambda_{em} \approx$ 590 nm at various QD to R6G molar ratios. All the samples were excited at $\lambda_{ex} \approx$ 375 nm, at which QD exclusively absorbs. For fitted components, refer to Table 3.1. [174]

In addition to that, a continuous quenching in the lifetime of QD fluorescence was observed upon a step-by-step addition of R6G [Figure 3.8 (a)]. The rise in acceptor's lifetime [Figure 3.8 (b)] and a concomitant quenching of donor's lifetime [Figure 3.8(a)] is a clear signature of FRET taking place within the QD-R6G complex. As both steady-state and lifetime data had confirmed the FRET

phenomenon, further analysis of FRET was carried out and the accurate FRET components were determined using a model-free analysis of time-resolved area normalized emission spectra (TRANES), a detailed description of which is provided in the remaining part of this chapter. This approach enabled a comprehensive analysis even when the emission peak positions of the donor and acceptor are very close.

Table 3.1. Lifetime fitting components of QD-R6G complex at different QD-to-R6G molar ratios (Figure 3.8). [174]

	QD:R6G ratio	**$\tau_1(a_1)$** **ns**	**τ_2 (a_2)** **ns**	**τ_3 (a_3)** **ns**
QD	**1:0**	1.65 (27%)	7.89 (34%)	22.13 (39%)
	1:0.5	1.19 (33%)	6.65 (36%)	21.55 (31%)
	1:1	1.01 (40%)	5.92 (36%)	21.36 (24%)
	1:2	0.69 (53%)	4.61 (34%)	20.18 (13%)
R6G	**0:1**	2.5 (9%)	4.39 (91%)	_____
	1:0.5	0.52 (-224%)	5.9 (294%)	19.6 (30%)
	1:1	0.50 (-209%)	5.45 (280%)	16.47 (29%)
	1:2	0.4 (-197%)	4.83 (277%)	14.2 (20%)

3.5 TRANES Analysis of the FRET Pair

TRANES were obtained by area normalizing the time-resolved emission spectra (TRES). Any excited state kinetics that leads to an energy stabilization or energy migration from one state to another is manifested by the spectral changes in TRES. Timescales associated with the kinetics were obtained from TRES analysis. Construction of TRES was performed following a recipe provided by Graham Fleming, Mark Maroncelli, and their colleagues; more details of which can be found in several existing reports and also in the previous chapter [Chapter 2].[13,140,176,177] TRES (without area normalization) were not very useful for FRET analysis, as the intensity of TRES gradually decreases with time due to the natural excited state decay process, and this phenomenon can mix easily with other processes of interest, which also cause the intensity changes (for example FRET, PET, etc). Upon area normalizing the TRES (by constructing TRANES), one can virtually stop the natural excited state decay process and thereby separate the excited state decay kinetics from the actual process of interest. After normalizing the TRES (by constructing TRANES), the total excited state population of the QD-R6G complex would not change with time, although the individual population may change due to FRET. In this scenario, TRANES would provide visual observation of excited state population (or emission intensity) shifting due to FRET from QD* side to R6G side over time.[77] Figure 3.9 shows the TRANES of QD-R6G FRET couple at a molar ratio of 1:2 when excited at $\lambda_{ex} \approx 375$ nm. At $\lambda_{ex} \approx 375$ nm, only the QDs are excited, leaving R6G unexcited due to its very low extinction coefficient value at 375 nm [Figure 3.2 (b)].

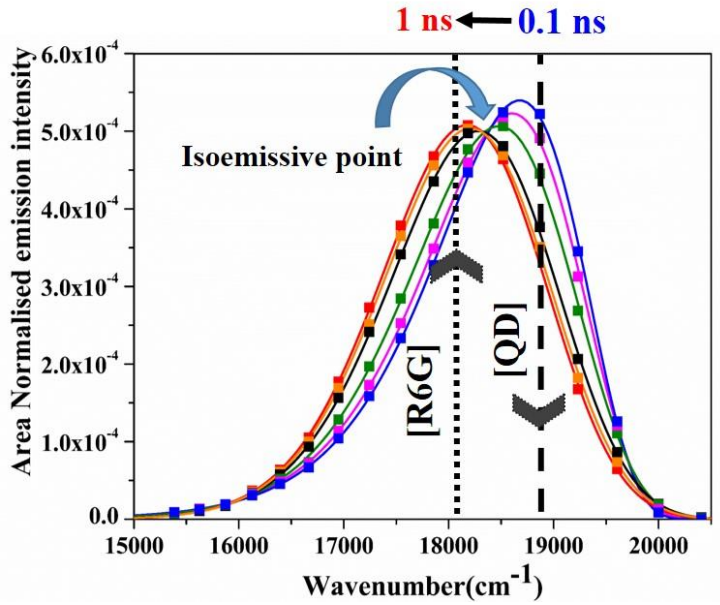

Figure 3.9. TRANES of QD-R6G FRET couple (for the QD to R6G molar ratio ~1:2 at λ_{ex}≈375 nm): FRET causing the excited-state population transfer from QD* to R6G in the time window of 0.1 ns to1 ns. Steady-state emission peak positions of QD and R6G are indicated by the vertical dashed and dotted lines respectively. [174]

Emission peak positions of QD and R6G in water are λ≈531 nm (or 18,832 cm^{-1}) and 551 nm (or 18,149 cm^{-1}), respectively, separated by only about 20 nm. We observed TRANES from ~100 ps to ~25 ns time window covering more than two decades in times. The one end of the time window (100ps) was limited by the IRF of our instrument (~70 ps), while the other end was terminated at ~25 ns as the lifetime of QD was ~16 ns (R6G has a much shorter lifetime ~4 ns). In TRANES analysis we observed an opposite phenomenon after 2 ns, compared to what we observed before 2 ns. Therefore, to obtain a better understanding we split the total time-window (100 ps to 25 ns) of the TRANES study into two time-windows; one from 100 ps to 1 ns [Figure 3.9] and the other is from 3 ns to 25 ns which is discussed in the next chapter. The initial time window (100 ps-1 ns) showed a visual observation of fast (≈0.3 ns- 0.6 ns) excited state population migration from QD*

(peaked at 18,832 cm^{-1}) to R6G (peaked at 18,149 cm^{-1}) over time due to FRET. The emergence of an isoemissive point in TRANES indicates the presence of an equilibrium between two emissive states [Figure 3.9].[178] During the later times (3ns-25ns), we observed a slow (~ 8 ns) virtual recovery of the QD* population from the R6G* population [Chapter 4].

The time scale of excited state population migration was calculated from the knowledge of how fast the area under the TRANES curve shifts from the QD* side to the R6G* side (due to FRET). To quantify this, we first fitted the individual TRANES of QD-R6G FRET couple by using a bi-lognormal function, keeping peak positions and full-width at half-maximum of QD and R6G fixed from their individual TRANES (when QD and R6G were present alone in water). Best fitted parameters were used for constructing two split single log-normal spectra: one for QD and the other for the R6G (Figure 3.10). Similarly, we split TRANES at different times covering a range from 100 ps to 25 ns. The subsequent sections discuss the bi-lognormal fitting and spectral splitting.

3.5.1 Spectral splitting Using Bi-lognormal Fitting Function

As discussed in the earlier section, we fitted each point of QD-R6G TRANES using the following bi-lognormal equation [Equation (3.2)] and the best-fitted parameters were used for simulating the split spectra of QD and R6G (Figure 3.10 and 3.11). These split spectra of QD and R6G were not area normalized unlike the TRANES of the QD-R6G couple instead the area under the curve keeps on changing over time. This time-dependent intensity change of the split spectra was used to deduce the FRET timescale which is described in the subsequent pages.

Bi-lognormal fitting equation:

$$y(x) = \sum_{i=1}^{2} \frac{b_i}{x - a_i} \exp(-c_i^2) \exp[-\frac{1}{2c_i^2}\{\ln(\frac{x - a_i}{b_i})\}^2] \qquad (3.2)$$

Where $a_i = x_i^0 - H_i\left(\frac{\rho_i}{\rho_i^2 - 1}\right); b_i = H_i\left(\frac{\rho_i}{\rho_i^2 - 1}\right)\exp(c_i)^2; c_i = \frac{\ln(\rho_i)}{\sqrt{2\ln 2}}$

In the above equations, x_i^0, H_i & ρ_i are the emission peak position, FWHM (full width at half maximum) and asymmetric factor of the spectrum of i^{th} emitting species.

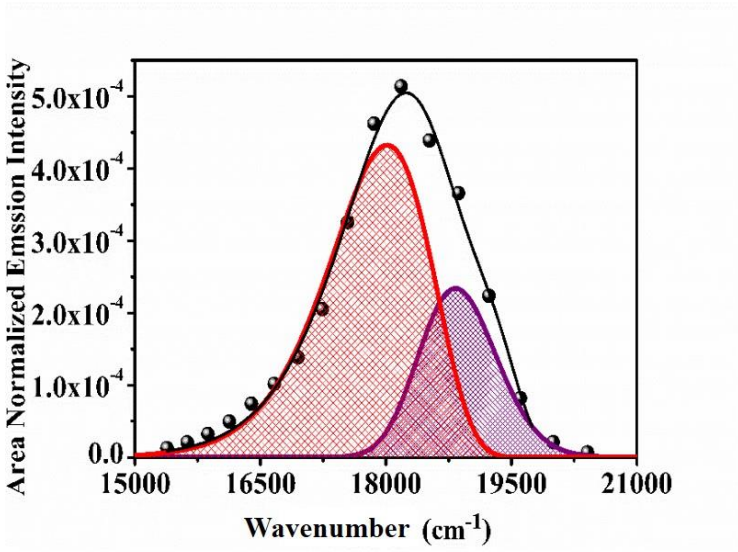

Figure 3.10. Spectral splitting of TRANES at a particular time (~500 ps) using a bi-lognormal fitting function (Equation 3.2). The black curve representing the bi-lognormal fitting to the experimental TRANES points (black balls) of QD and R6G mixture (1:2 mole ratio). Violet and Red sold lines representing the split spectra for QD and R6G, respectively. The area under the split red curve (or blue curve) is proportional to the excited state population of R6G (or QD) at time ~500 ps. [174]

3.6 FRET Timescale: Generation of Correlation Curve

After splitting each QD-R6G TRANES (Figure 3.11) we observed that as time progressed intensity of QD* subsided while the intensity of R6G* increased during the initial time window [Figure 3.11(a-b)]. Figure 3.11 shows the time-resolved emission spectra for the QD to R6G for the molar ratio 1:2. Similarly, we performed the same splitting for the other molar ratios as well (1:1 and 1:4).

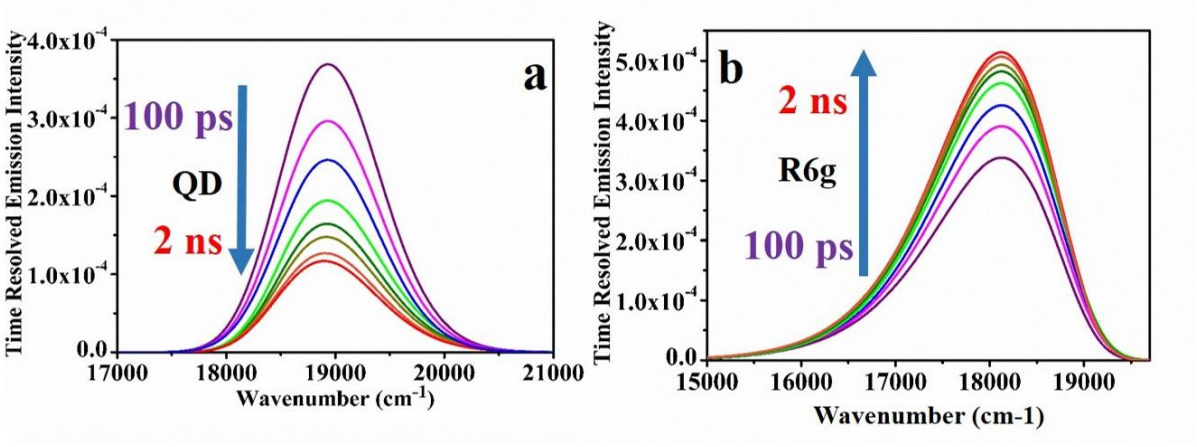

Figure 3.11. Representation of individual split time-resolved emission spectra of QD and R6G obtained from the splitting of corresponding TRANES of QD-R6G complex (with QD to R6G molar ratio 1:2). (a) the emission intensity (excited state population) of QD over time. (b) the emission intensity (excited state population) of R6G over time. [17]

The area under the split curve is proportional to the excited state population or fluorescence intensity. A correlation function, $C(t)_{FRET}$[= {ρ(t)-ρ(∞)}/{ρ(0)-ρ(∞)}] describing the FRET rate, was constructed for QD-R6G FRET couple. $C(t)_{FRET}$ is a function of relative excited state populations (i.e, area under the split curve in Figure 3.11) of donor or acceptor at time t [ρ(t)], initial time [ρ(0)] and after a long time [ρ(∞)] when excited state population migration process has completed. We used exponential fitting functions to fit the C(t)s of QD-R6G FRET couple (all the three molar ratios). During the time window ≈100 ps to 2 ns, FRET causes the quick excited state population transfer from QD* to R6G within the QD-R6G FRET couple (Figure 3.12). The FRET correlation functions [$C(t)_{FRET}$] are shown in Figure 3.12.

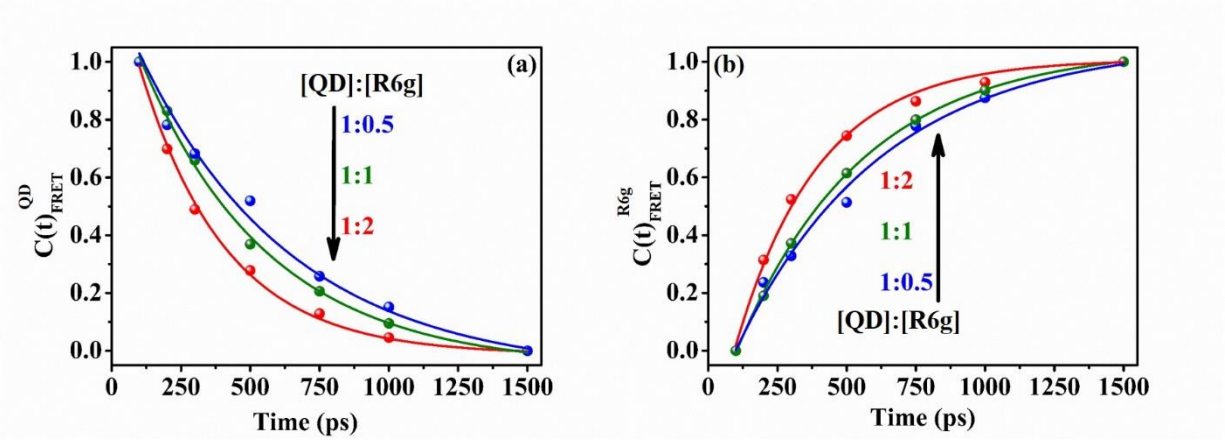

Figure 3.12. Time evolution of the FRET correlation functions [$C(t)_{FRET}$] showing excited state population decay rate of QD* (a) and corresponding population growth rate of R6G (b) at various QD-to-R6G mole ratios. These experimental [$C(t)]_{FRET}$ curves (colored balls) are fitted by exponential decay and growth functions (solid lines). All the correlation functions [$C(t)]_{FRET}$ are normalized to obtain a visual correlation between the excited state population depletion rate of QD* and excited state population growth rate of R6G; both are practically the same here. [174]

The depletion rate of the excited state population of QD* was to found be nicely correlating to the rate at which the excited state population of R6G was increasing for all the QD-to-R6G molar ratios (Figure 3.12).

3.7 Calculation of Donor-Acceptor Distances

From the obtained FRET timescale, we also calculated the QD-to-R6G distances using the following equation [Equation (3.3)] and assuming $k_{FRET}= 1/\tau_{FRET,}$ we found are ~3.8 nm, ~3.7 nm, and ~3.4 nm, respectively for QD-to-R6G mole ratios ~1:0.5, 1:1 and 1:2. The description of the individual parameters is given in chapter 2.

$$k_{FRET} = \frac{1}{\tau_{QD}^{0}} \left(\frac{R_0}{R_{DA}} \right)^6 \qquad (3.3)$$

3.8 Fluorescence Correlation Spectroscopy (FCS) Study

We also performed a fluorescence correlation spectroscopy (FCS) study of QD diffusion in water to obtain the hydrodynamic radius of QD and thereby calculated the expected donor-to-acceptor distance in the QD-R6G complex (Figure 3.13). From the measured value of the translational diffusion coefficient (D_t) and using the Stokes-Einstein equation ($D_t=k_BT/6\pi\eta\mathbf{r}$) we obtained the hydrodynamic radius of QD ~6 nm.[179,180] Radius of the R6G molecule is reported to be ~0.7 nm.[181] Therefore distance from the donor center to the acceptor center in QD-R6G complex was expected to be ~6.7 nm (~6 nm + 0.7 nm), which was underestimated by our calculated values (~3.4 nm-3.8 nm). TEM measurement (Figure 3.4) revealed the diameter of QD to be ~4.5nm without the surface polymer layer. Therefore if R6G is embedded deep inside the polymer layer of QD, the distance would be ~(4.5/2) + 0.7 =2.95 nm. Our calculated values and τ_{FRET} revealed the donor-to-acceptor distances to be ~3.4-3.8 nm, a little higher than ~2.95 nm but much lesser than ~6 nm. Therefore

the location of R6G is not at the QD-water interface; rather R6G resides deep inside the polymer layer of QD.

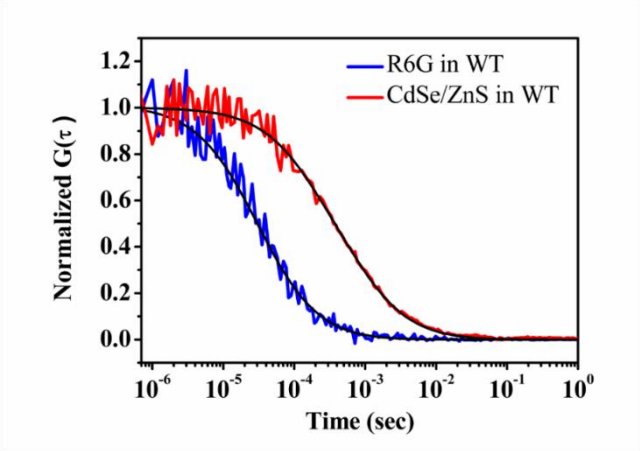

Figure 3.13. Normalized autocorrelation curve for CdSe/ZnS QD (red) and R6G (blue) in water (WT). The black curves represent the best fittings. The confocal volume was calibrated by using the known diffusion coefficient of R6G in water (426μm^2/sec).[162] Using the Stoke-Einstein theory the size of the QD was estimated to be ~12 nm. [174]

Molecular distance calculations relying on our TRANES based analysis complement nicely with the expected QD-to-R6G distance obtained from TEM and FCS measurements. This fact justifies the good acceptability of our FRET analysis method even when lifetimes of donor and acceptor molecules are predominated by unquenched molecules.

3.9 The Fraction of R6G bound per QD: The Poisson Distribution

The lifetime profile of QD (in the absence of R6G) can be described using the following equation.[39]

$$I(t,0) = I_0 \exp\left\{-k_0 t - m_t[1-\exp(-k_{qt}t]\right\} \qquad (3.4)$$

Where k_0 is the rate constant due to the unimolecular natural decay of the excited state QD in absence of R6G. k_{qt} is the quenching rate constant of the exciton by one defect site. Defect sites, which are present inherently at QD surface following a Poisson distribution, act as efficient quenchers. m_t is the average number of inherent quencher sites per QD. In the presence of R6G, if m is the mean number of R6G attached to a single QD following a Poisson distribution, the lifetime profile of QD can be described by the following equation.[39]

$$I(t,m) = I_0 \exp\left\{-k_0 t - m_t^{/}[1-\exp(-k_{qt}t)] - m[1-\exp(-k_{FRET}t)]\right\} \quad (3.5)$$

Where k_{FRET} is the FRET rate constant per R6G molecule. The natural excited state decay process of QD can be decoupled from other quenching processes (i.e., FRET, exciton trapping at quencher cites, etc) in the presence of R6G, by constructing a survival probability function [$S_q(t)$]. $S_q(t)$ is nothing but the lifetime profile of QD in the presence of R6G, normalized by the lifetime profile of QD in the absence of R6G (equation 3.5/equation 3.4).[132,182]

$$S_q(t,m) = \exp\left\{-(m_t^{/} - m_t)[1-\exp(-k_{qt}t)] - m[1-\exp(-k_{FRET}t)]\right\} \quad (3.6)$$

We used the above equation to fit the experimental survival probability curves obtained from the ratios of donor lifetime profiles (Figure 3.14; Table 3.2).

Fraction (*f*) of R6G bound to QD was calculated using the following equation.[39]

$$f = m[QD]/[R6G] \quad (3.7)$$

Where [R6G] and [QD] are the total concentration of R6G (bound + free) and QD within the solution; both were known experimentally. The value of *m* (number of R6G attached to a single

QD) was obtained from the fitting of the experimental survival probability curve using equation 3.6 (Table 3.2). The fraction of R6G bound to QD was found to be ~0.20, ~0.34, and ~0.45, respectively at molar ratios (QD-to-R6G) ~1:0.5, ~1:1, and ~1:2 (Table 3.2).

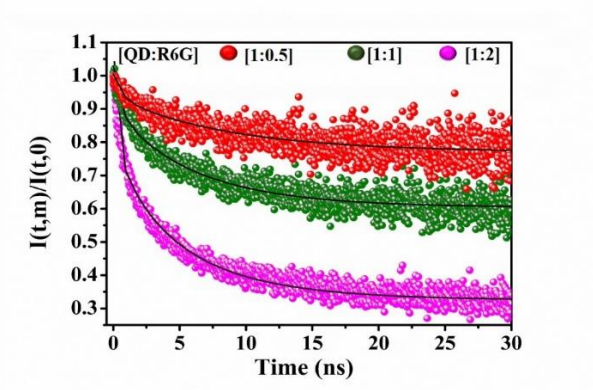

Figure 3.14. Experimental survival probability functions of QD-R6G FRET couple at different QD-to-R6G ratios. Solid lines are representing the best-fitted curves using equation 3.6. [174]

Table 3.2. The Best fitted parameters obtained after the fittings of our experimental survival probability curves with Equation 3.6 (Figure 3.14).[174]

QD-to-R6G mole ratio	**k_{qt} in ns^{-1} (quenching const due to defect sites)**	**k_{FRET} (in ns^{-1}) using Tachiya-Patra model**	**Number of R6G bound per QD**	**The fraction of R6G bound**
1:0.5	0.11	0.4	0.10	0.2
1:1	0.07	0.56	0.34	0.34
1:2	0.06	0.70	0.90	0.45

3.10 FRET Analysis at Different Temperature

To check the sensitivity of our analysis we studied FRET for the same QD-R6G (at 1:1 ratio) at two other temperatures (10 ^{0}C and 45 ^{0}C) as well. QD emission shows a slight bathochromic shift with increasing the temperature which causes lesser spectral overlap between the donor's emission with acceptor's absorption at a higher temperature (Table 3.3, Figure 3.15).

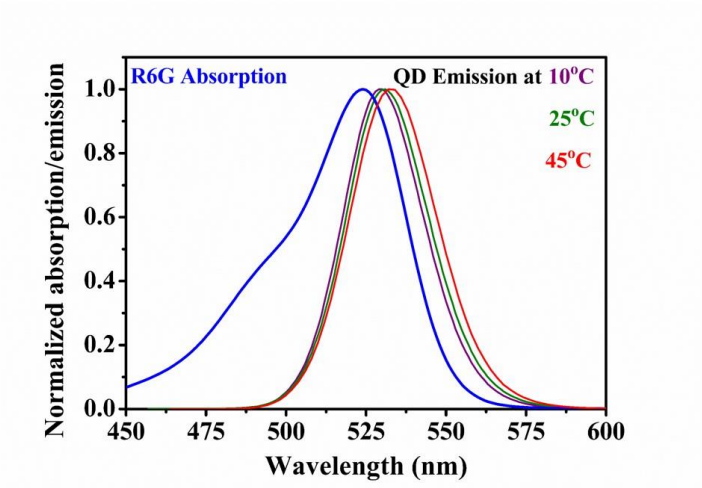

Figure 3.15. Spectral signatures of QD and R6G: the blue curve is the absorption spectrum of R6G, while violet, green and red curves are the emission spectra of QD at 10 ^{0}C, 25 ^{0}C, and 45 ^{0}C, respectively. Upon decreasing the temperature from 45 ^{0}C to 10 ^{0}C the spectral overlap between QD's emission and R6G's absorption increases slightly (Table 3.3). [174]

Overlap integral [J(λ)] value of QD-R6G FRET pair changes from ~4.6 × 10^{15} $M^{-1}cm^{-1}nm^4$ to ~4.2 × 10^{15} $M^{-1}cm^{-1}nm^4$ with raising the temperature from 10 ^{0}C and 45 ^{0}C (Figure 3.15). From the fitting of $[C(t)]_{FRET}$ we obtained the FRET timescale 400 ps, 470 ps, and 520 ps, respectively at 10 ^{0}C, 25 ^{0}C, and 45 ^{0}C (Figure 3.16, Table 3.3).

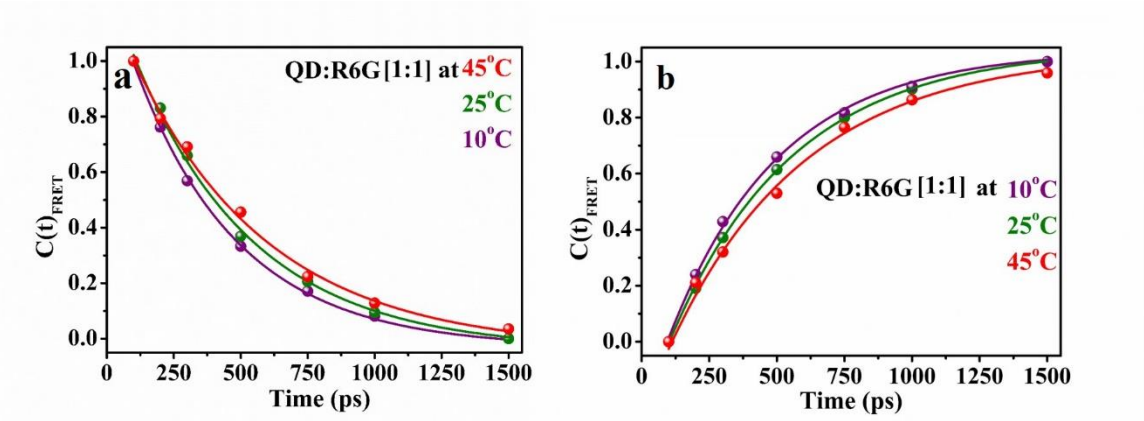

Figure 3.16. Time evolution of the FRET correlation functions [$C(t)_{FRET}$] showing excited state population decay rate of QD* (a) and corresponding population growth rate of R6G (b) at different temperatures. Sold lines represent the single exponential decay and growth fittings to the experimental [$C(t)]_{FRET}$ curves. The QD-to-R6G molar ratio was kept to be1:1 for this experiment. [174]

Table 3.3. Overlap integral values between donor emission and acceptor absorption at different temperatures, and corresponding FRET timescales obtained from TRANES analysis (Figure 3.16). [174]

Temperature	**J(λ) ($M^{-1}cm^{-1}nm^4$)**	**FRET Timescale (ps)**
10°C	4.6×10^{15}	400
25°C	4.5×10^{15}	470
45°C	4.2×10^{15}	520

FRET timescale gets shortened with increasing the J(λ) which is well understood. Our TRANES based analysis is very much responsive to the little change in J(λ) value and provides an accurate analysis of FRET kinetics.

3.11 Conclusion

In this study, we established a model-free analysis of FRET for a QD-based FRET assay, which worked excellently even when the donor and acceptor emit very close. Our fluorescence-based technique addresses many concerns mainly from biologists; where FRET study using transient absorption has inherent difficulties. Using our approach one can utilize QD for more accurate distance measurement in molecular ruler applications. Several attributions of our FRET analysis method has made it unique, greatly different from existing FRET analysis methods.

CHAPTER 4

Artifact due to difference in lifetime Profiles of the FRET Couple: A Detailed Study

4.1 Introduction

This chapter is an extension of the previous chapter. In the extension of the analysis described in the previous chapter, an opposite feature is observed in the time-resolved area normalized emission spectrum when studied for a longer time window. The reversal in the direction of excited state population change dominates the time longer time window. The origin of this opposite feature is explored and it was found to be an artifact. This artifact stems from the dissimilar excited state fluorescence lifetime profiles of the FRET couple used in the FRET study. The artifact may cause erroneous results if its effect is not deconvoluted from the experimental data. In the work presented in this chapter, we used extensive spectral fittings and simulations for de-convoluting the pure FRET components from a mixed process.[34] Our analysis allowed us to resolve the FRET kinetics and kinetics due to natural excited state decay processes in two different time windows and thereby we extracted the pure FRET components from a mixed process.[34] Also our analysis confirms that the opposite feature observed in TRANES is a form of artifact.

4.2 TRANES of Latter Time Window

As discussed in the previous chapter we generated TRANES for the FRET couple QD and R6G for a time window of ~100 ps to ~25 ns. The initial portion of the time window (~100 ps to ~1 ns)

represents FRET between QD and R6G which has already been explained in depth in Chapter 1. In this section, we will have a look at the QD-R6G TRANES in the latter time window of ~3 ns to ~25 ns.

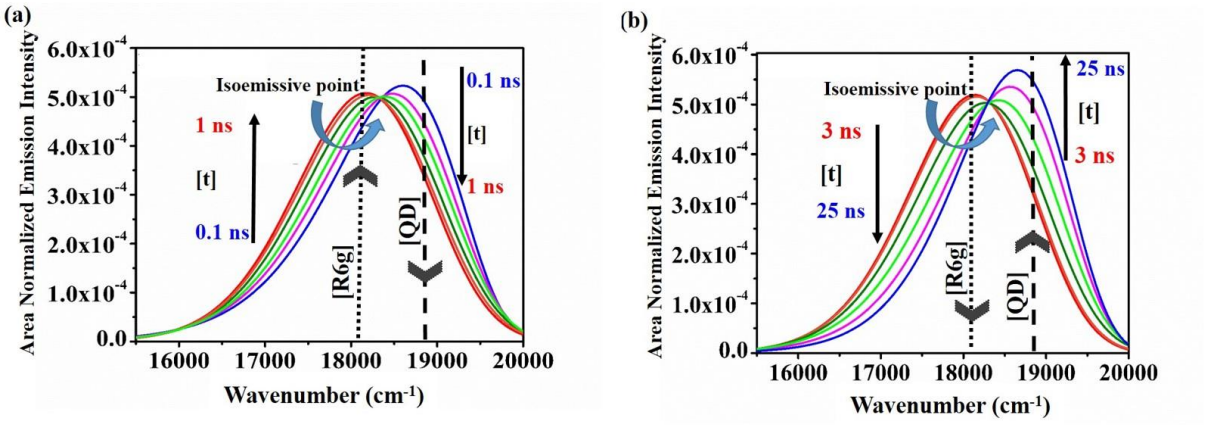

Figure 4.1. Two sets of TRANES of QD-R6G FRET couple (1:2 QD-to-R6G molar ratio at λ_{ex}~375 nm). Figure (a) shows excited state population transfer from QD* to R6G in an initial time window (0.1 ns-1 ns) due to FRET. Figure (b) shows the virtual recovery of the excited state population of QD* from R6G* at a later time window (~3 ns to ~25 ns). Steady-state emission peak positions of QD and R6G are indicated by the vertical dashed and dotted lines respectively. [174]

Figure 4.1 represents the QD-R6G TRANES for a time window of ~100 ps to ~25 ns. A reverse population transfer from R6G to QD along with an isoemissive point can be seen in Figure 4.1 (b). It was the evolution of this opposite feature that made us split the entire time window into two. Further, in the next section, the reason behind this opposite feature will be discussed.

4.3 Lifetime Profiles of QD and R6G

The different processes taking place in the total time window of ~100 ps to ~25 ns are (1) Energy Transfer from QD to R6G and (2) Natural excited state decay of QD and R6G.

The population change in the QD-R6G TRANES in the initial time window is attributed to the first process listed above i.e. FRET from QD to R6G. The natural excited state decay of QD and R6G and their dissimilar lifetimes might be the reason behind the opposite feature in QD-R6G TRANES at the later time window. Figure 4.2 shows the lifetime profiles of QD and R6G. The average excited-state lifetime of QD was ~16ns whereas it was found to be fourfold lesser for that of R6G i.e. ~4ns.

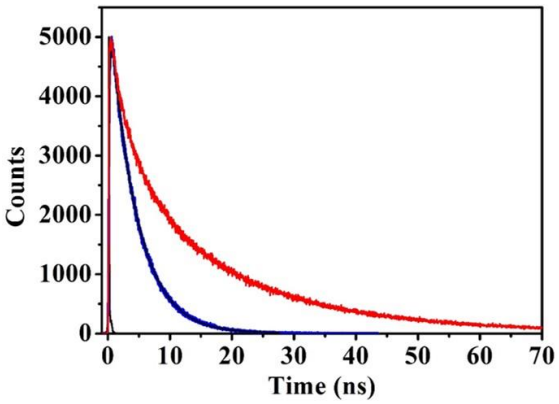

Figure 4.2. Excited-state Fluorescence lifetime decay profiles of QD (red solid line) and R6G (blue solid line) at their respective emission maxima.

We believed that it was the natural excited state decay process that might be inducing errors in the FRET analysis of QD and R6G. According to our hypothesis, the excited state population recovery of QD* here is not due to a reverse FRET mechanism, rather this phenomenon is attributable to the dissimilar excited state natural lifetimes of QD (~16 ns) and R6G (~4 ns). Observed population

recovery of QD* at the latter time regime has no real existence [Figure 4.1 (b)]. During the latter time excited state population of R6G quickly went to the ground state owing to its shorter lifetime but QD* remained alive because of its longer lifetime (~16 ns). These ground state populations of R6G at later times were automatically converted to the excited state population of QD* when the overall excited state population is conserved in TRANES by area normalizing the time-resolved emission spectra (TRES). To verify this hypothesis, we simulated a virtual scenario where FRET between QD and R6G was absent and studied the changes happening in the QD R6G TRANES which were only due to their different natural excited-state lifetimes. The next section of this chapter discusses the simulation of QD-R6G TRANES where FRET is absent.

4.4 Simulation of TRANES in absence of FRET between QD and R6G

We verified the above-mentioned hypothesis using a simulation where we constructed TRANES of QD-R6G couple in the absence of FRET (QD and R6G remained unmixed). Simulated TRANES for QD and R6G non-FRET couples were prepared by adding their individual experimental TRES (QD and R6G were present alone in water) followed by area normalization of the added spectrum to obtain TRANES. Figure 4.3 summarizes the entire simulation process for the generation of TRANES of QD and R6G. Simulated TRANES here would represent the non-FRET phenomenon only, which arises due to dissimilar lifetimes of QD and R6G molecules. This is in contrast to the experimental TRANES (obtained directly from the physically mixed QD and R6G solution) which demonstrate both, non-FRET and FRET phenomena simultaneously.

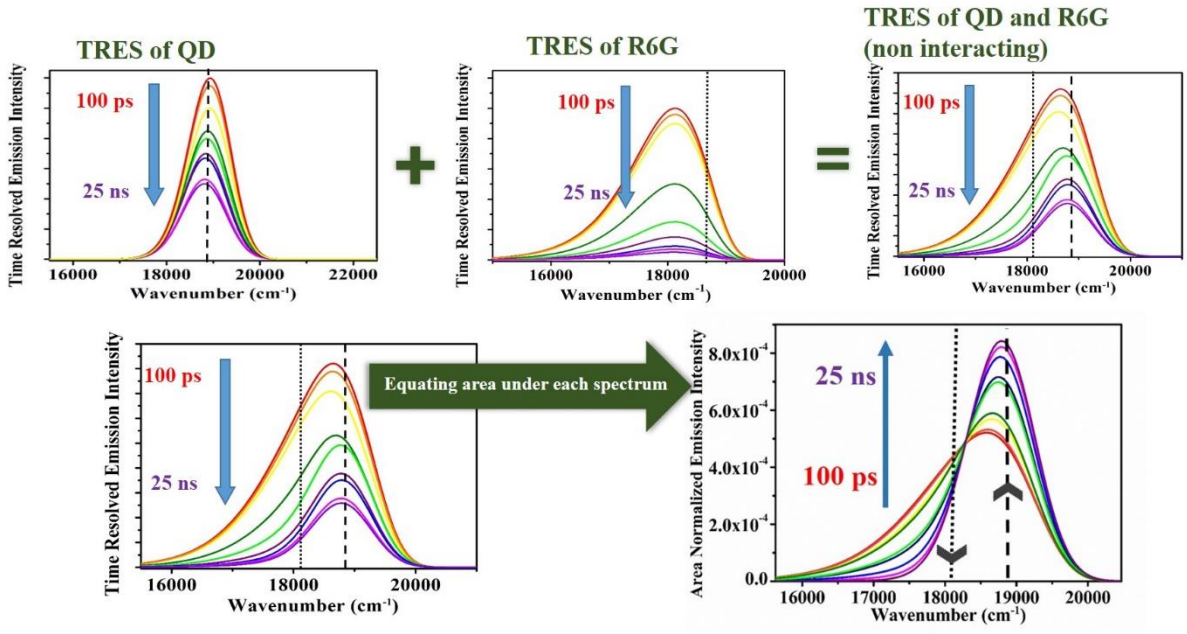

Figure 4.3. The Step by step procedure followed to obtain simulated TRANES for non-interacting (non-FRET) QD-R6G couple: Generation of QD and R6G TRES followed by their addition and normalization to obtain the final simulated TRANES.

Our simulated TRANES (Figure 4.3) were found to closely resemble the later time [Figure 4.1 (b)] experimental TRANES of QD-R6G FRET couple; recovery of QD* population from R6G* population. The time scale of excited state population migration was calculated from the knowledge on how fast the area under the TRANES curve is shifted from R6G* to QD* just like the way described in Chapter 3.

4.5 Bi-lognormal Splitting and Generation of the Correlation Function

To obtain the rate of this reverse change in QD* and R6G* population in the ~3 ns to ~25 ns time window, we fitted each QD-R6G TRANES using the same bi-lognormal equation (Equation 3.2) which we had used in the previous chapter to fit TRANES in the initial time window (~100 ps to

~1 ns). The best-fit parameters were obtained and utilized to split each of the TRANES into the excited state population of QD and R6G. (Figure 4.4)

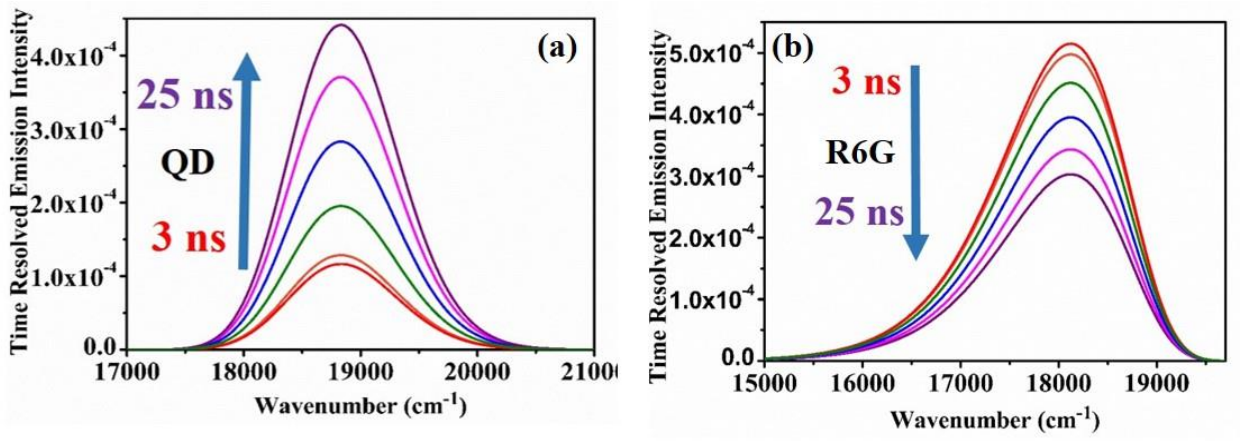

Figure 4.4. Representation of individual split time-resolved emission spectra of QD and R6G obtained from the splitting of corresponding TRANES of QD-R6G complex (1:2) in the later time window: 3ns to 25ns. (a) the emission intensity of QD over time. (b) the emission intensity of R6G over time. [174]

These split time spectra were further processed to obtain the correlation function (exactly like in Chapter 3) and thereby the rate of reverse population transfer was calculated. The population growth of QD* was found to be exactly matching with the population decay of R6G* [Figure 4.5 (a)]. The rate of reverse population transfer came out to be ~8ns.

Similarly, we also constructed $C(t)_{non\text{-}FRET}$ of QD-R6G non-FRET couple from simulated TRANES for the entire ~100ps to 25ns time window [(Figure 4.3 and Figure 4.5 (b)]. The fitting of this $C(t)_{non\text{-}FRET}$ provided us with the timescale (~11 ns) for back transfer of the excited state population. We used exponential fitting functions to fit the C(t)s of QD-R6G FRET and non-FRET couples. As can be seen from the two correlation functions, (1) QD-R6G TRANES obtained directly from experiments (~8 ns) (2) QD-R6G TRANES obtained from simulating a non FRET

scenario (~11 ns), the timescale of reverse population transfer is quite similar. This similarity in the timescales further provides good backing to our proposition of dissimilar lifetimes.

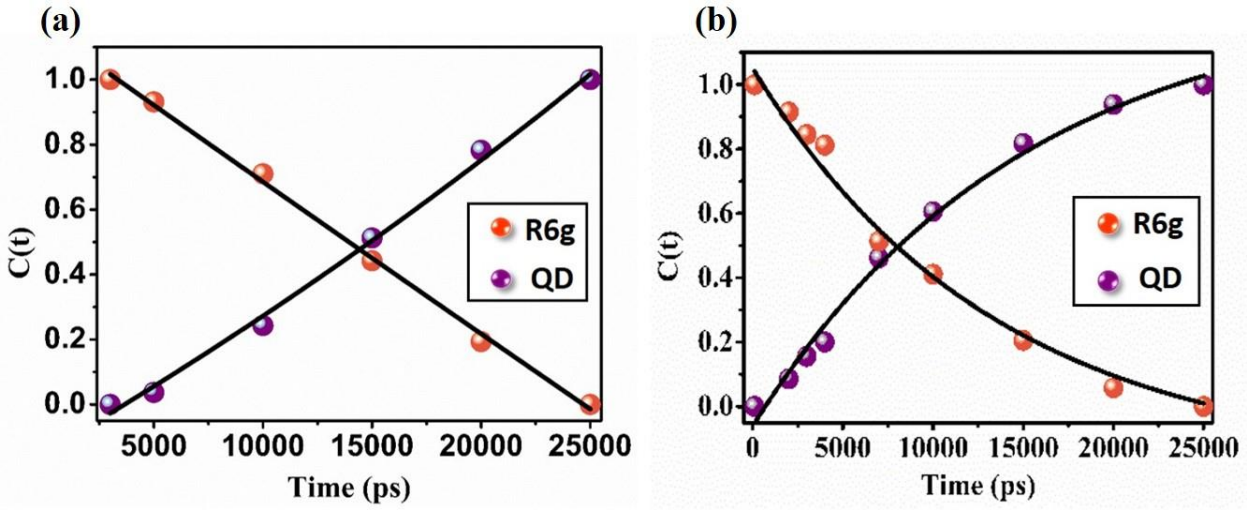

Figure 4.5. (a) The experimental correlation function C(t) of QD-R6G FRET couple during the later time (3ns-25ns); (b) C(t) obtained from our simulated TRANES from 100ps to 25ns; showing non-FRET phenomenon only. [174]

The $C(t)_{non\text{-}FRET}$ obtained from simulating a non FRET scenario [Figure 4.5 (b)] showed a reverse population transfer of R6G* to QD* right from the beginning itself with a population transfer timescale of ~11 ns. This indicates that the reverse population transfer was always present in the FRET timescale analysis and got mixed up with the FRET timescale. However, if the time scale of FRET is largely separated from the timescale of QD*'s population recovery rate, one can fairly assume that these two processes (FRET & excited state kinetics) are taking place independently in two different time windows of TRANES. In our case, FRET time scales (τ_{FRET}) are found to be ~580 ps, 470 ps, and 300 ps (for 1:0.5, 1:1, and 1:2 QD-to-R6G mole ratios), which are in orders of magnitude faster as compared to the excited state population recovery rate (~11 ns) of QD*. In

our case, FRET is completed much before the recovery of the QD* population starts. But if the timescales are similar one can also use our model-free TRANES approach to deconvolute the effect of dissimilar lifetimes from the actual FRET timescale.

4.6 Conclusion

Using the existing FRET analysis methods it is difficult to get rid of natural lifetime decay kinetics from the FRET components. However, our proposed analysis enabled a visual observation of excited state population transfer from donor to acceptor due to FRET during the initial time window and in the later time window just an opposite phenomenon due to the natural excited-state decay kinetics. Using a simple simulation mimicking the phenomenon which arises due to the dissimilar lifetimes of donor and acceptor, one can easily de-convolute the FRET component from a mixed process. Therefore the presented work here is not just merely a spectrum fitting and normalization on an extensively studied system; rather this work has a profound physical significance that will help readers to understand how the natural excited-state decay kinetics affects the FRET components through the visual correlation spectra. To the best of our knowledge, this type of model-free analysis has not been reported earlier which shows a de-convolution of FRET components from a mixed process.

CHAPTER 5

ANALYSIS OF PHOTOINDUCED ELECTRON TRANSFER: THE STOCHASTIC KINETIC MODEL

5.1 Introduction

Cadmium telluride (CdTe) QDs are extensively used in infrared optical devices, sensing applications, and photovoltaic devices for their various attributions, like low production cost, facile synthesis routes, and novel optical properties.[148,183–190] CdTe is known to form alloy materials with zinc (CdZnTe) and mercury (HgCdTe), those alloys are used in X-ray, gamma-ray, and infrared detectors.[191–194] Bulk CdTe has a band-gap of ~1.5 eV and emits in the infrared region (~800 nm).[195] However, when the particle size is reduced to a few nanometers or less, the emission peak position is shifted from infrared to visible or even ultraviolet region. Apart from photovoltaic applications, CdTe QDs being the best alternative to the molecular fluorophores, have appealed to an intense interest of researchers working on various sensing, and bio-application fields.[196] In the last couple of decades, literature has witnessed a burgeoning use of nanoscale semiconductors and their alloys on several occasions for the detection of various analytes in biology and chemistry.[66,197,198] Efficiency of a fluorescence-based sensing application depends on the extent of fluorescence quenching of the sensor molecule either by PET or FRET reaction.[170] CdTe QD emits as a result of the recombination of the exciton. External medium, capping agents, morphology, size, different types of chemical interactions, etc control the fluorescence properties of QD by modifying the energy levels of charge carriers. In the present chapter, we have shown that the physical contacts with the 2,4-dinitrotoluene (DNT) molecule can result in a significant quenching

of CdTe QD fluorescence. This observation indicates a more advanced use of CdTe QD can be the detection of explosive nitro-aromatic compounds. To pave the way for such possibilities, first, an in-depth understanding of the bimolecular quenching process in QD is highly warranted. Bimolecular quenching study in solution is well documented for organic dye molecules.[199–204] Different approaches for fittings based on various approximations and models are proposed in the literature. Using such approaches, attempts are being made by researchers to reconcile steady-state and the time-resolved data under the same set of parameters. The study of bimolecular PET reactions in common solvents gained popularity for the simple nature of the solution phase kinetics. However, the scenario does not remain that simple when the intrinsic PET rate reaches the upper limit of the diffusion-controlled rate of the medium. At this limit, the apparent rate of electron transfer reflects the mass transportation rate of the medium, rather than the actual PET kinetics.[204,205] To extract the intrinsic PET rate in such situations, several models based on different approximations are proposed. For example, a classical model like Smoluchowski assumes that the bimolecular PET can take place only when donor-to-acceptor separation remains within the encounter distance.[206–208] PET rate falls strictly to zero at any other separations. However, this is not true in reality.[204] When the PET rate is higher than the diffusion rate of the medium, the trajectory of PET kinetics moves from a static regime (kinetically controlled) to a stationary regime (diffusion-controlled) via a non-stationary regime.[204] The rate at the static regime is intrinsic. However, in the stationary regime, which is attained after a long time, the rate becomes purely diffusion-controlled for a fast PET process.[204] Contrary to the static and stationary regimes, in the non-stationary regime PET is distance-dependent. Collins−Kimbal model (with the help of a time-dependent sink term), and differential encounter theory (DET) is used to capture all the three regimes of PET kinetics.[204,208] In the present study we chose CdTe QD as a hole scavenger and

DNT as an electron acceptor for their well-matched redox profiles. Photo-excited CdTe QD* were quenched by hole transfer from LUMO of DNT to the conduction band (CB) of photo-excited CdTe QD*.[209] We synthesized three different CdTe QDs varying in their sizes, to tune the energy band gaps of the QD particles.[210] We assumed a Poisson distribution of DNT molecules at the QD surface (within the surface capping layer).[39,211,212]A comprehensive fitting to the experimental data approves the acceptability of our stochastic fitting model, originally proposed by Tachiya in his seminal papers.[213,214] Mechanism of bimolecular PET using QD is different from organic dye mainly in two ways.[215–217] First, in QD static quenching (through QD-quencher complex formation) is more probable than dynamic quenching, because the surface passivating layer of QD can easily trap the quencher molecules. Second, the passivating layer of QD shields the approach of the quencher molecules to a very close to the QD core, which causes an emissive complex formation where efficient PET is retarded. However, in addition to emissive complex formation, QD also forms dark complexes where either no photon from the complex is emitted, or the lifetime of the emitted photon is so quenched that it can't be measured by a time-resolved setup. One can in principle control the PET rate by changing the thickness/density of the polymer layer of QD. Both factors are absent when the organic dye is used instead of QD. PET kinetic due to emissive complex formation is well explained by Tachiya's stochastic kinetic model, which assumes a Poisson distribution of quencher molecules around the QD surface.[39,213,214] Also, the trapping of quencher molecules at the QD surface assures us that even a classical concept of time-independent PET rate (i.e., fixed QD-to-DNT distance during PET) would work well in our case.

5.2 Synthesis of the Quantum Dots

For the synthesis of CdTe QD, cadmium acetate dehydrate [$Cd(CH_3COO)_2.2H_2O$] and tellurium powder was dissolved in an organic solvent trioctylphosphine (TOP) by sonication. The obtained

clear solution was marked as solution 1. In another container dodecaylamine (DDA) was dissolved in TOP and heated at 80^{o} C. This capping agent solution was marked as solution 2. Next, solution 1 was mixed with solution 2 with continuous stirring. The temperature of the final reaction mixture (solution 1 + solution 2) was increased slowly to 145 ^{o} C and maintained this temperature for 4 hours (SCHEME 5.1). The entire reaction was carried out under an inert atmosphere (nitrogen gas). After 4 hours of heating, the mixture was cooled to room temperature to obtain crude CdTe QDs. Similarly, two more batches of QDs were synthesized following the same procedure but different reaction temperatures (165 ^{o} C and 185 ^{o} C). A total of three different variants of QDs (QD145, QD165, and QD185) were synthesized by tuning the reaction temperature (145 ^{o} C, 165 ^{o} C, and 185 ^{o} C)and keeping all other parameters the same.

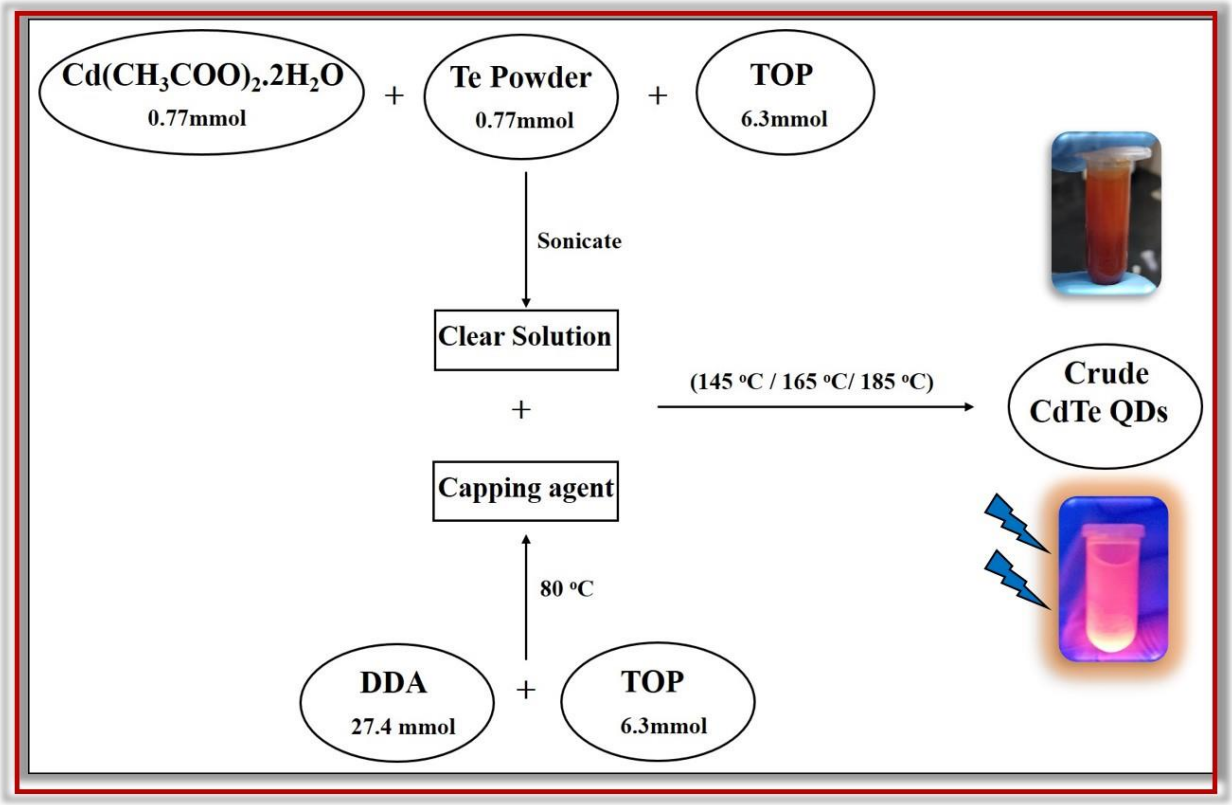

SCHEME 5.1. Reaction scheme for CdTe QD synthesis. [209]

5.3 Purification and Dispersion of QDs in Toluene

All the three batches of crude QDs obtained (QD145, QD165, and QD185) in the previous section were subjected to purification and redispersion into toluene. The impurities and side products were removed by dissolving and centrifuging the reaction mixture in methanol. The supernatant containing the unreacted DDA and Cadmium acetate was discarded while the flocculate containing the CdTe QDs was redispersed and centrifugated into toluene. The following scheme (SCHEME 5.2) can be referred to for a better understanding.

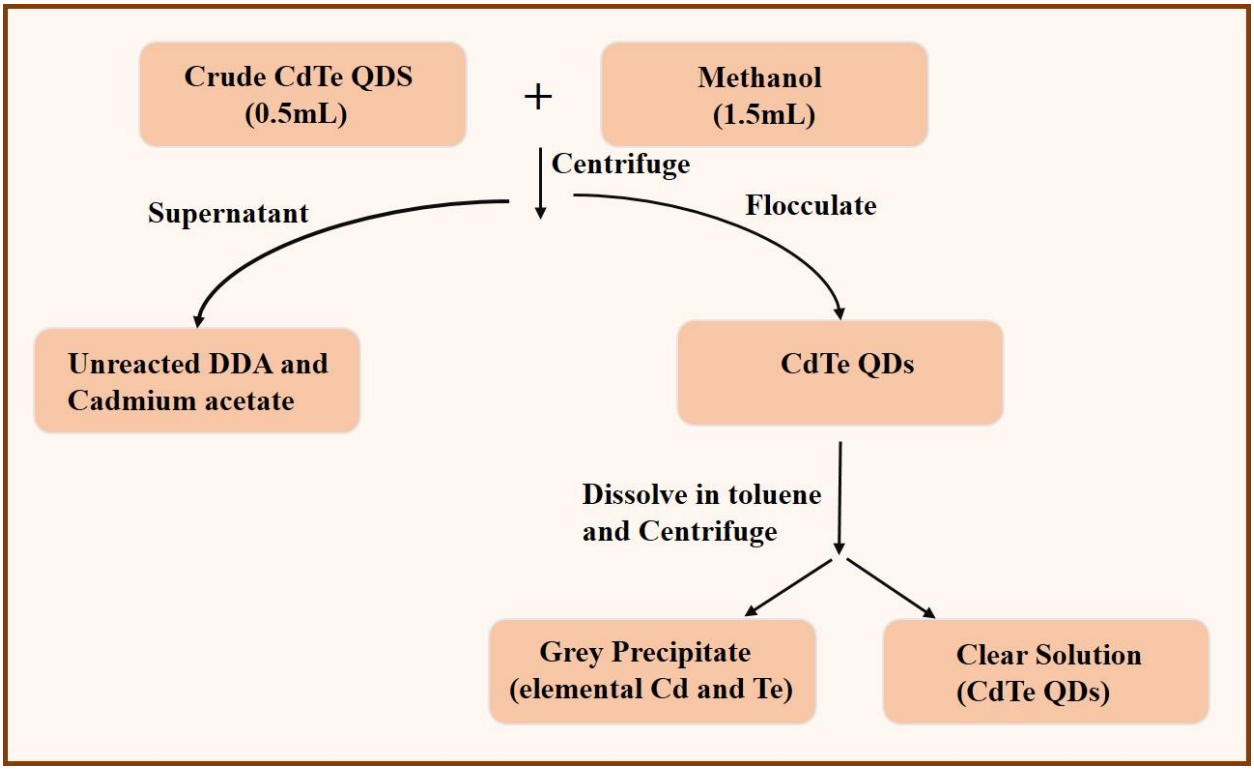

SCHEME 5.2. Schematic representation of the purification procedure followed to obtain the three batches of QDs (QD145, QD165, and QD185). [209]

5.4 TEM Measurements and Spectral Properties

HR-TEM measurements revealed that the low reaction temperature (~145^{o} C) produces small QD particles (~3.2 nm), while at high temperature (~185^{o} C) relatively large (~5.2 nm) particles are formed. At an intermediate temperature (~165^{o} C) particle size of ~4.2 nm was obtained (Figure 5.1).

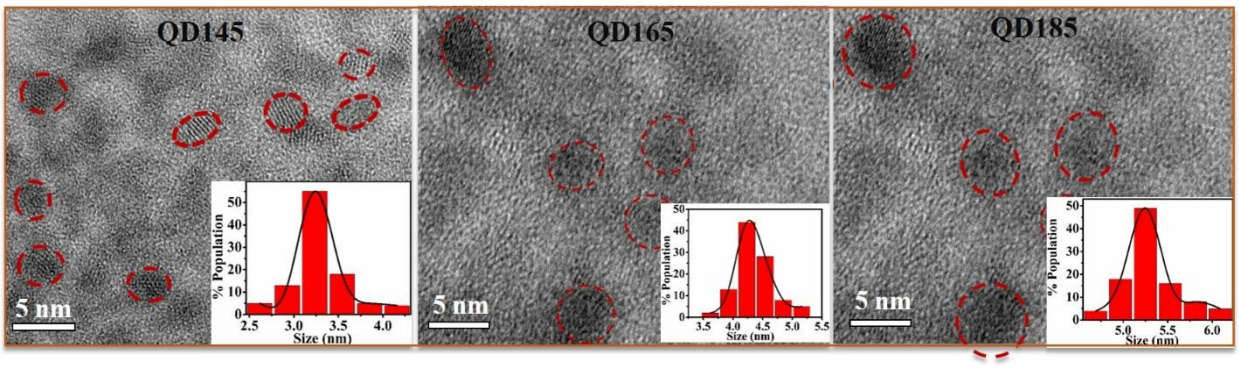

Figure 5.1. High-resolution TEM images along with the particle size distributions (inset) of CdTe QDs synthesized at various temperatures namely, 145° C, 165° C, and 185° C, respectively (left to right). [209]

However, DLS measurements revealed a much larger size compared to HR-TEM. This is because, unlike TEM which measures only the crystalline part of QD, DLS measures the QD sizes including the surface passivating layer (DDA) and the hydration layer. Using DLS, the sizes of QDs were measured to be ~8 nm (QD145), ~16.5 nm (QD165), and ~19.5 nm (QD185). The optical density (OD) of absorption spectra showed a sharp diminishing nature at longer wavelengths (>550-625 nm), but the OD increased monotonously at the blue side (<550-625 nm) (Figure 5.2).

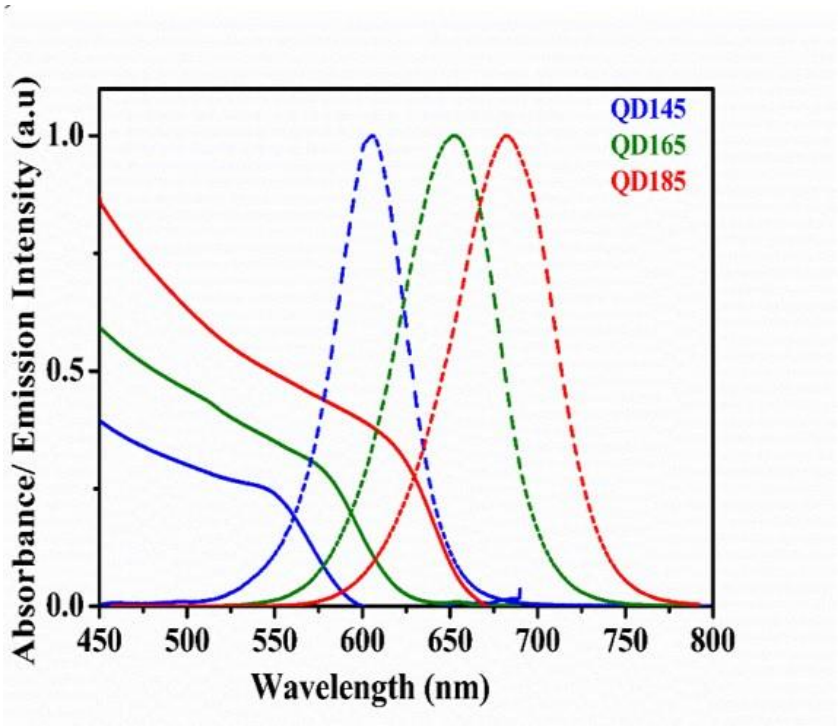

Figure 5.2. Spectral signatures of the three QDs as-synthesized at different temperatures: 145^{o} C (blue line), 165^{o} C (green line), and 185° C (red line), respectively. Solid curves represent the absorption spectra while the dotted curves represent the emission spectra. [209]

The absorption feature did not have a peak and remained the same for all three particles. The emission peak position of CdTe QD was shifted from ~600 nm (QD145) to ~700 nm (QD185) with increasing the QD particle size (Figure 5.2). This variation in optical features of the synthesized QDs with the particle size is justified and well documented in various reports. As the size of the nanoparticle increases the bandgap also increases which responsible for the redshift in the emission spectra.

5.5 Fluorescence Quenching: Steady-State and Time-Resolved

A step by step addition of DNT to all the three batches of synthesized QDs (QD145, QD165, and QD185) caused a regular quenching in the steady-state fluorescence intensity as well as the excited state fluorescence lifetime of the QDs. Quenching in the steady-state emissions and the excited-state lifetimes is depicted in Figure 5.3 whereas the exact lifetime values are provided in Table 5.1.

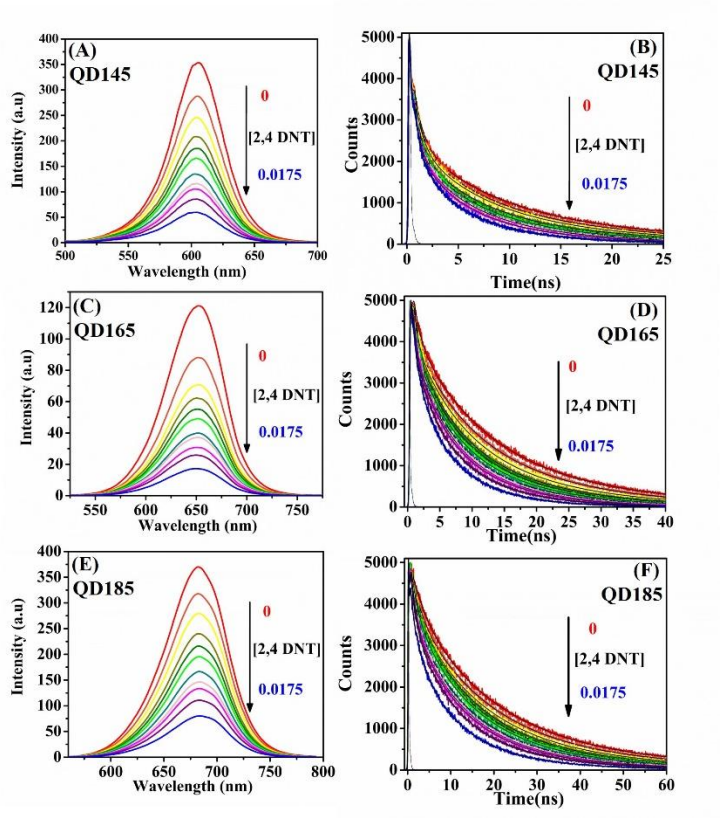

Figure 5.3. Quenching of steady-state emissions (A, C & E) and fluorescence lifetimes (B, D & F) of QD145 (A & B), QD165 (C & D), and QD185 (E & F) upon gradual addition of DNT. DNT concentration is in moles/liter. QD samples were excited at 405 nm and the fluorescence lifetimes were collected at their respective emission peaks. [209]

Table 5.1. Average lifetimes of quantum dots (QD145, QD165, and QD185) at different DNT (quencher) concentrations.

QD	DNT Concentration [M]	Average lifetime (ns)
QD145	0	6.96
	0.0010	6.72
	0.0025	6.00
	0.0040	5.20
	0.0050	5.08
	0.0060	4.62
	0.0075	3.98
	0.0090	3.68
	0.0100	3.47
	0.0125	3.01
	0.0175	2.48
QD165	0	10.22
	0.0010	8.68
	0.0025	7.48
	0.0040	6.31
	0.0050	6.1
	0.0060	5.27
	0.0075	5.16
	0.0090	4.63

	0.0100	4.56
	0.0125	3.74
	0.0175	3.04
QD185	0	18.53
	0.0010	16.80
	0.0025	14.57
	0.0040	13.97
	0.0050	13.38
	0.0060	12.22
	0.0075	10.94
	0.0090	10.04
	0.0100	9.51
	0.0125	8.36
	0.0175	7.35

5.6 Photoinduced Electron Transfer: Redox Profile of the Pair

As can be seen in the previous section the quenching of QD* emission can be attributed to one of the three probable quenching mechanisms: 1) FRET from QD* to DNT, 2) hole transfer from LUMO of DNT to the conduction band (CB) of QD*, and 3) electron transfer from the HOMO of DNT to the valance band (VB) of QD*.

Mechanism 1 can be easily ruled out by having a look at the spectral features of the three QDs and DNT (Figure 5.4). From Figure 5.4 it can be seen that there is no significant amount of spectral overlap between the emission spectrum of QD* and the absorption spectrum of DNT which confirms that FRET between the QDs and DNT is not possible.

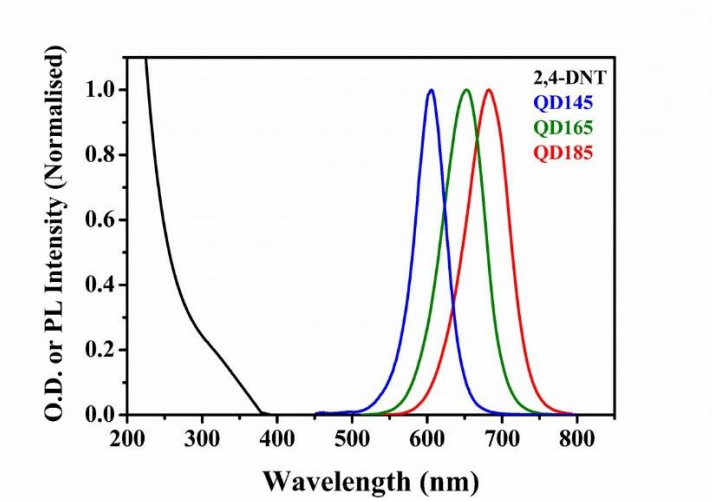

Figure 5.4. The absorption spectrum (black line) of DNT and emission spectra of QD145 (blue line), QD165 (green line), and QD185 (red line). There is no spectral overlap between DNT's absorption spectrum and any of the three QDs emission spectrum. [209]

Further from mechanisms 2 and 3, mechanism 3 can be ruled out by observing the redox potential profile of the QDs and DNT (SCHEME 5.3). From the redox profile of the QDs and DNT, it is evident that mechanism 3 is thermodynamically forbidden since the HOMO level of DNT is much lower in energy compared to the VB energy of QD. Therefore, the only mechanism that can cause quenching of QD* emission is mechanism 2, the hole transfer from LUMO of DNT to the CB of QD*.

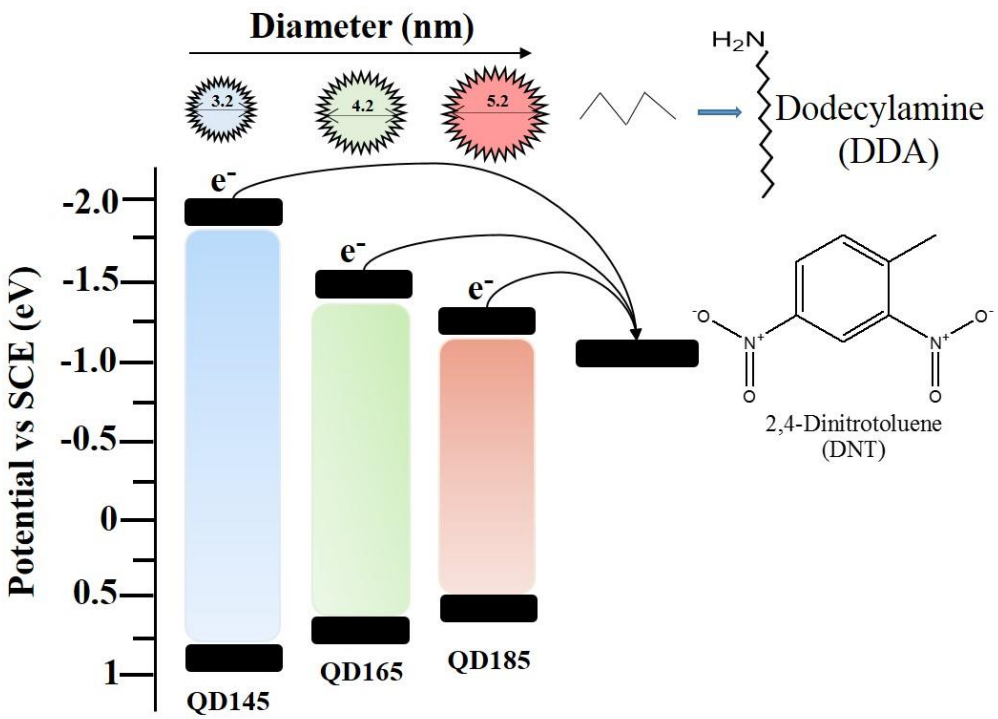

SCHEME 5.3. Redox profiles of QDs and a DNT molecule. Energy levels of QDs were calculated using Brus Equations as described in Chapter 2 of the thesis. [209]

In SCHEME 5.3, the lowest excited state [$1S_{3/2}$(h)-1S(e)] energy and redox potentials of QD* were calculated using a spherical QD with an infinite potential barrier assumption, proposed by Brus.[78,146] Further details of band energy calculation can be found in Chapter 2 of the thesis.

5.7 Tachiya's Stochastic Model: An Insight

Unlike the bimolecular quenching mechanism of organic dyes (i.e., coumarins) where quenching is mostly collisional, in QDs, trapped quencher molecules in the surface capping layer may cause the quenching (Scheme 5.4).[128,132,132,218–220]

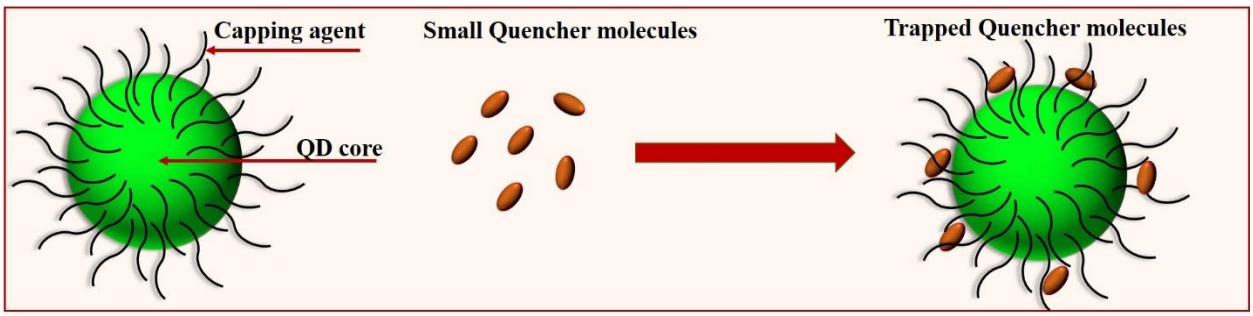

SCHEME 5.4. Schematic representation of trapped small quencher molecules on the QD surface.

In a seminal work, Patra and Tachiya proposed a stochastic kinetic model to explain the FRET kinetics from CdS QD/rods to Nile red, using similar assumptions.[39] We borrowed the same stochastic model and used it in our PET study, which enabled comprehensive fittings to our experimental data. If we assume that the PET rate coefficient is a time-independent parameter (as QD-to-DNT distance remains fixed in QD-DNT complex during PET) and n quencher molecules are trapped at the QD surface of an emissive complex, then the excited state population of QD* will decay through two independent decay channels (with rate coefficients k_0 and k_q) as follows,

$$QD_n^* \xrightarrow{k_0 + nk_q} QD_n \qquad (5.1)$$

Where, k_0 is the unimolecular excited state decay constant of QD* in the absence of quencher molecule and k_q is the PET rate coefficient per quencher molecule. When QD with n quencher molecules attached is excited, the overall excited state decay constant will be k_0+nk_q and the electron transfer rate constant will be nk_q. In our fittings, we assumed that n DNT molecules are attached to a QD (in an emissive complex) following a Poisson distribution. If there is an average m number of quencher molecules attached to a single QD, the population of QD attached to n DNT will be,[39,213,214]

$$\Theta(n) = \left(\frac{m^n}{n!} \right) \exp(-m) \tag{5.2}$$

In TCSPC we measured an ensemble-averaged excited state decay of QD* when one QD is attached to an average m number of DNT molecules. We can generate a fitting equation (equations 5.3-5.4) for an ensemble-averaged decay profile of QD* of an emissive complex where one QD is attached to an average m number of DNT molecules considering all probable values of n (0 to ∞).[39,211–215]

$$I(t,m) = I_0 \int_{n=0}^{n=\infty} \Theta(n) \exp[-(k_0 + nk_q)t] \tag{5.3}$$

$$I(t,m) = I_0 \exp\left[-k_0 t - m\left\{1 - \exp(-k_q t)\right\}\right] \tag{5.4}$$

When k_0 is much smaller compared to k_q, the initial portion of the excited state decay profile of QD* in the presence of quencher is fast and controlled by the factor $\exp(-k_q t)$. However, at a later time, the decay profile is exponential with a slope k_0 (equation 5.5).

$$I(t,m) = I_0 \exp(-m) \exp(-k_q t) \tag{5.5}$$

Equations 5.4 is expected to enable comprehensive fittings to the experimental intensity decay curves. The later time slope (k_0) of the decay curves (of QD* emission) in the presence of a quencher should match with the slope of the same in the absence of a quencher. However, the slope of QD*emission decay in the absence of DNT is not exponential. Unidentified trap sites at the QD surface are the reason behind not observing an exponential nature in emission decay profiles.[39] If m_t be the mean number of trap sites per QD present following a Poisson distribution,

then the intensity decay profile of QD* in the presence of DNT and trap sites is described by,[39,213,214]

$$I(t,m) = I_0 \exp\left[-k_0 t - m\left\{1-\exp(-k_q t)\right\} - m_t\left\{1-\exp\left(-k_{qt} t\right)\right\}\right] \quad (5.6)$$

In the absence of DNT but presence of trap sites, the decay profile is described by,

$$I(t) = I_0 \exp\left[-k_0 t - m_t\left\{1-\exp\left(-k_{qt} t\right)\right\}\right] \quad (5.7)$$

Where k_{qt} is the quenching constant per defect site.

5.8 The Survival Probability Function

Equation 5.6 is indeed more complicated than equation 5.4, because of the coexistence of trap sites and quencher molecules. For the fitting to the actual emission decay profiles (in Figure 5.3 B, 5.3 D & 5.3 F) the effect of the excitation lamp profile must be considered within the fitting equations (Equation 5.6 & 5.7). However, one can easily avoid these complications (i.e., incorporation of lamp profile and trap sites) by simply taking the ratio I(t,m)/I(t) as,[132,182]

$$S_q(t,m) = \frac{I(t,m)}{I(t)} = I_0 \exp\left[-m\left\{1-\exp(-k_q t)\right\}\right] \quad (5.8)$$

The above equation is much simpler compared to its previous form (Equation 5.6). $S_q(t,m)$ is called the excited state survival probability function which is free from the effects of lamp profile, trap sites and only depends on the electron transfer rate.[132,182] It is noteworthy that $S_q(t,m)$ functions are obtained from the exploitation of lifetime quenching data, where the non-emissive complex has no contribution. A different approach (Stern-Volmer approximations) based on the steady-state emission quenching was employed to analyze the PET kinetics of non-emissive complexes, which will be discussed in the latter part of the chapter. We used this equation (Equation 5.8) to

fit our experimental survival probability function obtained by normalizing the excited state decay profile of QD* in the presence of DNT by the same in the absence of DNT [i.e., I(t,m)/I(t)]. Figure 5.5 depicts the experimental $S_q(t,m)$ profiles along with the fitted lines (using equation 5.8) at three different DNT concentrations (0.001, 0.0075, and 0.0175 moles/lit).

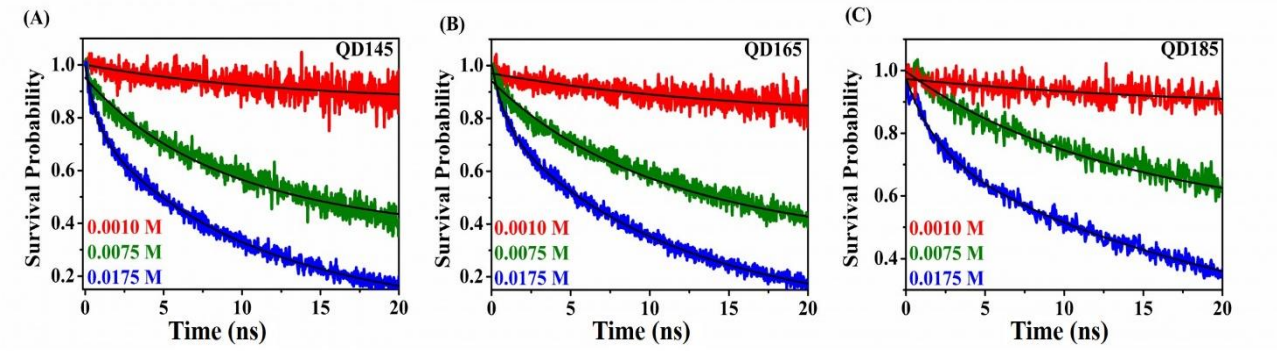

Figure 5.5. Representation of the obtained survival probability functions of emissive complexes along with their best fit (black solid lines) for A) QD145, B) QD165 & C) QD185 in the presence of 0.001M, 0.0075M, and 0.0175M of DNT. [209]

The fitted values for all the three QDs at different DNT concentrations are provided in Table 5.2 The mean number of DNT molecules (m) attached to a single QD in the emissive complex was found to be increasing from ~0.1-0.19 to ~1.2-1.7 as the DNT concentration was increased from 0.001M to 0.0175M (Table 5.2). PET rate of QD-DNT emissive complex was seen to be decreasing moderately with increasing the size of the QD. The smallest particle QD145 recorded the highest PET rate constant (k_q~0.072 ns^{-1}) per quencher molecule, while the largest QD (QD185) exhibited the lowest value of k_q (~0.05 ns^{-1}) (Table 5.2). The PET rates of emissive complexes are commensurate to their chemical driving forces (ΔG_0), as calculated from the Rehm-Weller equation (Table 5.2, Chapter 2 for ΔG_0 calculation).[132,182]

Table 5.2. Values of fitting parameters of survival probability functions (Figure 5.5) using equation 5.8. [209]

[DNT] (M)	Number of DNT/QD (m)			k_q (ns^{-1})			ΔG_0 (ev)		
	QD145	QD165	QD185	QD145	QD165	QD185	QD145	QD165	QD185
0.0010	0.16	0.19	0.10						
0.0025	0.34	0.42	0.22						
0.0040	0.56	0.59	0.35						
0.0050	0.65	0.74	0.46						
0.0060	0.80	0.85	0.54						
0.0075	0.95	1.07	0.73	0.072	0.055	0.050	-3.70	-2.70	-2.20
0.0090	1.07	1.23	0.81						
0.0100	1.18	1.36	0.89						
0.0125	1.37	1.54	1.06						
0.0175	1.63	1.73	1.25						

The PET rate constants in the above section were obtained from exploiting the time-resolved data, where only the emissive complex could contribute. In contrast, dark-complex either can emit photons with exceedingly shorter lifetimes (i.e., shorter than the IRF of the time-resolved instrument), or it can be completely dark without having an emission. In both of these cases, lifetime remains unaffected. Therefore one can rule out the contribution of the dark complexes in lifetime quenching. However, both dark complex and emissive complex can contribute to steady-state fluorescence quenching. Steady-state fluorescence intensity depends on the number of emitting molecules. Since dark complex formation reduces the number of emitting molecules, which in result will also decrease the steady-state intensity. We also tried to fit our steady-state quenching data with the same set of parameters obtained from the fittings to the time-resolved data

using Tachiya's stochastic model (Figure 5.5). However, we were unable to arrive at a conclusive fitting. This is because the steady-state quenching was controlled by the formation of both, dark and emissive complexes, while the lifetime quenching was controlled by only the emissive complex formations. The steady-state intensity quenching can be expressed by the following equations if the same stochastic kinetic model is used.[39,211–214]

$$\frac{I}{I_0} = \frac{\left\{\sum_{n=0}^{\infty}\sum_{n'=0}^{\infty}\left(m^n e^{-m}/n!\right)\left(m_t^{n'}e^{-m_t}/n'!\right)/[1+nk_q/k_0+n'k_{qt}/k_0]\right\}}{\sum_{n'=0}^{\infty}\left(m_t^{n'}e^{-m_t}/n'!\right)/[1+n'k_{qt}/k_0]} \tag{5.9}$$

or,

$$\frac{I}{I_0} = \frac{\left\{e^{-m}\sum_{n'=0}^{\infty}\left(m_t^{n'}e^{-m_t}/n'!\right)/[1+n'k_{qt}/k_0]\right\}}{\sum_{n'=0}^{\infty}\left(m_t^{n'}e^{-m_t}/n'!\right)/[1+n'k_{qt}/k_0]} + \frac{\left\{\sum_{n>0}^{\infty}\sum_{n'=0}^{\infty}\left(m^n e^{-m}/n!\right)\left(m_t^{n'}e^{-m_t}/n'!\right)/[1+nk_q/k_0+n'k_{qt}/k_0]\right\}}{\sum_{n'=0}^{\infty}\left(m_t^{n'}e^{-m_t}/n'!\right)/[1+n'k_{qt}/k_0]} \tag{5.10}$$

or,

$$\frac{I}{I_0} = e^{-m} + \frac{\left\{\sum_{n>0}^{\infty}\sum_{n'=0}^{\infty}\left(m^n e^{-m}/n!\right)\left(m_t^{n'}e^{-m_t}/n'!\right)/[1+nk_q/k_0+n'k_{qt}/k_0]\right\}}{\sum_{n'=0}^{\infty}\left(m_t^{n'}e^{-m_t}/n'!\right)/[1+n'k_{qt}/k_0]} \tag{5.11}$$

Due to the complex nature of equation 5.9, it is difficult to use in the fitting of steady-state quenching data, at least in the present form. In the next step (Equation 5.10) the right hand side of equation 5.9 (n= 0 to ∞) is split into two parts (n=0 and n= >0 to ∞). The first part (n=0) is further reduced to e^{-m} (equation 5.11). The second part (n= >0 to ∞) of equation 5.10 can be simplified in a special case when k_0 ($=1/\tau_{long}$) is much lower than k_q; then k_q/k_0 will be much larger than unity. τ_{long} is the longest component of the lifetime of QD* in the absence of DNT. Let us evaluate the value of "$(1+nk_q/k_0 + n'k_{qt}/k_0)^{-1}$" in the second part (of right hand side, for n= >0 to ∞) of equation 10 and 11, when $k_q/k_0 >> 1$. When $n \neq 0$ (i.e., n can be anything between 0 and ∞), the value of nk_q/k_0

will be infinitely large. Therefore, the value of "$(1+nk_q/k_0+n'k_{qt}/k_0)^1$" will be zero. Hence, equation 5.11 can be further reduced to equation 5.12 as follows (assuming $k_q/k_0>>1$),

$$\frac{I}{I_0} = e^{-m} \tag{5.12}$$

However in our case the values of k_0 ($=1/\tau_{long}$) are 0.046 ns^{-1} (QD145), 0.045 ns^{-1}(QD165) and 0.024 ns^{-1}(QD185), not much different from their respective k_q values (0.072 ns^{-1}, 0.055 ns^{-1} and 0.050 ns^{-1}). Therefore equation 5.2 may not be an appropriate fitting equation for our steady-state quenching data, as k_q/k_0 is not >>1.

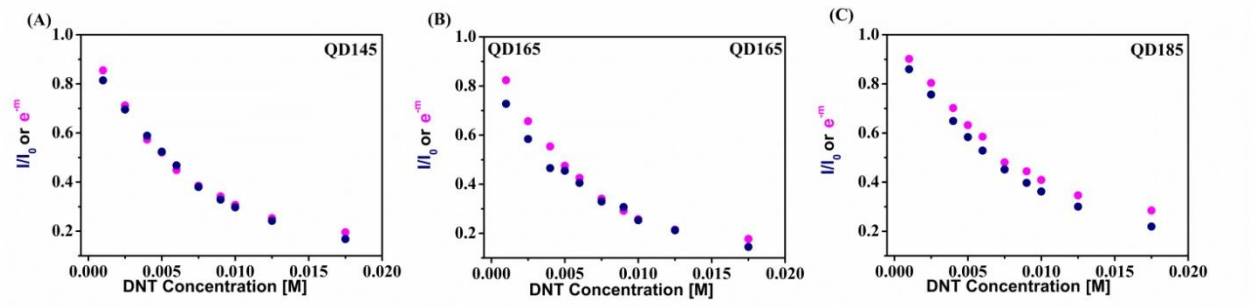

Figure 5.6. Graphs of I/I_0 (navy blue, obtained from steady-state emissions) and e^{-m} (magenta), obtained from the fittings of time-resolved data in Figure 5.5 as a function of DNT concentration for all the three QDs: A) QD145, B) QD165 and C) QD185. [209]

In Figure 5.6, we plotted experimental steady-state I/I_0 as a function of DNT concentration. In the same window, e^{-m} (Equation 5.12) was plotted as a function of DNT concentration. The value of m for a particular DNT concentration was obtained from the fitting of the survival probability function using equation 5.8, as described in the earlier section (Table 5.2). For all the three QDs, we observed a nice correlation was missing between e^{-m} (Equation 5.12) and steady-state I/I_0. This

is because equation 5.12 is an approximated form of equation 5.11 assuming $k_q/k_0>>1$, but in our case k_q/k_0 was not >>1. Therefore a more accurate equation for the fitting of steady-state emission in our case was equation 5.11, rather than equation 5.12. Nevertheless, a conclusive fitting with equation 5.12 was not possible as we missed the contribution of the dark complex in time-resolved fitting, but the same is detected in steady-state quenching analysis. One can reconcile the steady-state and time-resolved quenching data using the same set of parameters when the entire PET kinetic is detected by both the measurement techniques (i.e., time-resolved and steady-state).

5.9 Classic Stern-Volmer Analysis

We fitted our data using the classic Stern-Volmer (SV) fitting equation.[21] The steady-state SV plot exhibited a bent upward curvature at high quencher concentration and the slope of the steady-state SV curve was found to be always higher than the slope of the time-resolved SV plot (Figure 5.7). Time-resolved SV plots were easily fitted with a linear fitting equation ($I_0/I= 1+\tau_0 k[Q]$). Where k is the PET rate coefficient, τ_0 is the lifetime of QD* in the absence of quencher, and [Q] is the quencher concentration.

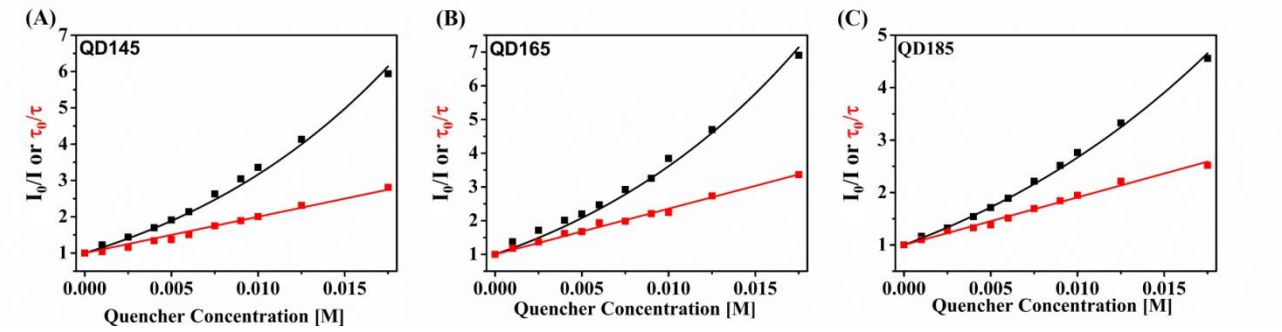

Figure 5.7. Steady-state and time-resolved Stern-Volmer plots (black and red square boxes) along with their best fits (black and red solid curves) for A) QD145, B) QD165 and C) QD185. [209]

Steady-state SV curve was fitted with a more complicated equation, $I_0/I=(1+\tau_0 k[Q])\exp(K[Q]$, assuming a dark complex formation between QD and quencher molecule with an associated equilibrium constant of K.[21] Fitting parameters are summarized in Table 5.3. The PET rate coefficient (k) was found to be decreasing from ~14.5×10^9 $M^{-1}S^{-1}$ to ~5×10^9 $M^{-1}S^{-1}$ as the QD size increased (QD145 to QD185). Nearly 3 times change in PET rate predicted by SV plot with changing QD size is more drastic compared to the change (0.072 ns^{-1} to 0.05 ns^{-1}) observed using Tachiya's kinetic model (Table 5.2 & 5.3). PET rate coefficient obtained from the fitting of lifetime SV plot is the PET rate of the emissive complex rather than a collisional quenching.

Table 5.3. Values of the Stern-Volmer fitting parameters (Figure 5.7).[209]

Quantum Dot	[DNT] (M)	I0/I	m	e^{-m}	kq (M^{-1} S^{-1})	K (M^{-1})
QD145	0.0010	1.23	0.16	0.86	14.5×10^9	46
	0.0025	1.44	0.34	0.71		
	0.0040	1.70	0.56	0.57		
	0.0050	1.91	0.65	0.52		
	0.0060	2.14	0.80	0.45		
	0.0075	2.63	0.95	0.39		
	0.0090	3.04	1.07	0.34		
	0.0100	3.36	1.18	0.31		
	0.0125	4.13	1.37	0.25		
	0.0175	5.94	1.63	0.20		
QD165	0.0010	1.37	0.19	0.82	13.0×10^9	43
	0.0025	1.71	0.42	0.66		
	0.0040	2.15	0.59	0.55		
	0.0050	2.20	0.74	0.47		
	0.0060	2.47	0.85	0.43		
	0.0075	3.03	1.07	0.34		
	0.0090	3.26	1.23	0.29		
	0.0100	3.94	1.36	0.26		
	0.0125	4.70	1.54	0.22		
	0.0175	6.91	1.73	0.18		
QD185	0.0010	1.16	0.10	0.90	5×10^9	34
	0.0025	1.32	0.22	0.80		
	0.0040	1.54	0.35	0.70		
	0.0050	1.71	0.46	0.63		
	0.0060	1.89	0.54	0.59		
	0.0075	2.21	0.73	0.48		
	0.0090	2.52	0.81	0.44		
	0.0100	2.76	0.89	0.41		
	0.0125	3.33	1.06	0.35		
	0.0175	4.56	1.25	0.28		

To confirm the nature of quenching is not collisional we performed the ITC experiment which reveals a one-to-one (QD-DNT) complex formation that is discussed elaborately in the subsequent section of this chapter. The binding constant (K) of the dark complex obtained from steady-state SV fitting showed that the smaller QD (QD145) exhibits a higher (~46 M^{-1}) binding constant than that (~34 M^{-1}) for a bigger QD (QD185) (Table 5.3). It may be noted that the discrepancy between lifetime and steady-state SV plot can arise only when there is an involvement of dark complexes. Being non-emissive (or having an ultra-short lifetime), the dark complex can't be detected in the lifetime SV plot, but the same is detected in the steady-state SV plot. On contrary to dark complexes, emissive complexes are equally visible in the lifetime and steady-state SV plots, thus no difference between lifetime and steady-state SV plots is observed. A significant difference between steady-state and time-resolved SV curves in our case confirmed the presence of dark complex formations. Fitting with Tachiya's stochastic kinetic model reveals that the smaller QD (QD145) interacts with more numbers (~0.16-1.63) of quencher molecules compared to the number (0.10-1.25) of quencher molecules a bigger QD (QD185) interacts at any quencher concentrations (Table 5.2). This is incongruent to the fact that a smaller QD (QD145) exhibited a higher value of the equilibrium constant (46 M^{-1}) of dark complex formation compared to that (34 M^{-1}) for a bigger QD (QD185) as obtained in SV analysis. Size is not the only parameter that controls binding kinetics. The density of the capping layer may be higher for smaller particles, which helps to trap the more number of quencher molecules for QD145.

5.10 Isothermal Titration Calorimetry

To confirm that the PET kinetic obtained from lifetime quenching (in SV analysis and Tachiya's stochastic kinetic model) is not collisional, we performed isothermal titration calorimetry (ITC)

study.[131] ITC study provided us direct evidence of the binding of DNT with QD (Figure 5.8).[131] Through ITC measurement one can get a direct estimation of various thermodynamical parameters associated with the binding process. In the ITC study, DNT as a titrant was loaded in the syringe, which was injected into the cell filled with QD solution (QD185 in toluene). QD concentration in the cell was much lower compared to the DNT concentration in the syringe. A total of 38μl of DNT solution (DNT in toluene) was added to the cell (QD in toluene) using 38 consecutive injections. Total heat change associated with each injection was noted, which was due to the binding and dilution of DNT molecules.

Heat change due to the dilution of QD (titrand) was negligible, as the extent of dilution was very less for already diluted QD solution. Heat change for dilution of DNT was subtracted from the total heat change for every injection. After subtraction, the remaining heat change obtained accounts for binding only, which was further exploited to obtain binding constant (K). This K included both types of bindings; emissive and non-emissive complexation. A strong interaction of DNT with QD was reflected in the high values of heat change associated with each injection of DNT (Figure 5.8). The equilibrium binding constant (K) was found to be ~400 M^{-1} for the QD185-DNT system. The binding constant (~34 M^{-1}) obtained from the SV plot was found to be an order of magnitude lower compared to that (~400 M^{-1}) obtained from the ITC study.

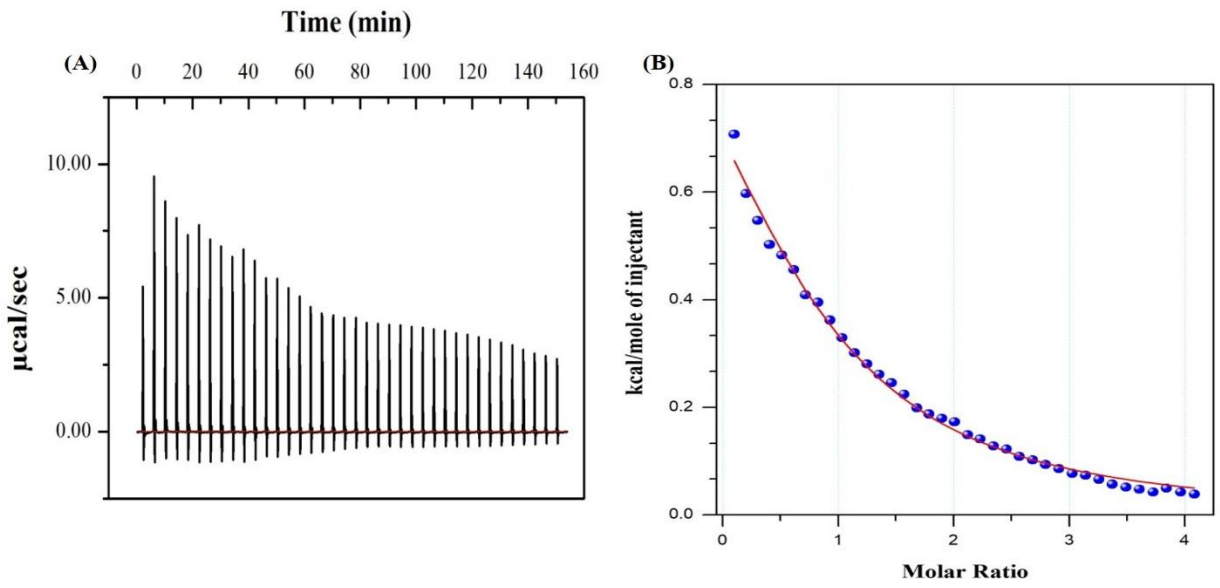

Figure 5.8. ITC profiles for the binding thermodynamics of DNT to QD185. A) Raw data of heat change against each injection (1 µl) of high concentration DNT (in toluene) to the low concentration QD185 (in toluene) taken in the sample cell at 20 ^{0}C. B) Integrated heat change as a function of molar ratio [DNT/QD] after correction with the heat of dilution of DNT. The red line in figure B shows the best fit assuming one site binding. [209]

Undoubtedly, ITC measured binding constant value is more reliable than the value obtained from SV fitting, as the former technique provides a direct estimation of the K value from heat change, irrespective of the spectroscopic nature of the complex (emissive or dark). However, SV fitting assumes donor-acceptor complex must be optically dark and being dark this complex will not emit a photon whose lifetime can be measured. Hence, the overall fluorescence lifetime was not changed due to dark complex formation. Unlike lifetime, steady-state intensity depends on the number of emitting molecules. The formation of a dark complex reduces the number of emitting molecules that cause quenching of the steady-state emission. Therefore in SV analysis, only the

dark complex was detected and not the emissive complex, while in ITC both the complexes were detected since the formation of both will result in a heat change. Therefore, different K values were obtained from different techniques (ITC and SV) and it is well justified.

5.11 Classical SV vs Stochastic Model

PET rate of the emissive complex was independently estimated using two methods; lifetime SV analysis and analysis with a stochastic kinetic model. In both cases, we exploited the time-resolved data where the emissive complex only contributes. Although both the methods provided us PET rate coefficients of a QD-DNT emissive complex we found Tachiya's stochastic model is more reliable since this model represents a more realistic picture of the QD-DNT complex where DNT molecules are distributed at the QD surface following a Poisson distribution. At higher quencher concentration (>0.01 M) more than one quencher molecules interact with a single QD. SV analysis at higher quencher concentration is not adequate, since it fails to explain the kinetics when multiple quencher molecules are involved in the quenching process. Besides, the high-value of binding constant (K~400 M^{-1}) obtained from the ITC study indicated that the collisional quenching was less probable in our system. Lifetime SV analysis was the best choice for collisional quenching, whereas, complex formation causing lifetime quenching was better explained by Tachiya's stochastic model. However, steady-state SV analysis was very crucial in our case, since it identifies the involvement of dark complex formations. The dark complex formation could neither be detected through a lifetime SV analysis nor in the fitting with a time-resolved stochastic model. It is worth mentioning here the definition of the dark complex is a bit tricky, as the dark complex may turn into an emissive complex when the lifetime is measured in the femtosecond upconversion setup instead of TCSPC. The dark complex is something that is not detected through time-resolved

measurements but the same is detected in a steady-state emission quenching study. One can simply assume this complex is not emitting a photon, hence lifetime can't be measured. However, if this complex emits photons with much shorter lifetimes compared to the temporal resolution of our instrument, we cannot detect it in time-resolved measurements and we will call the complex a dark complex but which is not. Therefore the CdTe QD-DNT dark complex here may not be non-emissive; rather an ultrafast PET might have quenched the lifetime of CdTe QD to a much faster timescale than the IRF of our TCSPC setup.

5.12 Conclusion

CdTe QD acts as an excellent electron donor in the presence of an electron-deficient molecule. Drastic quenching of CdTe QD emission (and excited-state lifetime) is a clear signature of PET taking place from the photo-excited QD* to DNT. THE bimolecular PET mechanism for a QD is completely different from that of an organic dye. In the latter case, the emission of organic dye is mostly quenched due to collision with the quencher molecules. However, for QD, the first quencher molecules are trapped at the surface capping layer of QD, followed by PET occurs. The mass transportation rate of the medium plays a significant role in collisional quenching, frequently observed in quenching studies of organic dye molecules. However, solvent diffusion plays an insignificant role for QD, where collision with quencher is not required for PET to take place. In the CdTe QD-DNT system, two types of complex formations (emissive and dark) are detected. Dark complex doesn't contribute to the lifetime quenching. Therefore, by using a stochastic kinetic model on lifetime quenching data, we focused only on the PET kinetic of emissive complexes. On the other hand, using steady-state Stern-Volmer (SV) analysis, we spectroscopically confirmed the involvement of dark complex formations. Therefore a combination of SV analysis and a stochastic

kinetic model is a nice approach to obtain a comprehensive understanding of PET kinetics of the QD-DNT system. Efficient quenching of CdTe QD fluorescence in the presence of DNT molecules indicating that apart from the photovoltaic applications of CdTe QDs, in the future CdTe QDs may be used for the detection of explosive nitroaromatic compounds.

Highlights of the thesis

The present thesis work is divided into a total of six chapters. The first two chapters are introduction and instrumentation chapters respectively. The rest four chapters are work chapters. The introduction chapter has been outlined to provide the basic knowledge of concepts, relevant to the thesis work, and their state of the art. The second chapter which is the instrumentation chapter is designed to provide an overview of the instrumentation used to carry out the thesis work and their working principles.

The rest four chapters are comprised of the strategic workflow. In these four chapters, we have studied two of the various excited state processes namely, Förster resonance energy transfer and photoinduced electron transfer involving nanoscale semiconductor systems known as "Quantum dots".

In the third chapter, we have studied FRET in a core-shell QD and an organic dye molecule "R6G" FRET pair. This FRET study was carried out by proposing a new approach using the already existing TRANES method. Our proposed method is model-free and a useful tool to capture, visualize, and quantify a FRET process. The method can be implemented in any FRET system. QD-R6G system was taken just as a model system in this case.

Apart from quantifying the FRET timescale, TRANES were also used to investigate the effect of donor-acceptor lifetimes on the FRET analysis. A set new of TRANES was simulated for this purpose and the details of the same are provided in the fourth chapter.

In the last two chapters, a detailed discussion of PET between synthesized CdTe Quantum dots and two small quencher molecules: Dinitrotoluene and N-methylaniline, is provided. ITC technique was utilized to explore the interaction between these small quencher molecules and the QDs. With the help of ITC and other fluorescence studies, two types of complex formation were observed: emissive and non-emissive complexes. A stochastic kinetic model along with the classical Stern-Volmer analysis was used to provide a complete picture of the PET process.

References:

(1) K. J. Vahala, *Nature* **2003**, *424*, 839–846.

(2) W. P. Ambrose, P. M. Goodwin, J. H. Jett, A. Van Orden, J. H. Werner, R. A. Keller, *Chem. Rev.* **1999**, *99*, 2929–2956.

(3) T. Bintsis, E. Litopoulou-Tzanetaki, R. K. Robinson, *J. Sci. Food Agric.* **2000**, *80*, 637–645.

(4) K. Mopper, C. A. Schultz, *Mar. Chem.* **1993**, *41*, 229–238.

(5) R. Richards-Kortum, E. Sevick-Muraca, *Annu. Rev. Phys. Chem.* **1996**, *47*, 555–606.

(6) V. Chandrasekhar, S. Das, R. Yadav, S. Hossain, R. Parihar, G. Subramaniam, P. Sen, *Inorg. Chem.* **2012**, *51*, 8664-8666.

(7) E. Petryayeva, W. R. Algar, I. L. Medintz, *Appl. Spectrosc.* **2013**, *67*, 215–252.

(8) A. Goetzberger, W. Greube, *Appl. Phys.* **1977**, *14*, 123–139.

(9) S. D.Verma, N. Pal, M. K. Singh, S. Sen, *J. Phys. Chem. B* **2015**, *119*, 11019-11029.

(10) M. S. H. Faizi, S. Gupta, V. K. Jain, P. Sen, *Sens. Actuators B Chem*. **2016**, *222*, 15-20.

(11) N. Pal, H. Shweta, M. K. Singh, S. D. Verma, S. Sen, *J. Phys. Chem. Lett*. **2015**, *6*, 1754-1760.

(12) (a) M. Chattoraj, B. A. King, G. U. Bublitz, S. G. Boxer, *Proc. Natl. Acad. Sci.* **1996**, *93*, 8362–8367. (b) C. Lawler, M. D. Fayer, *J. Phys. Chem. B* **2015**, *119*, 6024-6034.

(13) P. Dutta, P. Sen, A. Halder, S. Mukherjee, S. Sen, K. Bhattacharyya, *Chem. Phys. Lett.* **2003**, *377*, 229-235.

(14) O. K. Abou-Zied, N. Al-Lawatia, M. Elstner, T. B. Steinbrecher, *J. Phys. Chem. B* **2013**, *117*, 1062–1074.

(15) A. Mukhopadhyay, T. Hossen, I. Ghosh, A. L. Koner, W. M. Nau, K. Sahu, J. N. Moorthy, *Chem. Eur. J.* **2017**, *23*, 14797– 14805.

(16) C. T.Chen, Y. Wei, J. S. Lin, M. V. Moturu, W. S. Chao, Y. T. Tao, C. H. Chien, *J. Am. Chem. Soc.* **2006**, *128*, 10992–10993.

(17) (a) A. Phukon, K. Sahu, *Phys. Chem. Chem. Phys.* **2017**, *19*, 31461-31468. (b) D. B. Spry, M. D. Fayer, *J. Phys. Chem. B* **2009**, *113*, 10210-10221. (c) D. B. Spry, M. D. Fayer, *J. Chem. Phys.* **2007**, *127*, 204501.

(18) S. Koley, M. R. Panda, K. Bharadwaj, S. Ghosh, *Langmuir* **2018**, *34*, 817–825.

(19) K. Bhattacharyya, *Chem. Commun.* **2008**, *25*, 2848–2857.

(20) W. R. Algar, H. Kim, I. L. Medintz, N. Hildebrandt, *Coord. Chem. Rev.* **2014**, *263*, 65–85.

(21) J. R. Lakowicz, *Principles of Fluorescence Spectroscopy*; Springer science & business media, **2013**.

(22) P. T. Snee, R. C. Somers, G. Nair, J. P. Zimmer, M. G. Bawendi, D. G. Nocera, *J. Am. Chem. Soc.* **2006**, *128*, 13320–13321.

(23) M. H. Stewart, A. L. Huston, A. M. Scott, E. Oh, W. R. Algar, J. R. Deschamps, K. Susumu, V. Jain, D. E. Prasuhn, J. Blanco-Canosa, *Acs Nano* **2013**, *7*, 9489–9505.

(24) S. Weiss, *Nat. Struct. Biol.* **2000**, *7*, 724–729.

(25) D. M. Lilley, T. J. Wilson, *Curr. Opin. Chem. Biol.* **2000**, *4*, 507–517.

(26) M. Li, L. G. Reddy, R. Bennett, N. D. Silva Jr, L. R. Jones, D. D. Thomas, *Biophys. J.* **1999**, *76*, 2587–2599.

(27) H. Li, D. S. Lyles, M. J. Thomas, W. Pan, M. G. Sorci-Thomas, *J. Biol. Chem.* **2000**, *275*, 37048–37054.

(28) M. A. Tricerri, A. K. Behling Agree, S. A. Sanchez, J. Bronski, A. Jonas, *Biochemistry* **2001**, *40*, 5065–5074.

(29) Q. Xu, W. J. Brecht, K. H. Weisgraber, R. W. Mahley, Y. Huang, *J. Biol. Chem.* **2004**, *279*, 25511–25516.

(30) C. Berney, G. Danuser, *Biophys. J.* **2003**, *84*, 3992–4010.

(31) P. S. Chowdhury, P. Sen, A. Patra, *Chem. phys. lett.* **2005**, *413*, 311-314.

(32) M. Sato, T. Ozawa, K. Inukai, T. Asano, Y. Umezawa, *Nat. Biotechnol.* **2002**, *20*, 287–294.

(33) X. Huang, J. Wang, H. Liu, T. Lan, J. Ren, *Talanta* **2013**, *106*, 79–84.

(34) H. Kim, C. Y. Ng, W. R. Algar, *Langmuir* **2014**, *30*, 5676–5685.

(35) K. M. Parkhurst, L. J. Parkhurst, *J. Biomed. Opt.* **1996**, *1*, 435–442.

(36) L. E. Morrison, L. M. Stols, *Biochemistry* **1993**, *32*, 3095–3104.

(37) A. K. Mandal, S. Ghosh, A. K. Das, T. Mondal, K. Bhattacharyya, *ChemPhysChem* **2013**, *14*, 788-796.

(38) K. Sahu, S. Ghosh, S. K. Mondal, B. C. Ghosh, P. Sen, D. Roy, K. Bhattacharyya, *J. Chem. Phys.* **2006**, *125*, 044714(1-8).

(39) S. Sadhu, M. Tachiya, A. Patra, *J. Phys. Chem. C* **2009**, *113*, 19488–19492.

(40) I. L. Medintz, D. Farrell, K. Susumu, S. A. Trammell, J. R. Deschamps, F. M. Brunel, P. E. Dawson, H. Mattoussi, *Anal. Chem.* **2009**, *81*, 4831–4839.

(41) (a) P. A. Liddell, G. Kodis, A. L. Moore, T. A. Moore, D. Gust, *J. Am. Chem. Soc.* **2002**, *124* , 7668–7669. (b) V. S. Gladkikh, A. I. Burshtein, H. L. Tavernier, M. D. Fayer, *J. Phys. Chem. A* **2002**, *106*, 6982-6990.

(42) V. Bandi, H. B. Gobeze, F. D'Souza, C*hem. Eur. J.* **2015**, *21*, 11483–11494.

(43) D. Wróbel, A. Graja, *Coord. Chem. Rev.* **2011**, *255*, 2555–2577.

(44) S. Sasaki, G. P. Drummen, G. Konishi, *J. Mater. Chem. C* **2016**, *4*, 2731–2743.

(45) H. Imahori, Y. Sakata, *Adv. Mater.* **1997**, *9*, 537–546.

(46) D. Rehm, A. Weller, *Isr. J. Chem.* **1970**, *8*, 259–271.

(47) M. R. Eftink, C. A. Ghiron, *Biochemistry* **1984**, *23*, 3891–3899.

(48) H. S. Geethanjali, D. Nagaraja, R. M. Melavanki, R. A. Kusanur, *J. Lumin.* **2015**, *167*, 216–221.

(49) B. G. Evale, S. M. Hanagodimath, *J. Lumin.* **2010**, *130*, 1330–1337.

(50) S. Nad, H. Pal, *J. Phys. Chem. A* **2000**, *104*, 673–680.

(51) Y.-J. Zhao, K. Miao, Z. Zhu, L.-J. Fan, *ACS Sens.* **2017**, *2* , 842–847.

(52) T. P. Le, J. E. Rogers, L. A. Kelly, *J. Phys. Chem. A* **2000**, *104*, 6778–6785.

(53) R. Vos, Y. Engelborghs*, *Photochem. Photobiol.* **1994**, *60*, 24–32.

(54) M. Torimura, S. Kurata, K. Yamada, T. Yokomaku, Y. Kamagata, T. Kanagawa, R. Kurane, *Anal. Sci.* **2001**, *17*, 155–160.

(55) M. Sauer, K. H. Drexhage, U. Lieberwirth, R. Müller, S. Nord, C. Zander, *Chem. Phys. Lett.* **1998**, *284*, 153–163.

(56) F. D. Lewis, T. Wu, Y. Zhang, R. L. Letsinger, S. R. Greenfield, M. R. Wasielewski, *Science* **1997**, *277*, 673–676.

(57) S. Raichlin, E. Sharon, R. Freeman, Y. Tzfati, I. Willner, *Biosens. Bioelectron.* **2011**, *26*), 4681–4689.

(58) R. Freeman, I. Willner, *Nano Lett.* **2009**, *9*, 322–326.

(59) R. Freeman, T. Finder, L. Bahshi, R. Gill, I. Willner, *Adv. Mater.* **2012**, *24*, 6416–6421.

(60) R. Freeman, T. Finder, R. Gill, I. Willner, *Nano Lett.* **2010**, *10*, 2192–2196.

(61) R. Freeman, T. Finder, I. Willner, *Angew. Chem.* **2009**, *121*, 7958–7961.

(62) L. Zang, R. Liu, M. W. Holman, K. T. Nguyen, D. M. Adams, *J. Am. Chem. Soc.* **2002**, *124*, 10640–10641.

(63) R. Liu, M. W. Holman, L. Zang, D. M. Adams, *J. Phys. Chem. A* **2003**, *107*, 6522–6526.

(64) R. P. Detoma, L. Brand, *Chem. Phys. Lett.* **1977**, *47*, 231–236.

(65) D. Chakrabarty, P. Hazra, A. Chakraborty, D. Seth, N. Sarkar, *Chem. Phys. Lett.* **2003**, *381*, 697–704.

(66) K. Mishra, S. Koley, S. Ghosh, *J. Phys. Chem. Lett.* **2019**, *10*, 335–345.

(67) N. Dhenadhayalan, K. -C. Lin, R. Suresh, P. Ramamurthy, *J. Phys. Chem. C* **2016**, *120*, 1252–1261.

(68) A. S. R. Koti, N. Periasamy, *J. Chem. Phys.* **2001**, *115*, 7094–7099.

(69) A. S. R. Koti, N. Periasamy, *Res. Chem. Intermed.* **2002**, *28*, 831–836.

(70) V. R. Kishore, S. Kokane, K. L. Narasimhan, N. Periasamy, *Chem. Phys. Lett.* **2004**, *386*, 118–122.

(71) N. Nandi, K. Sahu, *J. Photochem. Photobiol. A* **2019**, *374*, 138-144.

(72) N. Periasamy, A. S. R. Koti, *Proc.-INDIAN Natl. Sci. Acad. PART A* **2003**, *69*, 41–48.

(73) A. S. R. Koti, N. Periasamy, *J. Chem. Sci.* **2001**, *113*, 157–163.

(74) A. S. R. Koti, M. M. G. Krishna, N. Periasamy, *J. Phys. Chem. A* **2001**, *105*, 1767–1771.

(75) S. Rakshit, R. Saha, P. K. Verma, S. K. Pal, *Photochem. Photobiol.* **2012**, *88*, 851–859.

(76) P. Verma, H. Pal, *J. Phys. Chem. A* **2012**, *116*, 4473–4484.

(77) S. Singh, S. Koley, K. Mishra, S. Ghosh, *J. Phys. Chem. C* **2018**, *122*, 732–740.

(78) A. Boulesbaa, A. Issac, D. Stockwell, Z. Huang, J. Huang, J. Guo, T. Lian, *J. Am. Chem. Soc.* **2007**, *129*, 15132–15133.

(79) A. C. Arango, L. R. Johnson, V. N. Bliznyuk, Z. Schlesinger, S. A. Carter,* H. H. Hörhold, *Adv Mater* **2001**, *12*, 1689–1692.

(80) D. F. Watson, G. J. Meyer, *Annu. Rev. Phys. Chem.* **2005**, *56*, 119–156.

(81) N. A. Anderson, T. Lian, *Annu. Rev. Phys. Chem.* **2005**, *56*, 491–519.

(82) H. Tributsch, *Coord. Chem. Rev.* **2004**, *248*, 1511–1530.

(83) V. Biju, M. Micic, D. Hu, H. P. Lu, *J. Am. Chem. Soc.* **2004**, *126*, 9374–9381.

(84) E. M. Sanehira, A. R. Marshall, J. A. Christians, S. P. P. N. Harvey, Ciesielski, L. M. Wheeler, P. Schulz, L. Y. Lin, M. C. Beard, J. M. Luther, *Sci. Adv.* **2017**, *3*, eaao4204.

(85) A. Swarnkar, A. R. Marshall, E. M. Sanehira, B. D. Chernomordik, D. T. Moore, J. A. Christians, T. Chakrabarti, J. M. Luther, *Science* **2016**, *354*, 92–95.

(86) M. Liu, O. Voznyy, R. Sabatini, F. P. G. de Arquer, R. Munir, A. H. Balawi, X. Lan, F. Fan, G. Walters, A. R. Kirmani, *Nat. Mater.* **2017**, *16*, 258–263.

(87) R. D. Schaller, V. I. Klimov, *Phys. Rev. Lett.* **2004**, *92*, 186601.

(88) A. J. Nozik, *Annu. Rev. Phys. Chem.* **2001**, *52*, 193–231.

(89) L. E. Brus, Chemistry and Physics of Semiconductor Nanocrystals. *Columbia Univ.* **2007**.

(90) M. T.Prabhu, N. Sarkar, *Protein Pept. Lett.* **2019**, *26*, 555-563.

(91) M. G. Bawendi, M. L. Steigerwald, L. E. Brus, *Annu. Rev. Phys. Chem.* **1990**, *41*, 477–496.

(92) R. Loef, A. J. Houtepen, E. Talgorn, J. Schoonman, A. Goossens, *Nano Lett.* **2009**, *9*, 856–859.

(93) I. L. Medintz, J. H. Konnert, A. R. Clapp, I. Stanish, M. E. Twigg, H. Mattoussi, J. M. Mauro, J. R. Deschamps, *Proc. Natl. Acad. Sci.* **2004**, *101*, 9612–9617.

(94) J. Ali, G. U. Siddiqui, K. H. Choi, Y. Jang, K. Lee, *J. Lumin.* **2016**, *169*, 342–347.

(95) L. Wang, X. Chen, Y. Lu, C. Liu, W. Yang, *Carbon* **2015**, *94*, 472–478.

(96) M. Mehta, D. Reuter, A. Melnikov, A. D. Wieck, A. Remhof, *Appl. Phys. Lett.* **2007**, *91*, 123108.

(97) X. Luo, B. Guo, L. Wang, F. Deng, R. Qi, S. Luo, C. Au, *Colloids Surf. Physicochem. Eng. Asp.* **2014**, *462*, 186–193.

(98) S. J. Lee, Z. Ku, A. Barve, J. Montoya, W. Y. Jang, S. R. J. Brueck, M. Sundaram, A. Reisinger, S. Krishna, S. K. Noh, *Nat. Commun.* **2011**, *2*, 1–6.

(99) F. E. Kruis, H. Fissan, A. Peled, *J. Aerosol Sci.* **1998**, *29*, 511–535.

(100) L. Mangolini, D. Jurbergs, E. Rogojina, U. Kortshagen, *J. Lumin.* **2006**, *121*, 327–334.

(101) Y. Zhang, A. Clapp, *Sensors* **2011**, *11*, 11036–11055.

(102) B. P. Biswal, D. B. Shinde, V. K. Pillai, R. Banerjee, *Nanoscale* **2013**, *5*, 10556–10561.

(103) E. Henry, A. Dif, M. Schmutz, L. Legoff, F. Amblard, V. Marchi-Artzner, F. Artzner, *Nano Lett.* **2011**, *11*, 5443–5448.

(104) W. Kwon, S. -W.Rhee, *Chem. Commun.* **2012**, *48*, 5256–5258.

(105) O. E. Rayevska, G. Y. Grodzyuk, V. M. Dzhagan, O. L. Stroyuk, S. Y. Kuchmiy, V. F. Plyusnin, V. P. Grivin, M. Y. Valakh, *J. Phys. Chem. C* **2010**, *114*, 22478–22486.

(106) H. S. Mansur, A. A. Mansur, *Mater. Chem. Phys.* **2011**, *125*, 709–717.

(107) W. Jiang, A. Singhal, J. Zheng, C. Wang, W. C. Chan, *Chem. Mater.* **2006**, *18*, 4845–4854.

(108) Y. Zheng, Z. Yang, J. Y. Ying, *Adv. Mater.* **2007**, *19*, 1475–1479.

(109) R. E. Bailey, S. Nie, *J. Am. Chem. Soc.* **2003**, *125*, 7100–7106.

(110) M. F. Kuehnel, D. W. Wakerley, K. L. Orchard, E. Reisner, *Angew. Chem. Int. Ed.* **2015**, *54*, 9627–9631.

(111) C. Gimbert-Suriñach, J. Albero, T. Stoll, J. Fortage, M. N. Collomb, A. Deronzier, E. Palomares, A. Llobet, *J. Am. Chem. Soc.* **2014**, *136*, 7655–7661.

(112) S. H. Lee, J. Ryu, D. H. Nam, C. B. Park, *Chem. Commun.* **2011**, *47*, 4643–4645.

(113) A. Shamirian, A. Ghai, P. T. Snee, *Sensors* **2015**, *15*, 13028–13051.

(114) S. Silvi, A. Credi, *Chem. Soc. Rev.* **2015**, *44*, 4275–4289.

(115) K. F. Chou, A. M. Dennis, *Sensors* **2015**, *15*, 13288–13325.

(116) D. Geiβler, N. Hildebrandt, *Curr. Inorg. Chem.* **2011**, *1*, 17–35.

(117) D. Geissler, S. Linden, K. Liermann, K. D. Wegner, L. J. Charbonniere, N. Hildebrandt, *Inorg. Chem.* **2014**, *53*, 1824–1838.

(118) N. Hildebrandt, K. D. Wegner, W. R. Algar, *Coord. Chem. Rev.* **2014**, *273*, 125–138.

(119) B. Hötzer, I. L. Medintz, N. Hildebrandt, *Small* **2012**, *8*, 2297–2326.

(120) E. Kymakis, G. A. J. Amaratunga, *Appl. Phys. Lett.* **2002**, *80*, 112–114.

(121) J. L. Segura, N. Martín, D. M. Guldi, *Chem. Soc. Rev.* **2005**, *34*, 31–47.

(122) M. C. Scharber, D. Mühlbacher, M. Koppe, P. Denk, C. Waldauf, A. J. Heeger, C. J. Brabec, *Adv. Mater.* **2006**, *18*, 789–794.

(123) P. Ravirajan, S. A. Haque, D. Poplavskyy, J. R. Durrant, D. D. C. Bradley, J. Nelson, *Thin Solid Films* **2004**, *451*, 624–629.

(124) W. Geens, T. Martens, J. Poortmans, T. Aernouts, J. Manca, L. Lutsen, P. Heremans, S. Borghs, R. Mertens, D. Vanderzande, *Thin Solid Films* **2004**, *451*, 498–502.

(125) E. Kucur, J. Riegler, G. A. Urban, T. Nann, *J. Chem. Phys.* **2004**, *120*, 1500–1505.

(126) M. Lonergan, *Annu Rev Phys Chem* **2004**, *55*, 257–298.

(127) N. A. Anderson, E. Hao, X. Ai, G. Hastings, T. Lian, *Chem. Phys. Lett.* **2001**, *347*, 304–310.

(128) K. Tvrdy, P. A. Frantsuzov, P. V. Kamat, *Proc. Natl. Acad. Sci.* **2011**, *108*, 29–34.

(129) P. V. Kamat, *Acc. Chem. Res.* **2012**, *45*, 1906–1915.

(130) G. S. Bassi, A. I. Murchie, F. Walter, R. M. Clegg, D. M. Lilley, *EMBO J.* **1997**, *16*, 7481–7489.

(131) S. Koley, S. Ghosh, *Phys. Chem. Chem. Phys.* **2016**, *18*, 32308–32318.

(132) A. Bhowmik, H. Kaur, S. Koley, S. Jana, S. Ghosh, *J. Phys. Chem. C* **2016**, *120*, 5308–5314.

(133) S. Paula, W. Sues, J. Tuchtenhagen, A. Blume, *J. Phys. Chem.* **1995**, *99*, 11742–11751.

(134) S. Dai, K. C. Tam, *J. Phys. Chem. B* **2001**, *105*, 10759–10763.

(135) S. Dai, K. C. Tam, *Langmuir* **2005**, *21*, 7136–7142.

(136) W. Loh, C. Brinatti, K. C. Tam, *Biochim. Biophys. Acta BBA-Gen. Subj.* **2016**, *1860*, 999–1016.

(137) A. Biela, N. N. Nasief, M. Betz, A. Heine, D. Hangauer, G. Klebe, *Angew. Chem. Int. Ed.* **2013**, *52*, 1822–1828.

(138) S. Winzen, S. Schoettler, G. Baier, C. Rosenauer, V. Mailaender, K. Landfester, K. Mohr, *Nanoscale* **2015**, *7*, 2992–3001.

(139) W. Becker, *Advanced Time-Correlated Single Photon Counting Techniques*; Springer Science & Business Media, **2005**; Vol. 81.

(140) M. Maroncelli, G. R. Fleming, *J. Chem. Phys.* **1987**, *86*, 6221–6239.

(141) T. Wiseman, S. Williston, J. F. Brandts, L. N. Lin, *Anal. Biochem.* **1989**, *179*, 131–137.

(142) E. Freire, O. L. Mayorga, M. Straume, *Anal. Chem.* **1990**, *62*, 950A–959A.

(143) B. J. Berne, R. Pecora, *Dynamic Light Scattering: With Applications to Chemistry, Biology, and Physics*; Courier Corporation, **2000**.

(144) C. Gell, D. Brockwell, A. Smith, *Handbook of Single Molecule Fluorescence Spectroscopy*; Oxford University Press on Demand, **2006**.

(145) N. Pal, S. D. Verma, M. K. Singh, S. Sen, *Anal. chem.* **2011**, *83*, 7736-7744.

(146) L. E. Brus, *J. Chem. Phys.* **1984**, *80*, 4403–4409.

(147) N. Hildebrandt, C. M. Spillmann, W. R. Algar, T. Pons, M. H. Stewart, E. Oh, K. Susumu, S. A. Diaz, J. B. Delehanty, I. L. Medintz, *Chem. Rev.* **2017**, *117*, 536–711.

(148) S. Kundu, A. Patra, *Chem. Rev.* **2017**, *117*, 712–757.

(149) I. L. Medintz, M. H. Stewart, S. A. Trammell, K. Susumu, J. B. Delehanty, B. C. Mei, J. S. Melinger, J. B. Blanco-Canosa, P. E. Dawson, H. Mattoussi, *Nat. Mater.* **2010**, *9*, 676–684.

(150) W. R. Algar, K. Susumu, J. B. Delehanty, I. L. Medintz, *Semiconductor Quantum Dots in Bioanalysis: Crossing the Valley of Death*; ACS Publications, **2011**.

(151) A. R. Clapp, T. Pons, I. L. Medintz, J. B. Delehanty, J. S. Melinger, T. Tiefenbrunn, P. E. Dawson, B. R. Fisher, B. O'Rourke, H. Mattoussi, *Adv. Mater.* **2007**, *19*, 1921–1926.

(152) I. L. Medintz, N. Hildebrandt, *FRET-Förster Resonance Energy Transfer: From Theory to Applications*; John Wiley & Sons, **2013**.

(153) P. Moroz, W. P. Klein, K. Akers, A. Vore, N. Kholmicheva, N. Razgoniaeva, D. Khon, S. A. Díaz, I. L. Medintz, M. Zamkov, *J. Phys. Chem. C* **2017**, *121*, 26226–26232.

(154) P. Moroz, N. Razgoniaeva, Y. He, G. Jensen, H. Eckard, H. P. Lu, M. Zamkov, *ACS Nano* **2017**, *11*, 4191–4197.

(155) N. Kholmicheva, P. Moroz, E. Bastola, N. Razgoniaeva, J. Bocanegra, M. Shaughnessy, Z. Porach, D. Khon, M. Zamkov, *ACS Nano* **2015**, *9*, 2926–2937.

(156) S. Sadhu, A. Patra, *J. Phys. Chem. C* **2011**, *115*, 16867–16872.

(157) S. Sadhu, A. Patra, *J. Phys. Chem. C* **2012**, *116*, 15167–15173.

(158) S. Sadhu, K. K. Haldar, A. Patra, *J. Phys. Chem. C* **2010**, *114*, 3891–3897.

(159) M. Hilczer, M. Tachiya, *J. Phys. Chem. C* **2009**, *113*, 18451–18454.

(160) A. Al Salman, A. Tortschanoff, G. Van der Zwan, F. Van Mourik, M. Chergui, *Chem. Phys.* **2009**, *357*, 96–101.

(161) L. Hartmann, A. Kumar, M. Welker, A. Fiore, C. Julien-Rabant, M. Gromova, M. Bardet, P. Reiss, P. N. Baxter, F. *ACS Nano* **2012**, *6*, 9033–9041.

(162) J. F. Callan, R. C. Mulrooney, S. Kamila, B. McCaughan, *J. Fluoresc.* **2008**, *18*, 527–532.

(163) W. R. Algar, M. H. Stewart, A. M. Scott, W. J. Moon, I. L. Medintz, *J. Mater. Chem. B* **2014**, *2*, 7816–7827.

(164) K. Truong, M. Ikura, *Curr. Opin. Struct. Biol.* **2001**, *11*, 573–578.

(165) I. L. Medintz, A. R. Clapp, H. Mattoussi, E. R. Goldman, B. Fisher, J. M. Mauro, *Nat. Mater.* **2003**, *2*, 630–638.

(166) Q. Ni, J. Zhang, Dynamic Visualization of Cellular Signaling. In *Nano/Micro Biotechnology*; Springer, **2009**, 79–97.

(167) J. R. Silvius, I. R. Nabi, *Mol. Membr. Biol.* **2006**, *23*, 5–16.

(168) S. Ghosh, N. K. Das, U. Anand, S. Mukherjee, *J. Phys. Chem. Lett.* **2015**, *6*, 1293–1298.

(169) Y. P. Kim, Y.-H. Oh, E. Oh, H. -S. Kim, *Biochip J* **2007**, *1*, 228–233.

(170) A. M. Dennis, W. J. Rhee, D. Sotto, S. N. Dublin, G. Bao, *ACS Nano* **2012**, *6*, 2917–2924.

(171) K. Zhang, Q. Mei, G. Guan, B. Liu, S. Wang, Z. Zhang, *Anal. Chem.* **2010**, *82*, 9579–9586.

(172) M. D. Kattke, E. J. Gao, K. E. Sapsford, L. D. Stephenson, A. Kumar, *Sensors* **2011**, *11*, 6396–6410.

(173) P. Wu, T. Zhao, S. Wang, X. Hou, *Nanoscale* **2014**, *6*, 43–64.

(174) K. Bharadwaj, S. Koley, S. Jana, S. Ghosh, *Chem. Asian J.* **2018**, *13*, 3296 – 3303.

(175)(a) S. M. Park, A. J. Bard, *J. Electroanal. Chem. Interfacial Electrochem.* **1977**, *77*, 137-152. (b) J. Huang, D. Stockwell, Z. Huang, D. L. Mohler, T. Lian, *J. Am. Chem. Soc.* **2008**, *130*, 5632-5633.

(176) R. S. Fee, M. Maroncelli, *Chem. Phys.* **1994**, *183*, 235–247.

(177) A. Phukon, S. Ray, K. Sahu, *Langmuir* **2016**, *32*, 10659–10667.

(178) A. S. R. Koti, M. M. G. Krishna, N. Periasamy, *J. Phys. Chem. A* **2001**, *105*, 1767–1771.

(179) E. Haustein, P. Schwille, Fluorescence Correlation Spectroscopy: An Introduction to Its Concepts and Applications. *Biophys. Textb. Online* **2004**.

(180) S. Ghosh, U. Mandal, A. Adhikari, K. Bhattacharyya, *Chem. Asian J.* **2009**, *4*, 948–954.

(181) Y. Y. Kievsky, B. Carey, S. Naik, N. Mangan, Ben- D. Avraham, I. Sokolov, *Dynamics of Molecular Diffusion of Rhodamine 6G in Silica Nanochannels*; American Institute of Physics, **2008**.

(182) S. Koley, M. R. Panda, S. Ghosh, *J. Phys. Chem. C* **2016**, *120*, 13456–13465.

(183) S. F. Wuister, I. Swart, F. van Driel, S. G. Hickey, C. de Mello Donegá, *Nano Lett.* **2003**, *3*, 503–507.

(184) B. Jana, A. Ghosh, S. Maiti, D. Bain, S. Banerjee, H. N. Ghosh, A. Patra, *J. Phys. Chem. C* **2016**, *120*, 25142–25150.

(185) P. Maity, T. Debnath, H. N.Ghosh, *J. Phys. Chem. Lett.* **2013**, *4*, 4020–4025.

(186) D. L. Smith, T. C. McGill, J. N. Schulman, *Appl. Phys. Lett.* **1983**, *43*, 180–182.

(187) Z. Li, Y. Zhou, D. Yan, M. Wei, *J. Mater. Chem. C* **2017**, *5*, 3473–3479.

(188) B. Rezaei, M. Shahshahanipour, A. A. Ensafi, *Luminescence* **2016**, *31*, 958–964.

(189) K. W. Mitchell, A. L. Fahrenbruch, R. H. Bube, *J. Appl. Phys.* **1977**, *48*, 4365–4371.

(190) C. Ge, M. Xu, J. Liu, J. Lei, H. Ju, *Chem. Commun.* **2008**, *4*, 450–452.

(191) A. Castaldini, A. Cavallini, B. Fraboni, P. Fernandez, J. Piqueras, *J. Appl. Phys.* **1998**, *83*, 2121–2126.

(192) Z. He, W. Li, G. F. Knoll, D. K. Wehe, J. Berry, C. M. Stahle, *Nucl. Instrum. Methods Phys. Res. Sect. Accel. Spectrometers Detect. Assoc. Equip.* **1999**, *422*, 173–178.

(193) S. M. Johnson, J. L. Johnson, W. J. Hamilton, D. B. Leonard, T. A. Strand, E. A. Patten, J. M. Peterson, J. H. Durham, V. K. Randall, T. J. Delyon, *J. Electron. Mater.* **2000**, *29*, 680–686.

(194) P. Norton, *Optoelectron. Rev.* **2002**, *3*, 159–174.

(195) G. Fonthal, L. Tirado-Mejıa, J. I. Marın-Hurtado, H. Ariza-Calderon, J. G. Mendoza-Alvarez, *J. Phys. Chem. Solids* **2000**, *61*, 579–583.

(196) A. C. Vinayaka, S. Basheer, M. S. Thakur, *Biosens. Bioelectron.* **2009**, *24*, 1615–1620.

(197) S. M. Ng, M. Koneswaran, R. Narayanaswamy, *RSC Adv.* **2016**, *6*, 21624–21661.

(198) X. Ding, L. Qu, R. Yang, Y. Zhou, J. Li, *Luminescence* **2015**, *30*, 465–471.

(199) S. Sarkar, R. Pramanik, D. Seth, P. Setua, N. Sarkar, *Chem. Phys. Lett.* **2009**, *477*, 102–108.

(200) S. Ghosh, K. Sahu, S. K. Mondal, P. Sen, K. Bhattacharyya, *J. Chem. Phys.* **2006**, *125*, 054509.

(201) P. Mukherjee, S. Biswas, P. Sen, *J. Phys. Chem. B* **2015**, *119*, 11253–11261.

(202) M. Kumbhakar, T. Mukherjee, H. Pal, *Chem. Phys. Lett.* **2005**, *410*, 94–98.

(203) Y. Nagasawa, A. P. Yartsev, K. Tominaga, A. E. Johnson, K. Yoshihara, *J. Am. Chem. Soc.* **1993**, *115*, 7922–7923.

(204) M. Koch, A. Rosspeintner, G. Angulo, E. Vauthey, *J. Am. Chem. Soc.* **2012**, *134*, 3729–3736.

(205) A. Paul, A. Samanta, *J. Phys. Chem. B* **2007**, *111*, 1957–1962.

(206) R. C. Dorfman, M. D. Fayer, *J. Chem. Phys.* **1992**, *96*, 7410–7422.

(207) S. Murata, M. Nishimura, S. Y. Matsuzaki, M. Tachiya, *Chem. Phys. Lett.* **1994**, *219*, 200–206.

(208) D. D. Eads, B. G. Dismer, G. R. Fleming, *J. Chem. Phys.* **1990**, *93*, 1136–1148.

(209) K. Bharadwaj, H. Choudhary, S. Hazra, S. Ghosh, *Chem. Asian J.* **2019**, *14*, 4207-4216.

(210) D. V. Talapin, S. Haubold, A. L. Rogach, A. Kornowski, M. Haase, H. Weller, *J. Phys. Chem. B* **2001**, *105*, 2260–2263.

(211) L. Dworak, A. J. Reuss, M. Zastrow, K. Rück-Braun, J. Wachtveitl, *Nanoscale* **2014**, *6*, 14200–14203.

(212) K. Bharadwaj, S. Koley, S. Jana, S. Ghosh, *Chem. Asian J.* **2018**, *13*, 3296–3303.

(213) M. Tachiya, APPLICATION OF A GENERATING FUNCTION TO REACTION KINETICS IN MICELLES. KINETICS OF QUENCHING OF LUMINESCENT PROBES IN MICELLES. **1975**.

(214) M. Tachiya, *J. Chem. Phys.* **1982**, *76*, 340–348.

(215) H. Leng, J. Loy, V. Amin, E. A. Weiss, M. Pelton, *ACS Energy Lett.* **2016**, *1*, 9–15.

(216) M. C. Sekhar, A. Samanta, *J. Phys. Chem. C* **2015**, *119*, 15661–15668.

(217) K. E. Knowles, M. D. Peterson, M. R. McPhail, E. A. Weiss, *J. Phys. Chem. C* **2013**, *117*, 10229–10243.

(218) H. Tu, D. F. Kelley, *Nano Lett.* **2006**, *6*, 116–122.

(219) X. Wang, L. Cao, F. Lu, M. J. Meziani, H. Li, G. Qi, B. Zhou, B. A. Harruff, F. Kermarrec, Y. P. Sun, *Chem. Commun.* **2009**, *0*, 3774–3776.

(220) H. Zang, P. K. Routh, R. Alam, M. M. Maye, M. Cotlet, *Chem. Commun.* **2014**, *50*, 5958–5960.

(221) S. S. M. Rodrigues, D. S. Ribeiro, J. X. Soares, M. L. Passos, M. L. M. Saraiva, J. L. Santos, *Coord. Chem. Rev.* **2017**, *330*, 127–143.

(222) X. Mathew, G. W. Thompson, V. P. Singh, J. C. McClure, S. Velumani, N. R. Mathews, P. J. Sebastian, *Sol. Energy Mater. Sol. Cells* **2003**, *76*, 293–303.

(223) A. K. Shukla, K. Sudhakar, P. Baredar, *Energy Build.* **2016**, *128*, 99–110.

(224) B. Parida, S. Iniyan, R. Goic, *Renew. Sustain. Energy Rev.* **2011**, *15*, 1625–1636.

(225) L. Kranz, S. Buecheler, A. N. Tiwari, *Sol. Energy Mater. Sol. Cells* **2013**, *119*, 278–280.

(226) P. V. Meyers, R. T. Birkmire, *Prog. Photovolt. Res. Appl.* **1995**, *3*, 393–402.

(227) A. H. Munshi, J. M. Kephart, A. Abbas, T. M. Shimpi, K. L. Barth, J. M. Walls, W. S. Sampath, *Sol. Energy Mater. Sol. Cells* **2018**, *176*, 9–18.

(228) J. Tao, S. Yu, *Sol. Energy Mater. Sol. Cells* **2015**, *141*, 108–124.

(229) Z. Fan, H. Razavi, J. Do, A. Moriwaki, O. Ergen, Y. -L. Chueh, P. W. Leu, J. C. Ho, T. L. A. Takahashi, Reichertz, *Nat. Mater.* **2009**, *8*, 648–653.

(230) J. Peng, L. Lu, H. Yang, *Renew. Sustain. Energy Rev.* **2013**, *19*, 255–274.

(231) V. Fthenakis, H. C. Kim, *Renew. Sustain. Energy Rev.* **2010**, *14*, 2039–2048.

(232) M. M. de Wild-Scholten, *Sol. Energy Mater. Sol. Cells* **2013**, *119*, 296–305.

(233) S. Kaniyankandy, S. Rawalekar, H. N. Ghosh, *J. Phys. Chem. C* **2012**, *116*, 16271–16275.

(234) T. Baines, T. P. Shalvey, J. D. Major, CdTe Solar Cells. In *A Comprehensive Guide to Solar Energy Systems*; Elsevier, **2018**, 215–232.

(235) J. D. Major, R. E. Treharne, L. J. Phillips, K. Durose, *Nature* **2014**, *511*, 334–337.

(236) S. J. Rosenthal, J. C. Chang, O. Kovtun, J. R. McBride, I. D. Tomlinson, *Chem. Biol.* **2011**, *18*, 10–24.

(237) A. Schroedter, H. Weller, R. Eritja, W. E. Ford, J. M. Wessels, *Nano Lett.* **2002**, *2*, 1363–1367.

(238) C. T. Matea, T. Mocan, F. Tabaran, T. Pop, O. Mosteanu, C. Puia, C. Iancu, L. Mocan, *Int. J. Nanomedicine* **2017**, *12*, 5421.

(239) S. Wang, N. Mamedova, N. A. Kotov, W. Chen, J. Studer, *Nano Lett.* **2002**, *2*, 817–822.

(240) Y. Q. Sun, J. Liu, X. Lv, Y. Liu, Y. Zhao, W. Guo, *Angew. Chem. Int. Ed.* **2012**, *51*, 7634–7636.

(241) K. Kiyose, S. Aizawa, E. Sasaki, H. Kojima, K. Hanaoka, T. Terai, Y. Urano, T. Nagano, *Chem. Eur. J.* **2009**, *15*, 9191–9200.

(242) J. Ma, J.-Y. Chen, J. Guo, C. C. Wang, W. L. Yang, L. Xu, P. N. Wang, *Nanotechnology* **2006**, *17*, 2083.

(243) P. V. Kamat, *J. Phys. Chem. C* **2008**, *112*, 18737–18753.

(244) A. Rosspeintner, G. Angulo, E. Vauthey, *J. Am. Chem. Soc.* **2014**, *136*, 2026–2032.

(245) K. Bharadwaj, H. Choudhary, S. Hazra, S. Ghosh, *ChemPhysChem* **2020**, *21*, 415-422.

(246) S. Koley, S. Ghosh, *Phys. Chem. Chem. Phys.* **2016**, *18*, 24830-24834.